Order Number 9507299

Nitrogen oxides in the arctic stratosphere: Implications for ozone abundances

Slusser, James Robert, Ph.D.

University of Alaska Fairbanks 1994

U·M·I
300 N. Zeeb Rd.
Ann Arbor, MI 48106

NITROGEN OXIDES IN THE ARCTIC STRATOSPHERE: IMPLICATIONS FOR OZONE ABUNDANCES

A

THESIS

Presented to the Faculty
of the University of Alaska Fairbanks
in Partial Fulfillment of the Requirements
for the Degree of

DOCTOR OF PHILOSOPHY

By

James Robert Slusser, B. S., M. A.

Fairbanks, Alaska

May 1994

NITROGEN OXIDES IN THE ARCTIC STRATOSPHERE: IMPLICATIONS FOR OZONE ABUNDANCES

By
James Robert Slusser

RECOMMENDED:

Dr. Glenn Shaw

Dr. Richard Benner

Dr. Brenton Watkins

Dr. Victor Filyushkin

Dr. Roger Smith

Dr. Knut Stamnes, Chairman, Advisory Commitee

Dr. John Morack, Head, Physics Department

APPROVED:

Dr. Paul B. Reichardt, Dean, College of Natural Sciences

Dr. Joe Kan, Dean of the Graduate School

April 27, 1994
Date

Abstract

In the high latitude winter stratosphere, NO_2 sequesters chlorine compounds which are extremely efficient at destroying ozone. During the nighttime, NO_2 reacts with ozone to form N_2O_5 which acts as a reservoir of NO_2. Under heavy aerosol loading, N_2O_5 may react with water on aerosol surfaces to form HNO_3, a reservoir more resistant to photolysis. This heterogeneous reaction results in reduced NO_2 concentration when the sun returns at the end of the winter.

A spectrograph system has been developed to measure scattered zenith skylight and thereby determine stratospheric NO_2 slant column abundance. Conversion of the measured slant column abundance to vertical column abundance requires dividing by the air mass. The air mass is the enhancement in the optical path for the scattered twilight as compared to a vertical path. Air mass values determined using a multiple scattering radiative transfer code have been compared to those derived using a Monte Carlo code and were found to agree to within 6% at a 90° solar zenith angle for a stratospheric absorber.

Six months of NO_2 vertical column abundance measured over Fairbanks during the winter 1992-93 exhibited the

daylight diminished and increased as the sunlight hours lengthened. The overall seasonal behavior was similar to high-latitude measurements made in the Southern Hemisphere. The ratios of morning to evening column abundance were consistent with predictions based on gas-phase chemistry. The possible heterogeneous reaction of N_2O_5 on sulfate aerosols was investigated using Fourier Transform Infrared Spectrometer measurements of HNO_3 column abundance and lidar determinations of the aerosol profile. Using an estimated N_2O_5 column abundance and aerosol profile as input to a simple model, significant HNO_3 production was expected. No increase in HNO_3 column abundance was measured. From this set of data, it was not possible to determine whether significant amounts of N_2O_5 were converted to HNO_3 by this heterogeneous reaction. Better estimates of the N_2O_5 and aerosol profile, and a more continuous set of HNO_3 measurements, are needed to determine if HNO_3 was actually produced.

Table of Contents

List of Figures

List of Tables

Acknowledgements

It's been a long haul and it's hard to know where to begin. There are so many people to thank and who have touched my life. To my two advisors, Knut Stamnes and Glenn Shaw I owe deep gratitude for mentoring me in the old European tradition of Cavendish and Helmholtz. Each in his own way encouraged, cajoled and occasionally threatened me to give me the strength to forge ahead in my pursuit of knowledge about the stratosphere. Although each was heavily committed to raising families, writing proposals, training other graduate students, traveling, and fighting for space for our growing department, both spent long hours reading my writing, some it only half formed, or listening as I formulated new ideas, not always clearly. Richard Benner spent hours tutoring me in inorganic chemistry, encouraging me to write on his board in colored magic marker that dried just as I was getting to the point, shared his love of atmospheric chemistry and experimentation as well as letting us use his microwave. More than that, Rich was the one to say "you've got enough to write up, now go get a job." Roger Smith was the godfather of the electronics and overall software design and has the gift of making the difficult seem straightforward and amusing. Dan Jaffe helped me to see early on the importance of getting testable hypotheses

together and introduced me to atmospheric chemistry. Victor Filyushkin came like a welcome cold front after weeks of heat and humidity and to give me insight to the myriad chemical reactions in the stratosphere. To Brenton Watkins, thanks for cogent advice and reading yet another thesis.

To Baltimore Larry Kozicki and his peerless machinists, nothing is free but every job you did was flawless. Sharpening wits against yours was, well humor at each other's expense. To Benny and his electronics wizards, thanks for the advice on SAABs, wireups, and dance lessons.

To Paul Johnston and Richard McKenzie of New Zealand NIWA words are inadequate to express my debt. Not only did they provide their software which took many years to develop, they took hours out of their heavy schedule to respond in well thought out letters to my sometimes pleading emails on the nitty gritty of analysis. Without their help this work would not have been written. Their papers cleared a path for my project, but more than that their friendship sustained me in days and weeks where it seemed I was adrift in a sea of inconclusive results and crashing code. It is to them that I dedicate this dissertation.

To Susan Solomon and George Mount of the NOAA aeronomy lab, a big thank you for continual support and clear direction. Both generously provided the insight of their research and helped me focus instrumentation development and

scientific questions.

Thanks to Lori Perliski and Arne Dahlback for supplying computations and descriptions of their scattering models and to Kyle Hammond and Jianli Sun for expert programming.

To the National Science Foundation for funding, to the GI for all that was required, to the National Weather Service for maps and data (thanks Kraig), to University of Denver for FTIR and insight (thanks Xu, David and Frank), to Takeshi Shibata, and Y. Iwasaka of Nagoya University, and M. Fujiwara of Fukuoko University for lidar data, to the Computer Resource Center. Thanks to Gloria Koening of the Climate Monitoring Diagnostic Laboratory.

To Ginny my sister, we did it, and this is our year. Our growing friendship is a treasure that I cherish. To Jim and Walt Tape, you showed me what it takes to make it in science while at the same time be loving men. And to my father Bob, can you believe it? You encouraged my questions and probing. You taught me to patiently surround the unknown until it yielded its secrets to logic. To the memory of my mother Elizabeth, who taught me to revere life and to wonder at the grandeur of this world we walk upon so briefly. To Paul, my brother and pathfinder, I wish you could see the world you helped shape. I won't forget even one of you many acts of nobility.

And to Clara Mary for your pesky sense of humor and

witty comments regarding everything from food to electronegativity.

Chapter 1

Introduction

The goal of this research is to investigate the role of nitrogen oxides in stratospheric chemistry at high latitudes. Measurements obtained at Fairbanks, Alaska (65°N) are used for this purpose.

The importance of nitrogen oxides in the stratosphere relates to ozone abundance. Nitrogen dioxide, NO_2, influences ozone abundance in several important ways, and its measurement, especially in conjunction with measured stratospheric temperatures, wind, and other trace gas abundances can yield valuable information about the stratosphere [*Solomon*, 1990].

1.1: The Chapman Reactions

The *Chapman* [1930] reactions predict an ozone layer formed by sunlight acting upon a pure oxygen atmosphere

$$O_2 + h\nu \rightarrow O + O \quad (\lambda < 242\ nm) \tag{1.1}$$

$$O + O_2 + M \rightarrow O_3 + M \tag{1.2}$$

$$O_3 + h\nu \rightarrow O_2 + O \quad (\lambda < 800\ nm) \tag{1.3}$$

$$O + O_3 \rightarrow 2O_2\ . \tag{1.4}$$

Formation of ozone depends on the availability of atomic

oxygen, which is produced in the stratosphere by photolysis of molecular oxygen. At altitudes greater than 80 km, where atomic oxygen is abundant, recombination of oxygen atoms with molecular oxygen competes with the production of ozone

$$O + O + M \rightarrow O_2 + M \,. \qquad (1.5)$$

In these reactions, M represents a molecule (typically N_2 or O_2) that is needed to conserve mechanical energy and momentum in the collisional interaction. The wavelengths (λ) in parentheses after reactions (1.1) and (1.3) indicate the long wavelength limit of photodissociation. Note that reaction (1.3) destroys O_3 only temporarily since the atomic oxygen produced rapidly attaches to O_2 to reform ozone in reaction (1.2). Thus, the sum of odd oxygen, defined $O_x = O + O_3$, is unchanged by this reaction.

The Chapman reactions alone would predict an ozone layer reaching its maximum number concentration in the stratosphere below the altitude of maximum production of atomic oxygen. The ozone concentration would not peak at the altitude of maximum atomic oxygen production because ozone formation in reaction (1.2) is a three body reaction that proceeds with greater probability at lower altitudes. The rate of atomic oxygen production from reaction (1.1) reaches a maximum because it is the product of two functions: the intensity of ultraviolet solar radiation

which increases with height, and the density of O_2 which decreases with height. Using these oxygen reactions alone with the appropriate photodissociation rates yields twice the observed ozone concentration in the middle and upper stratosphere between 20 and 50 km and about 10 times the observed concentration in the mesosphere between 50 and 100 km. The only reaction that destroys ozone, reaction (1.4), is too slow to account for the observed ozone profile meaning additional ozone loss terms must be considered.

1.2: Role of Free Radicals

Additional ozone losses were hypothesized by *Crutzen* [1970] to occur because of catalytic reactions between odd oxygen and molecules with unpaired electrons ("free radicals") in the nitrogen, hydrogen, chlorine, and bromine oxide groups [*Nicolet*, 1975; and *Shimazaki*, 1985]. Molecules react chemically only when the repulsive barrier between them is overcome. The energy required to overcome this barrier is known as the activation energy which can be either kinetic or electronic. The free radicals are reactive because of their low activation energies, typically from 5 to 40 kJ/mole (0.05 to 0.41 eV) [*Warneck*, 1988]. Catalytic reactions which destroy ozone can be shown as

$$X + O_3 \rightarrow XO + O_2 \qquad (1.6)$$

$$XO + O \rightarrow X + O_2 \qquad (1.7)$$

$$Net \quad O_3 + O \rightarrow 2O_2 \qquad (1.8)$$

where X could represent NO, H, HO, Cl, or Br. Since there are over 100 stratospheric reactions involving ozone and other important trace gases, it is useful to group molecules into families in which the sum of individual members are conserved to a first approximation. For instance, NO_y is defined as ($NO + NO_2 + NO_3 + 2N_2O_5 + ClONO_2 + HNO_3$).

1.3: The Role of Nitrogen Oxides in the Stratosphere

Although molecular nitrogen (N_2) is the most abundant terrestrial gas, it is nearly unreactive in the troposphere and stratosphere because of its bond strength of 941.7 kJ/mole (9.76 eV, corresponding to a photon of λ = 127 nm) and is not a source of stratospheric NO or NO_2. The sum of ($NO + NO_2$) is defined to be NO_x. The main source of stratospheric NO_x is the addition of oxygen (oxidation) to terrestrial N_2O formed by biological and industrial reactions of molecular nitrogen [*Brasseur and Solomon*, 1986]. N_2O is oxidized in the stratosphere by the excited

singlet state of atomic oxygen $O(^1D)$ produced by photodissociation of O_3. The excitation energy of $O(^1D)$ is 190 kJ/mole (1.96 eV) making it reactive with a vast array of molecules

$$O_3 + h\nu \rightarrow O(^1D) \quad (\lambda < 320\ nm) \tag{1.9}$$

$$N_2O + O(^1D) \rightarrow 2NO\ . \tag{1.10}$$

Another possible reaction is

$$N_2O + O(^1D) \rightarrow N_2 + O_2\ . \tag{1.11}$$

Since the production of $O(^1D)$ in reaction (1.9) requires energetic photons of wavelength shorter than 320 nm for its formation, and since ozone blocks most of this radiation at altitudes below 15 km, N_2O is stable in the troposphere, and NO production by reaction (1.10) reaches its maximum between 20 and 35 km. The actual height of this maximum depends upon the distribution of $O(^1D)$ which is a function of solar zenith angle. The height of the maximum depends upon the values of the vertical eddy diffusion coefficient, K_{zz}, [*Brasseur and Solomon*, 1986] because this dictates how quickly tropospheric N_2O diffuses up to the stratosphere.

The resulting nitrogen oxide molecule, NO, produced from reaction (1.10) rapidly reacts with ozone to form nitrogen dioxide

$$NO + O_3 \rightarrow NO_2 + O_2 \ . \qquad (1.12)$$

In sunlight, NO and NO_2 quickly establish a photostationary state at altitudes less than 45 km [*Wayne*, 1991]

$$NO_2 + h\nu \rightarrow NO + O \quad (\lambda < 400\ nm) \qquad (1.13)$$

$$NO + O_3 \rightarrow NO_2 + O_2 \ . \qquad (1.14)$$

NO_2 is effective at the catalytic destruction of O_3 because atomic oxygen reacts with NO_2 at a much higher reaction rate than it does with O_3 in reaction (1.4) which more than makes up for its much smaller mixing ratio (about 100 times smaller than O_3). Thus the following reaction is more likely than reaction (1.4) [*Warneck*, 1988]

$$NO_2 + O \rightarrow NO + O_2 \ . \qquad (1.15)$$

NO_x influences ozone abundance in three ways. First, the NO_x catalytic cycle is the most important of the ozone destroying trace gas cycles between 15 and 40 km [*Shimazaki*, 1985] where the following reactions take place

$$NO + O_3 \rightarrow NO_2 + O_2 \qquad (1.16)$$

$$NO_2 + O \rightarrow NO + O_2 \qquad (1.17)$$

$$Net \quad O_3 + O \rightarrow 2O_2 \ . \qquad (1.18)$$

Second, only with low levels of NO_x in the polar

stratosphere can levels of ClO increase so that severe depletions of ozone occur through the various chlorine catalytic cycles. The three reactions below occur on the surfaces of polar stratospheric clouds (PSCs) [*Solomon*, 1990] which are a mixture of water, nitric acid, sulfuric acid, and hydrochloric acid [*Wofsy, et al.*, 1988; *Hamill and Toon*; 1991]. The result of these reactions is to reduce forms of nitrogen like NO and NO_2 that react with ozone, and to release chlorine compounds that once photolyzed are extremely efficient in the destruction of ozone.

$$ClONO_2 + HCl \rightarrow Cl_2 + HNO_3 \qquad (1.19)$$

$$ClONO_2 + H_2O \rightarrow HOCl + HNO_3 \qquad (1.20)$$

$$N_2O_5 + HCl \rightarrow ClNO_2 + HNO_3 \ . \qquad (1.21)$$

The Cl_2, HOCl, and $ClNO_2$ molecules released by reactions (1.19), (1.20), and (1.21) are easily photolyzed when the sun returns to release forms of chlorine that efficiently destroy ozone in the reactions below. Furthermore, the HNO_3 formed is unreactive to ozone and if the aerosols containing nitric acid are large enough, they will settle out of the stratosphere further reducing active nitrogen that could otherwise prevent the halogen (chlorine and bromine) catalytic cycles shown below from raging.

There are two major catalytic cycles involving the

halogens Cl and Br. Both require high concentrations of ClO which are normally prevented by reaction (1.19). The first with Cl,

$$2x(Cl + O_3 \rightarrow ClO + O_2) \tag{1.22}$$

$$ClO + ClO + M \rightarrow Cl_2O_2 + M \tag{1.23}$$

$$Cl_2O_2 + h\nu \rightarrow Cl + ClO_2 \tag{1.24}$$

$$ClO_2 + M \rightarrow Cl + O_2 + M \tag{1.25}$$

$$net \quad 2O_3 + h\nu \rightarrow 3O_2 \tag{1.26}$$

and the second with Cl and Br,

$$BrO + ClO \rightarrow Br + Cl + O_2 \tag{1.27}$$

$$Br + O_3 \rightarrow BrO + O_2 \tag{1.28}$$

$$Cl + O_3 \rightarrow ClO + O_2 \tag{1.29}$$

$$net \quad 2O_3 + h\nu \rightarrow 3O_2 \ . \tag{1.30}$$

Under normal (unperturbed) conditions, there are sufficient concentrations of NO_2 to react with ClO to prevent this molecule from accumulating

$$NO_2 + ClO + M \rightarrow ClONO_2 + M \ . \tag{1.31}$$

This prevents the two catalytic cycles above from occurring.

ClO is more efficient than NO at destroying ozone.

Third, it has been suggested that heterogeneous reactions of several nitrogen oxides (for instance N_2O_5 and $ClONO_2$) occur on sulfate aerosols at temperatures higher than those required for the formation of PSCs [*Hofmann and Solomon,* 1989]. These reactions result in a reduction of the NO_2 concentration, making ozone losses possible [*Pitari and Visconti,* 1991; *Solomon and Keys, 1992; Johnston et al.,* 1992; *Mills et al.,* 1993]. These reactions are more important in the wake of the large enhancement of stratospheric aerosol due the 1991 Pinatubo volcanic eruption [*McCormick et al.,* 1992].

1.4: The Ozone Layer

Although ozone is of great importance in the radiative heat balance of the stratosphere [*Andrews et al.,* 1987], it is a trace gas with its total column abundance amounting to only about 3 mm at standard temperature and pressure. Figure 1.1 shows a typical late winter Arctic ozone profile in terms of partial pressure (mPa) versus height taken in the Scandinavian Arctic above Ny Alesund, Svalbard (79°N) using a balloon-borne ozonesonde [*R. Neuber,* private communication, 1992].

Ozone absorbs strongly in the Hartley bands from 200 to 300 nm and in the Huggins bands from 300 to 360 nm, thereby

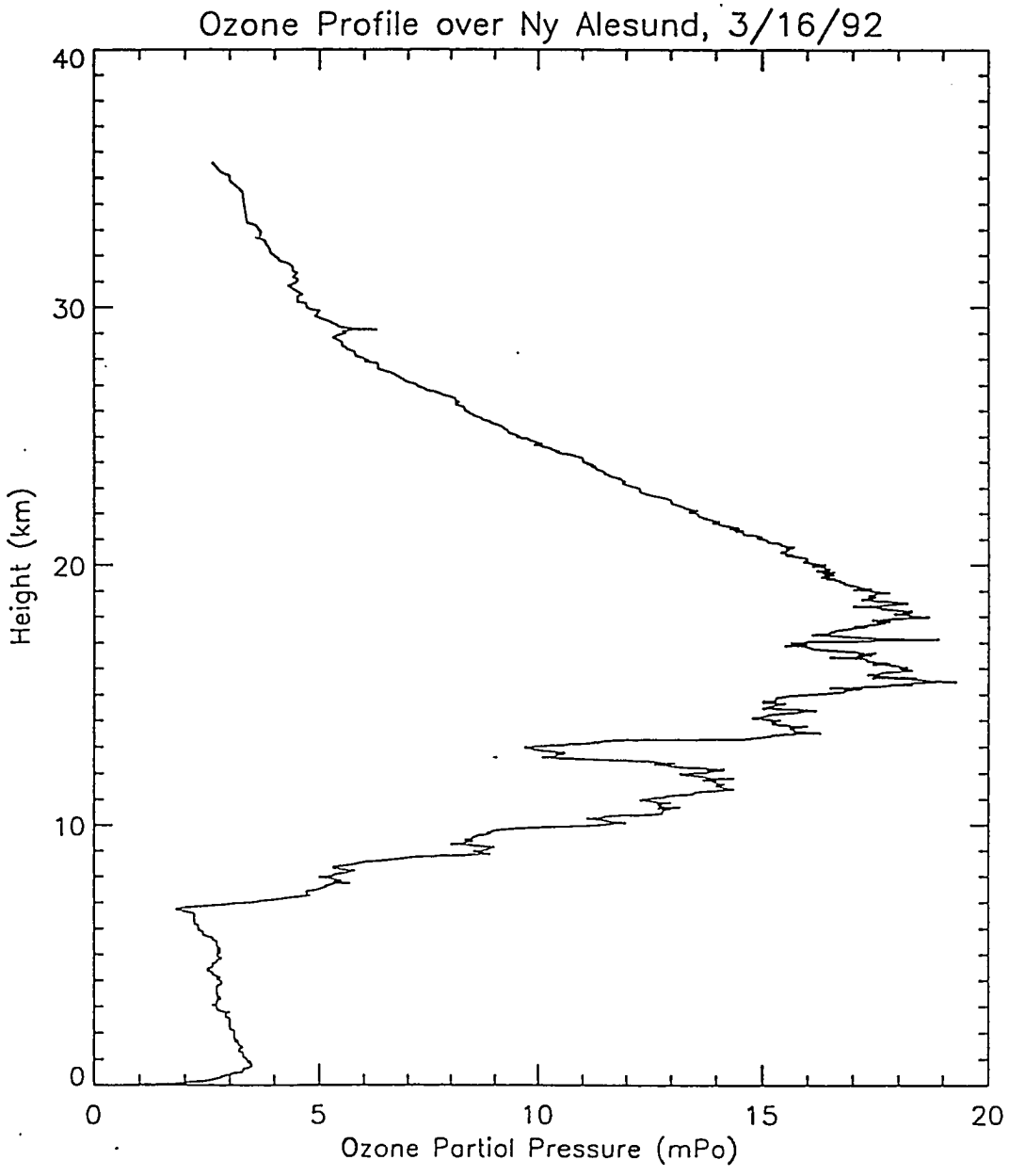

Figure 1.1: Ozone partial pressure as a function of altitude at a location in the Scandinavian Arctic (79° N). Data was supplied by the Alfred Wegner Institute of Bremen, Germany. Measurements were made using an ozonesonde.

blocking ultraviolet radiation which if unchecked would damage living organisms. Ozone also has broad but weak absorption between 450 and 800 nm known as the Chappuis bands. Figure 1.2 (bottom) shows the ozone absorption cross section versus wavelength from 200 to 800 nm with the Hartley and Huggins bands as well as the Chappuis bands [*Molina and Molina,* 1986]. Figure 1.2 (top) shows the solar irradiance at the top of the atmosphere versus wavelength [*Nicolet*, 1989].

Massive depletions of ozone over Antarctica have been observed by *Farman et al.* [1985] with a ground-based Dobson spectrophotometer, *Stolarski et al.* [1985] using the satellite Total Ozone Mapping Spectrometer (TOMS), and later by *Deshler et al.* [1990] who made *in situ* measurements with ozonesondes. These ozone losses have resulted in large increases in ultraviolet radiation reaching the biosphere [*Lubin et al*, 1989; *Stamnes et al.*, 1990]. The Arctic has thus far escaped such major depletions due to warmer stratospheric temperatures that prevent the extensive formation of PSC's, and more thorough mixing of trace gases from lower latitudes [*Webster et al.*, 1993; *Wilson et al.*, 1993]. Because of increasing global levels of chlorine compounds in the stratosphere [*Brasseur and Granier,* 1990], there is mounting concern that the occurrence of a much colder than normal Arctic winter stratosphere could be

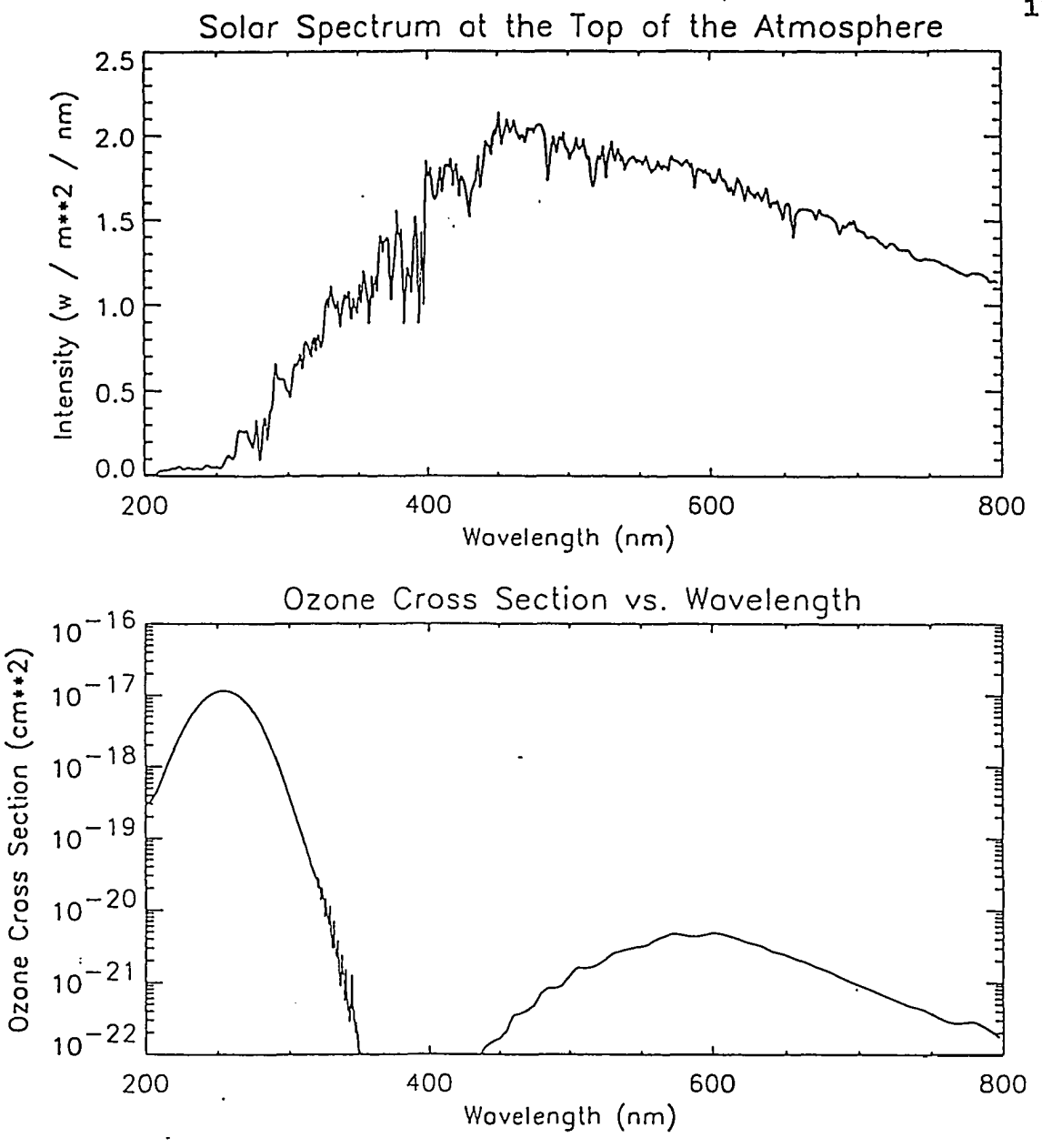

Figure 1.2: Solar spectrum at the top of the atmosphere (top).
The ozone absorption cross section is shown in the bottom figure.

accompanied by major ozone depletions over the Arctic.

1.5: Overview of the Work

Chapter 2 will discuss the optics, electronics, and software of the University of Alaska Fairbanks' spectrograph used to record the spectra of scattered light. The analysis of these spectra to reliably retrieve slant column abundances of NO_2 and estimate the errors will form the basis of Chapter 3. Air mass values are needed to convert measured slant columns to the vertical column abundances used by modelers. These computations will be discussed in Chapter 4, including the effects of stratospheric aerosols. Chapter 5 will treat the retrieval of vertical profiles from a twilight time series of measured NO_2 slant column abundances.

Chapter 6 contains a discussion of experimental results obtained during a six month campaign during the winter of 1992-93 at Fairbanks, Alaska. NO_2 slant column abundance was measured to study diurnal and seasonal behavior, and to investigate possible conversion of nitrogen oxides to nitric acid on surfaces of sulfate aerosols [*Solomon and Keys*, 1992; *Johnston et al.*, 1992]. Results and areas for future research are presented in chapter 7.

Chapter 2

Experimental Description

2.1 Optical Setup

The objective is to derive NO_2 abundances by looking at its absorption of sunlight impinging on top of the atmosphere. Stratospheric NO_2 vertical column abundances, N, are typically about 3×10^{15} cm^{-2} and at 450 nm the NO_2 absorption cross section for photodissociation, σ, is 5.0×10^{-19} cm^2 [*H. Johnston,* unpublished, 1977]. This leads to an optical depth (a dimensionless quantity) of $\tau = \sigma N$ of 1.5×10^{-3}. The corresponding absorption of 1.5×10^{-3} is easily estimated by Beer's Law

$$I = I_o e^{-\tau} \approx I_o(1 - \tau) \qquad (2.1)$$

where I is the intensity ($W/m^2/nm$) of the direct beam at ground level, I_o is the intensity outside the earth's atmosphere, and τ is the optical path due to the presence of NO_2. This absorption can be increased by having the light travel a longer path, length l (cm), through the absorber

$$\tau = n\sigma l \qquad (2.2)$$

where n ($molecules/cm^3$) is the molecular density of the absorber. The absorption is increased by a factor of 20 if instead of looking at the overhead direct beam, scattered twilight from the zenith is observed. This twilight

absorption due to NO_2 is of the order of 1 to 3% which is sufficient to extract column abundance from the observations. This magnitude of absorption is in theory not hard to measure if one takes the ratio of a long path spectrum taken at twilight to a short path spectrum taken at noon. The solar spectrum itself is complicated and has absorption features that are about 10 to 15% of the maximum intensity, making wavelength alignment between the two spectra critical if the absorption structure of NO_2 is to be discernible in the ratio.

The absorption structure of NO_2 is about 1 nm wide. *Brewer et al.* [1973] and *Noxon* [1975] demonstrated that a spectrometer with similar resolution could resolve stratospheric NO_2 near 450 nm using scattered twilight. The instrument for measuring NO_2 needed to be accurate, fairly portable, and reasonably priced. Furthermore, for a particular instrument and grating, the light reaching the detector is inversely proportional to the square of the focal length of the focusing element between the entrance slit and the grating, precluding too long a focal length. Too short a focal length means poor resolution. This suggested using a spectrometer of fairly short (less than 0.5 m) focal length.

Next the choice had to be made between the two methods of UV-visible atmospheric differential optical absorption

spectroscopy in current use: an imaging spectrograph using a photodiode array as a detector or a scanning spectrometer using a single photomultiplier as a detector. Array systems have a stationary grating so each photodiode receives light of a fixed bandpass throughout the measurement period, and subsequent measurements. Thus, when one takes the ratio of two spectra measured by a photodiode array spectrograph, there is less wavelength realignment required since the grating has remained stationary. The fixed grating is also advantageous because it avoids the mechanical deterioration inevitable in scanning systems. Two drawbacks of array systems are that individual photodiodes are less sensitive to light than the single high voltage photomultiplier used in scanning systems and the array must be calibrated for the variation of response of each photodiode.

The choice of instruments was discussed with Dr. George Mount of the National Oceanic and Atmospheric Administration (NOAA) Aeronomy Laboratory who designed the spectrograph used by *Mount et al.* [1987] to measure stratospheric NO_2 and later BrO and OClO [*Solomon et al.*, 1988]. Given the amount of money available, and the short time available to develop the instrumentation, Dr. Mount suggested the purchase of a spectrograph which could be fitted with a photodiode array detector. These considerations led to the acquisition of a 0.275 m Czerny-Turner monochromator (Acton Research

Corporation, Acton, MA) with a 1024 pixel photodiode array (Princeton Applied Research Corporation/EG&G, Princeton, NJ). Table 2.1 summarizes relevant parameters for the optical system.

Table 2.1: Parameters of Spectrograph System

focal length	0.275 m
detector	1024 element photodiode array
pixel dimensions	2.5 μm x 2.5 mm
slit width	250 μm
grating	1200 gr/mm blazed at 500 nm
configuration	Czerny-Turner

Figure 2.1 shows the optical layout of the system. The instrument was deployed on the roof of the Geophysical Institute and pointed to the zenith. The chosen spectrograph has a half angle field of view for the extreme rays of 8.3° x 10.3°.

The angular dispersion of a grating spectrometer may be determined by differentiating the grating equation

$$\frac{\partial}{\partial\beta}\left[\, d(\sin\alpha+\sin\beta) \;=\; m\lambda \,\right] \qquad (2.3)$$

where α and β are the angles the incoming and outgoing rays,

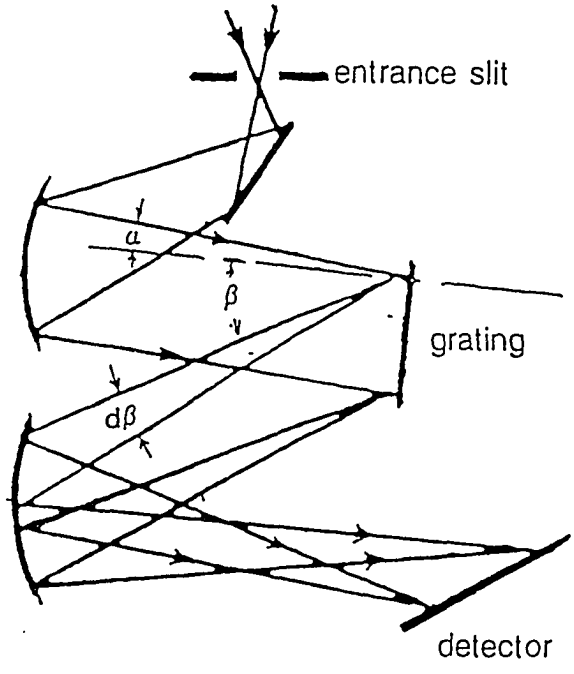

Figure 2.1: Optical layout of Czerny- Turner spectrograph. There is a second plane mirror just before the detector that has been omitted for clarity.

respectively, make with the optical axis of the grating (as shown in Figure 2.1), m is the order number, λ is the wavelength, and d is the distance between the grooves of the grating. Since α does not vary, Eq. 2.3 reduces to the angular dispersion

$$\frac{\partial\beta}{\partial\lambda} = \frac{m}{d\cos\beta} \quad . \tag{2.4}$$

In the first order utilized here, the angular dispersion is roughly proportional to the difference in wavelength since and for the small angles used, $\cos\beta$ is nearly constant. The resolution of a spectrometer, $\delta\lambda$, is the smallest difference between two wavelengths of light before the diffraction patterns due to the entrance slit merge at the focal plane. Using Rayleigh's criterion that the maximum of one wavelength's diffraction pattern coincide with the minimum of the other leads immediately to the resolution relation [*Hutley,* 1982]

$$\delta\lambda = \frac{s}{f_1}\frac{d\lambda}{d\beta} \tag{2.5}$$

where f_1 is the focal length of the first mirror, s is the slit width, and $(d\lambda/d\beta)$ is the inverse angular dispersion from Eq 2.4. A slit width of 250 μm was chosen to give a resolution of 0.73 nm using the 1200 groove /mm grating. Figure 2.2 shows the response of the spectrograph to monochromatic light at 435.8 nm. The width of the

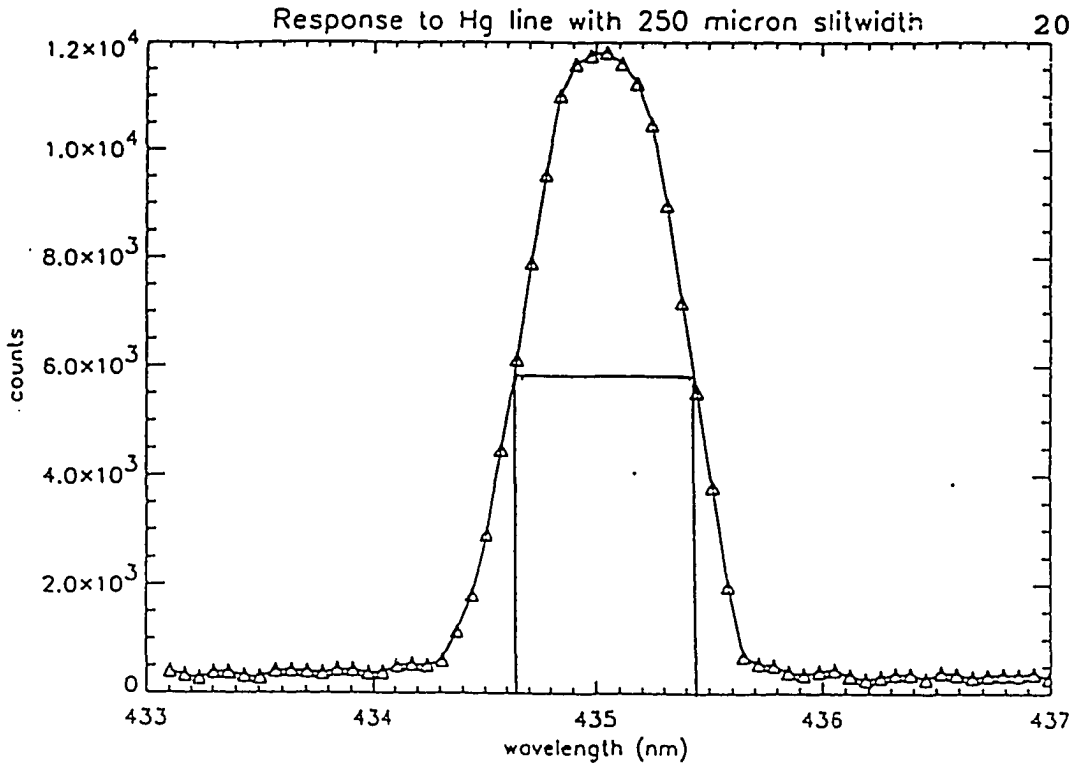

Figure 2.2: Response of the spectrograph to the Hg line at 435.8 nm. This response function will be used to smooth the cross sections and measured spectra used in analysis.

spectrograph response to this line is 0.76 nm, in agreement with theory outlined above.

The width of the NO_2 absorption features to be resolved is roughly 1.0 nm, so the slit width chosen reflects a compromise between light to the detector and resolution. If the slit were much wider, wavelength calibration using the solar Fraunhofer lines discussed in Chapter 3 became difficult; a narrower slit resulted in less light to the detector. As much light as possible reaching the detector is desirable in deep twilight. With the chosen slit width, measurements could be made to solar zenith angles of 95°. A resolution of 0.76 nm and a centerline of diode to diode wavelength spacing of 0.069 nm resulted in 11 pixels sampling the resolved wavelength region.

2.2: System Software and Control Electronics

Figure 2.3 shows a block diagram of the optical system. Spectra were taken ever 10 minutes and stored. Appendix A gives a description of the detector and the components to control the spectrograph. Also included in Appendix A is the method to cool and prevent condensation on the detector. Appendix B gives the Fortran source code for controlling the experiment.

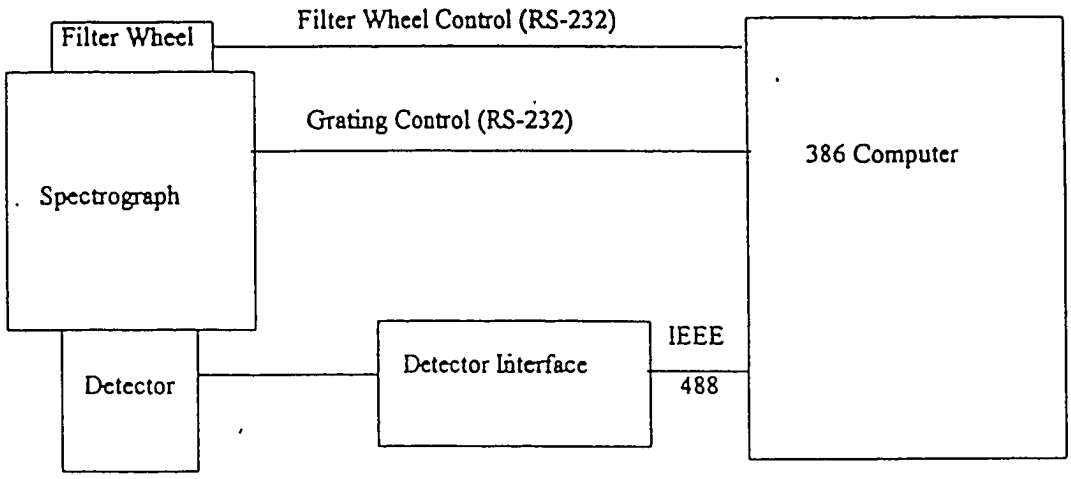

Figure 2.3: Block diagram of the optical system, showing the spectrograph, filter wheel, detector, detector interface unit, and computer.

Chapter 3

Experimental Analysis

3.1: Retrieval Procedure

3.1.1 General Considerations

The long atmospheric optical paths for the sun's rays that are scattered from the zenith sky at twilight give rise to greater absorption from weakly absorbing gases compared to direct sun measurements at these solar zenith angles. *Brewer et al.* [1973] and *Noxon* [1975] pioneered the technique of using ground-based spectrometers to measure the absorption caused by stratospheric NO_2 by observing the zenith sky intensity during twilight. This technique for retrieving NO_2 slant column abundances relies on the ratio of a twilight (long path) spectrum for which absorption is large to a high sun (local noon) spectrum which has much less absorption because of the shorter optical path. The twilight spectrum is hereafter referred to as the observation and the noon spectrum the control. The aim is to determine the actual NO_2 slant column abundance, β_{actual}, which is the sum of the NO_2 observed, β_{obs}, and the amount in the control, $\beta_{control}$,

$$\beta_{actual} = \beta_{obs} + \beta_{control} \quad . \tag{3.1}$$

Although NO_2 is by far the strongest absorber in the blue region of the spectrum (400-470 nm), there are also weak absorptions due to ozone and water vapor, as well as atmospheric and optical effects that can be treated as additional absorbers. Thus, the abundance of a number of absorbers will be determined. Effective determination of the amounts of these absorbers requires the use of multiple wavelengths.

Following the work of *Harrison* [1979] it is assumed that the ratio of zenith intensities of wavelength λ at twilight, $I(\lambda)$ to midday, $I'(\lambda)$ can be written as

$$\left(\frac{I}{I'}\right)_\lambda = (a + b\lambda)\exp\left[-\sum \sigma_{\lambda i}\beta_i\right] \qquad (3.2)$$

where β_i (cm^{-2}) is the difference in the slant column abundance between the actual slant column abundance and the control for the ith absorber as in Eq. 3.1, $\sigma_{\lambda i}$ is the absorption cross section at wavelength λ of the ith absorber, and a and b are constants which express the differences in scattering geometries between twilight and midday. Over a short wavelength interval of about 50 nm, Eq. 3.2 can be written for a number of wavelengths as [*McKenzie and Johnston*, 1982]

$$\ln\left(\frac{I}{I'}\right)_\lambda = -\left(\left(\sum \sigma_{\lambda i}\beta_i\right) + \lambda S + C\right) + e_\lambda \qquad (3.3)$$

where S and C are new linear constants and e_λ is the individual residual error. For a multi-wavelength fit, e^2 summed over wavelength is called the residual.

The linear trend of the log ratio spectrum and the absorption cross sections of Eq. 3.3 are removed (detrended) by subtracting the fitted values of a linear regression line. The linear trends of the measured spectra and cross sections can result in bias caused by correlation of the linear component of the ozone and Rayleigh terms. The deviations from the regression lines are noted as primes and follow the relation

$$\ln\left(\frac{I}{I'}\right)'_\lambda = -\left(\sum \sigma'_{\lambda i}\beta_i\right) + e_\lambda \ . \qquad (3.4)$$

The slant optical path τ_{avg} is the product of the slant column abundance β (cm^{-2}) and the absorber cross section σ (cm^2),

$$\tau_{avg} = \sigma\ \beta \ . \qquad (3.5)$$

3.1.2: Physical and Mathematical Framework

The code developed by Mr. Paul Johnston and Dr. Richard McKenzie [*P. Johnston*, private communication, 1992] of New Zealand's National Institute of Water and Atmosphere (NIWA) at Lauder for obtaining NO_2 column abundances from spectrometer measurements [*McKenzie and Johnston*, 1982,

1984] was kindly made available to us. This analysis program is a multi-wavelength least squares fitting algorithm which varies absorber amounts until the best fit is achieved between the measured log ratio (the left-hand side of Eq. 3.4) and the reconstructed spectra (the right-hand side of Eq. 3.4). The best fit means that the sum of the squares of the residuals is minimized.

A quantitative description of the trend analysis follows. To determine the slant column abundances of the N absorbers x_n (corresponding to β_i in Eq. 3.4), M simultaneous equations are solved, one for each wavelength m. g_m is the detrended log intensity ratio from Eq. 3.4 at wavelength m ($\ln(I/I')_\lambda$), a_{mn} is the cross section ($\sigma_{\lambda i}$) of the nth absorber, and e_m is the individual residual at wavelength m,

$$\sum_{n=1}^{N} a_{mn}\, x_n - g_m = e_m \ . \tag{3.6}$$

The sum of the squared residuals, E, is

$$E = \sum_{m=1}^{M} e_m^2 \tag{3.7}$$

or

$$E = \sum_{m=1}^{M} [\sum_{n=1}^{N} a_{mn} x_n - g_m]^2 \ . \tag{3.8}$$

To minimize E by varying the absorber amounts x_n requires that the first derivative of E with respect to each absorber is zero and the second derivative is negative

$$\frac{\partial E}{\partial x_1} = \frac{\partial E}{\partial x_2} = \ldots = \frac{\partial E}{\partial x_n} = 0 \ . \tag{3.9}$$

Performing the differentiation yields

$$\begin{aligned}
\frac{\partial E}{\partial x_1} &= \sum_m a_{m1}a_{m1}x_1 + \ldots + \sum_m a_{m1}a_{mn}x_n - \sum_m a_{m1}g_m = 0 \\
\frac{\partial E}{\partial x_2} &= \sum_m a_{m2}a_{m1}x_1 + \ldots + \sum_m a_{m2}a_{mn}x_n - \sum_m a_{m2}g_m = 0 \\
&\vdots \\
\frac{\partial E}{\partial x_n} &= \sum_m a_{mn}a_{m1}x_1 + \ldots + \sum_m a_{mn}a_{mn}x_n - \sum_m a_{mn}g_m = 0 .
\end{aligned} \tag{3.10}$$

These equations can be written in matrix form as

$$\begin{vmatrix} (\sum_m a_{m1}a_{m1}) & \ldots & (\sum_m a_{m1}a_{mn}) \\ (\sum_m a_{m2}a_{m1}) & \ldots & (\sum_m a_{m2}a_{mn}) \\ & \vdots & \\ (\sum_m a_{mn}a_{m1}) & \ldots & (\sum_m a_{mn}a_{mn}) \end{vmatrix} \begin{vmatrix} x_1 \\ x_2 \\ \\ x_n \end{vmatrix} = \begin{vmatrix} (\sum_m a_{m1}g_m) \\ (\sum_m a_{m1}g_m) \\ \\ (\sum_m a_{mn}g_m) \end{vmatrix} \tag{3.11}$$

or in shorthand notation as

$$\tilde{A}\vec{x} = \tilde{B}. \tag{3.12}$$

This matrix equation can be inverted to yield the solution vector

$$\vec{x} = \tilde{A}^{-1}\,\tilde{B}\ . \tag{3.13}$$

The magnitude of the residual gives an estimate of the uncertainty of the measurement if the errors are random. Since the errors are not random, the magnitude of the residual is only a rough indication of the magnitude of the errors.

3.1.3: Retrieval Algorithm

If the short path and long path spectra were perfectly aligned with respect to wavelength, the large Fraunhofer absorption features common to both would disappear when their ratio was taken. However, because of small wavelength misalignments between the spectra, this is rarely the case. The solar Fraunhofer absorptions are of the order of 15% of the overall solar blackbody envelope compared with absorptions of scattered twilight due to NO_2 and O_3 which are about 1%. This implies that Fraunhofer structure will obscure the weaker absorptions in the ratio spectra if the two are not precisely aligned. Misalignments due to temperature fluctuations in the vicinity of the spectrograph change the grating dispersion and the optical path of the

spectrometer which in turn cause large apparent absorption structures due to the solar lines in the ratio spectra, obscuring the smaller absorption due to NO_2 or O_3.

It is therefore imperative to have an analysis technique which can adjust (called *shift*) as well as compress or expand (called *stretch*) the wavelength scale of one spectra with respect to the other to compensate for the misalignment. The shift algorithm moves the wavelength scale of a spectrum, then interpolates the intensity values to the shifted spectrum's *old* wavelength values. This allows the ratios to be taken at the same wavelengths. The stretch procedure changes the wavelength spacing between samples which also requires interpolation of intensities to the old wavelengths of the stretched spectrum. The interpolations consist of a 3-point fit which is a compromise between the less accurate 2-point and more noisy higher order interpolation. In the absence of shift and stretch, simply taking the ratio of the two spectra and performing a least squares fit will yield unsatisfactory NO_2 retrievals.

To align two spectra, the following algorithm was used. Consider two arrays, x_i and y_i, to be aligned on the interval i= b to e, where i represents pixel number. First, the slope of the two arrays is removed. Next, the correlation is calculated for various incremental shifts, k,

of one array with respect to another,

$$Corr(l) = \sum_{i=b}^{e} y_i x_{i+1} + x_i y_{i-1} \ . \qquad (3.14)$$

The three largest Corr(l) values are taken and by quadratic interpolation the fractional shift index of maximum correlation k.a. is found. Next, x_i is shifted by the fractional k.a just determined and the alignment procedure repeated until Corr(l) attains a stable maximum.

The steps to derive NO_2 slant column abundances are as follows. The fine resolution reference solar spectrum [*Delbouille*, 1973] and cross section absorption spectra are filtered with the instrument's transmission function to allow more effective alignment of these spectra with the ratio spectrum measured by the instrument. Filtering also allows a better multi-wavelength fit between the right-hand side and the left-hand side of Eq. 3.4. The spectrograph's transmission function is characterized by recording the spectrum of a Hg line at 435.8 nm with the entrance slit width set at 250μm. Filtering the solar spectrum or cross sections $F(\lambda')$ with the transmission function $T(\lambda)$ requires solution of the quotient

$$F_f(\lambda') = \frac{\int F(\lambda'+\lambda)\ T(\lambda)\, d\lambda}{\int T(\lambda)\, d\lambda} \tag{3.15}$$

where the integral limits are over all $T(\lambda)$ that are non-zero, F is the input unfiltered function, and F_f is the output filtered function. These integrations are done numerically with a finite step size $\delta\lambda$ replacing $d\lambda$. The step size of the filtering $\delta\lambda$ must be less than the sampling spacing of the reference Fraunhofer or cross section spectra. The solar spectrum and the absorbing cross sections are interpolated to give values at the required $\delta\lambda$ spacings.

Next, the control path spectrum, typically taken at noon when the absorption is small, is shifted with respect to the reference solar spectrum to achieve the best possible alignment with the cross sections used. The log ratio spectrum, as well as these cross sections, were detrended as described above.

This observational spectrum is then shifted to align it with the control spectrum. The log ratio of the observation to control spectra is determined and Eq. 3.13 solved for absorber amounts. A synthetic spectrum is constructed by inserting the various slant column absorber amounts just determined into the right hand side of Eq. 3.4 for M wavelengths and the residuals determined. Shift and

stretch are varied sequentially, and the alignment and calculation sequence repeated. Molecular absorber amounts are again determined and the whole process repeated until the sum of the squared residuals is minimized. The size of the residual is a measure of the goodness of fit. It was found to be satisfactory to vary stretch and shift independently because these two variables were sufficiently uncoupled to allow finding a solution without varying them simultaneously.

Another factor that influences the retrieval of NO_2 and ozone is the Ring Effect [*Grangier and Ring,* 1962] which may be treated in Equation 3.6 as another absorption cross section. As the solar zenith angle increases, there is a progressive filling in of the Fraunhofer minima described by *Ginzberg* [1972], and *Kattawar et al.* [1981]. It is caused by density and velocity fluctuations of molecules in the atmosphere leading to slight changes in the wavelength of the light due to Doppler shifts. *Noxon et al.* [1979] accounted for the effect by adding a small offset to the twilight spectrum. It is approximated in the NIWA software by a pseudo-cross section generated from the inverse of the Fraunhofer solar spectrum as described by *Johnston and McKenzie* [1989]. A second Ring "cross section" used by the NIWA algorithm is generated by taking the ratio of clear to cloudy controls. The Ring Effect will be further discussed

below in section 3.2.

3.1.4: Determination of Cross Sections

To determine the exact shape and wavelength position of the NO_2 absorption lines, light was observed after passing through an NO_2 absorption cell. The cell was placed over the spectrograph entrance slit, zenith scattered sunlight was passed through this cell, and a spectrum was recorded (the observation spectrum). By removing the cell an NO_2-free reference spectrum was acquired (the control spectrum). The NIWA code was used to retrieve NO_2 column abundance. Figure 3.1 shows the spectrum reconstructed by inserting each solved for absorber amount *except* NO_2 into the right hand side of Eq. 3.4 (solid line) and solving for e_λ. This is compared with the absorption due to the NO_2 amount the determined by the code (dotted line). The NO_2 column abundance of 24.205 cm^{-2} was determined. The cell had 2070 ppmv of NO_2 diluted with air at approximately 1.0 ± 0.8 atm. Given the concentration and path length of the cell and the absorption due to the gas cell, a cross section of NO_2 is calculated which can be checked against those of *H. Johnston* [1977, unpublished data, supplied by *P. Johnston*, private communication, 1992] used in the least squares fitting program. The light through the absorption cell is attenuated as

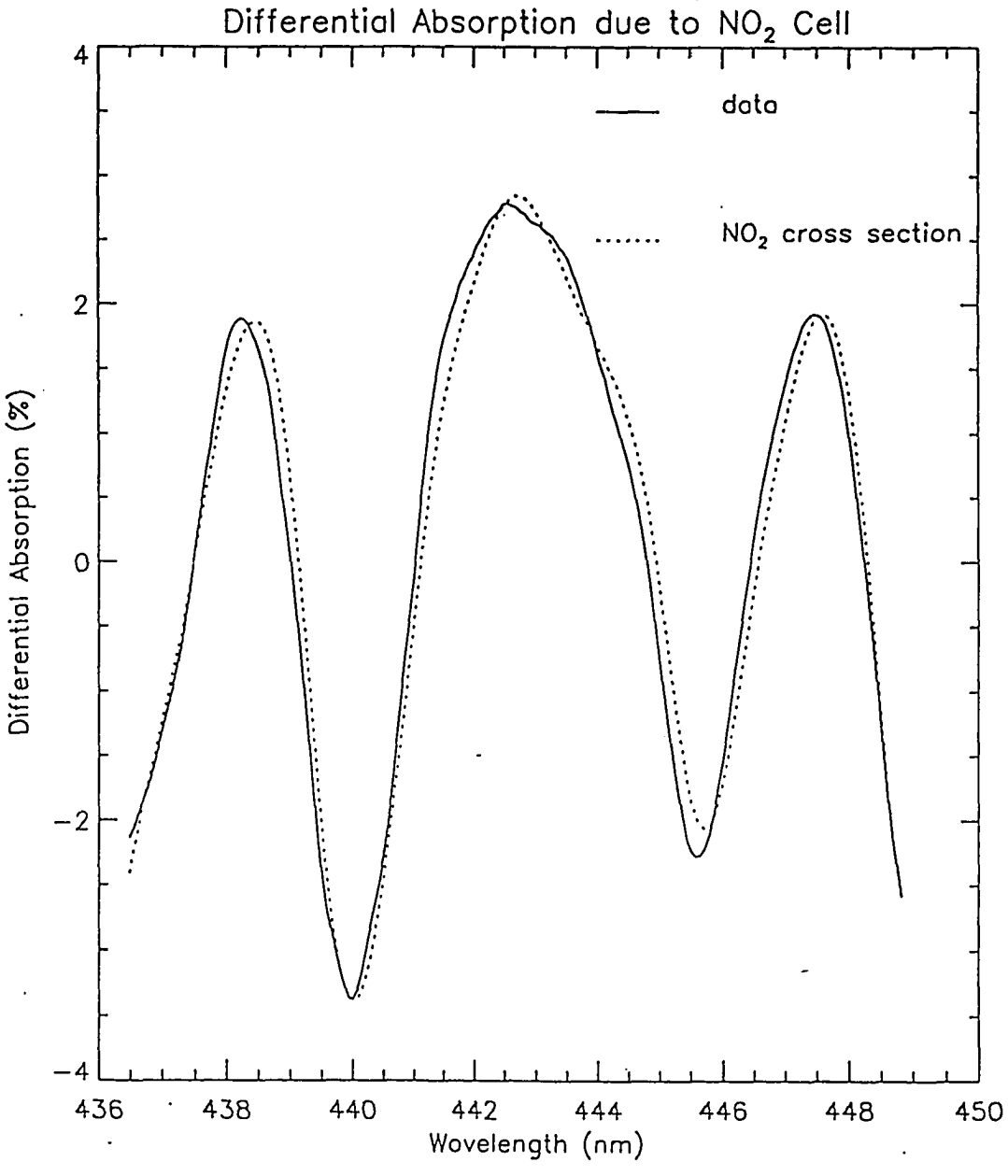

Figure 3.1: The absorption due to the NO_2 cell. The solid curve is the synthetic spectrum constructed with each absorber accounted for except NO_2. The dotted curve shows the absorption due to the H. Johnston NO_2 cross sections using the amount that was determined from the analysis program.

$$I = I' e^{-\tau} . \tag{3.16}$$

where I' and I are the intensities of light with and without the cell in place, respectively, and τ is the absorption optical path due to the NO_2. This leads to an expression for the absorption optical path, τ,

$$\tau = \ln \frac{I'}{I} . \tag{3.17}$$

τ may also be determined by the path length l (cm), the number concentration of the absorbing gas n (cm^{-3}), and the absorption cross section σ (cm^2) of NO_2

$$\tau = l\, n\, \sigma . \tag{3.18}$$

where n has been assumed to be constant in the cell. The uncertainties in calculating τ are associated with uncertainties in l (±1.0%), n (± 500%), I and I' (± 3%), which gives an overall uncertainty in σ of ± 500 %. The large uncertainty in n reflects the poor degree of knowledge of the amount of NO_2 in the cell. At the high concentration of NO_2 from the gas cylinder (2000 ppmv), evidently much of the NO_2 was actually N_2O_4 as will be described in section 3.2. A graph of cross section versus wavelength for the H. S. Johnston cross sections is shown in Figure 3.2 (top) and from the University of Alaska Fairbanks cell measurements

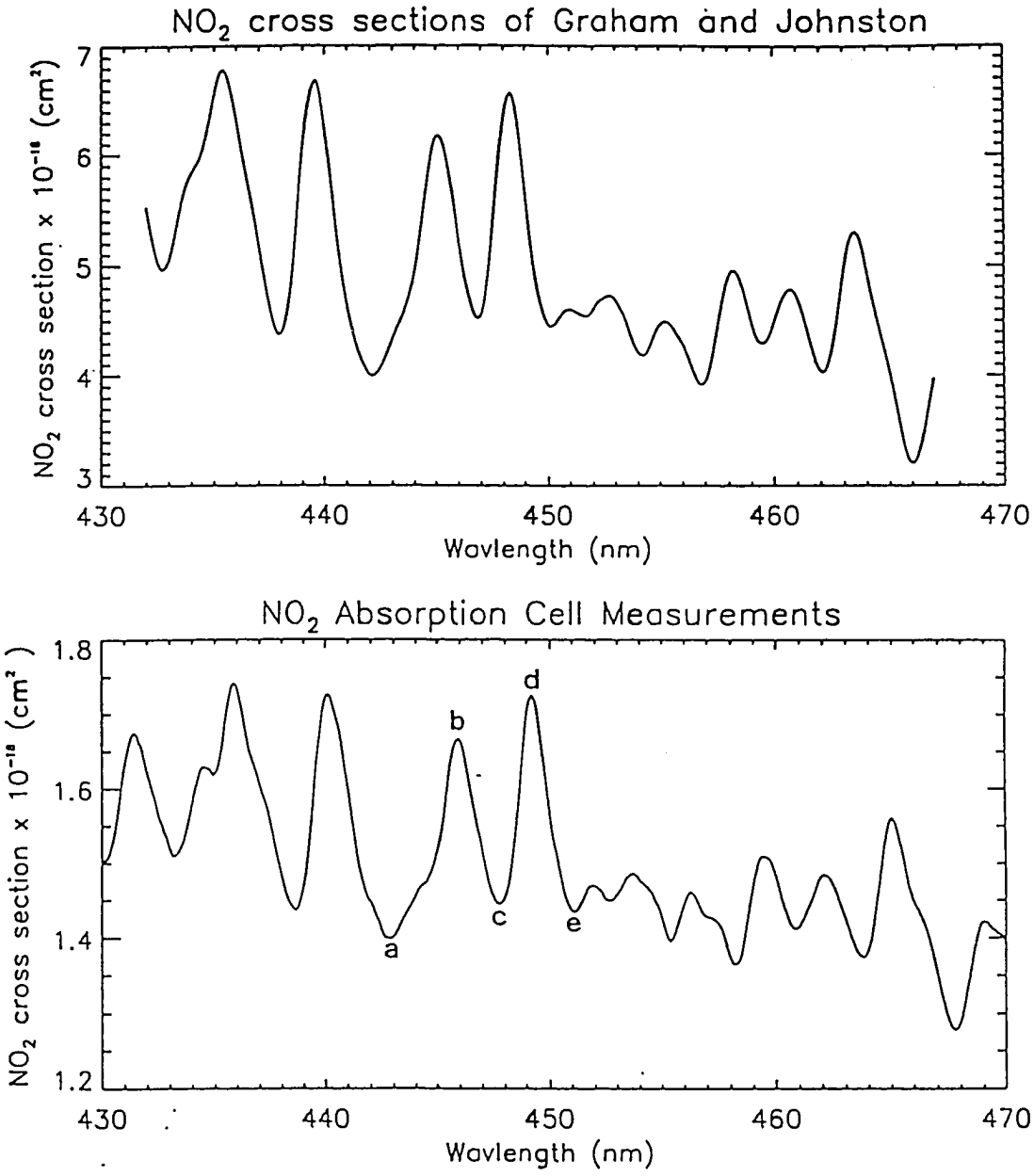

Figure 3.2: A comparison is shown of the NO_2 cross sections of Graham and Johnston (top) used in analysis codes, and absorption cell measurements made by the University of Alaska (bottom). The wavelengths of the minima and maxima labled a – e are found in Table 3.1.

(bottom). As is discernible by comparison of the two graphs, there is a small offset of approximately 1.0 nm and an average difference in cross sections of 400% between the two sets of measurements. The differences in the cross sections measured can be attributed to the high uncertainty of the NO_2 concentration in the absorption cell. The wavelength offset is investigated further. Table 3.1 shows a tabulation of λ for the minima and maxima labeled a, b, c, d, and e obtained by the University of Alaska spectrometer at various wavelengths compared with the cross sections and wavelengths measured by H. Johnston. Offsets of this magnitude are not serious because of the alignment procedures in the NO_2 retrieval code.

Table 3.1: Comparison of University of Alaska Fairbanks and H. Johnston Cross Sections

letter	Graham and Johnston (nm)	UAF (nm)	difference (nm)
a	442.1	442.74	+0.62
b	445.1	445.95	+0.85
c	446.8	447.80	+1.00
d	448.2	449.23	+1.03
e	450.1	451.08	+0.98

3.2 Error Analysis

Vertical column abundances of NO_2 and O_3 obtained from spectrograph measurements contain uncertainties due to the measurement process and unknown effects in the atmosphere. These errors can be either relative which effect the magnitude but not the shape of a time series of measurements, or absolute which affect both the shape and magnitude of a time series of measurements. The errors can be grouped into six categories: 1) cross sections, 2) optical effects of the spectrograph, 3) transformation of light into an electrical signal, 4) sky effects including scattering, polarization, aerosols, and clouds, 5) software analysis artifacts, and 6) conversion of slant column to vertical column abundances. These errors are summarized in Table 3.2 and will be discussed in the sequence given.

The cross sections of H. Johnston were made at 25° C at NO_2 pressure extrapolated to 0.0 atm and have an estimated uncertainty of ± 10% at 450 nm [*A. Goldman,* 1993, private communication]. Stratospheric temperatures and pressures where NO_2 abundance reaches its maximum range from -20° to -90° C and from 50 mbar to 10 mbar, so these cross sections will be in error depending on the NO_2 temperature and pressure coefficient. This dependence results because NO_2

Table 3.2
Uncertainties in Vertical column NO_2 Retrievals at 90°

Factor	Estimated Uncertainty
1. Absolute cross sections of NO_2, O_3, O_4.	10 %
2. Temperature dependence of cross sections.	4 %
3. Wavelength accuracy of spectrometer: offset and linearity.	< 0.5 %
4. Thermal noise of background correction.	< 1 %
5. Changing detector temperature changes detector gain.	< 1 %
6. Pixel to pixel sensitivity: worst case.	< 0.5 %
7. Statistics of counting signal.	0.5 %
9. Polarization and Ring Effects.	< 3 %
10. NO_2 in control spectrum.	< 5 %
11. NO_2 / NO ratio changes as the sun sets requiring correction of NO_2 slant column.	< 5 %
12. Tropospheric NO_2 from pollution.	variable
13. Is the minimum residual in 9 space a local or an absolute minimum?	< 0.5 %
14. How sensitive the final NO_2 is to setting the other absorbers to zero.	< 0.5 %
15. Slant column to vertical column: uncertainty in air mass and profile.	10 %
16. Timing uncertainty: computer clock, what is the midpoint of the scan?	< 1 %
17. Uncertainty in calculating solar zenith angle (air mass error).	< 1 %

is in equilibrium with the dimer, N_2O_4

$$NO_2 + NO_2 \rightarrow N_2O_4 \qquad (3.19)$$

with the reaction shifting to the right at lower temperatures and higher NO_2 pressures. Since the N_2O_4 cross section is different than that of NO_2, its presence in NO_2 absorption cells leads to errors in the assumed concentration of NO_2, hence errors in these cross sections. *Roscoe and Hind* [1993] conclude in their summary of NO_2 cross section measurements that for other measurements made at temperatures and pressures similar to those at which Johnston's were made, considerable N_2O_4 was present. *Davidson et al.* [1988] measured the NO_2 cross section at pressures of less than 0.1 mbar using a 48.6 m cell at low pressures of NO_2 which vastly reduced the concentration of the dimer. The temperature dependence for the NO_2 cross section was measured by Davidson to be ± 4 % from 350 to 550 nm at temperatures between 232 and 398 K.

Next, consider the possible errors in assigning a wavelength to each individual pixel. Figure 3.3 shows the solar spectrum recorded with the spectrograph on 5/14/92 and aligned using the Fraunhofer lines at 410.1748 and 434.0475 nm. Table 3.3 shows some Fraunhofer lines with the known wavelengths and elemental solar absorptions [*Moore et al.*, 1966] compared with the wavelength assigned after

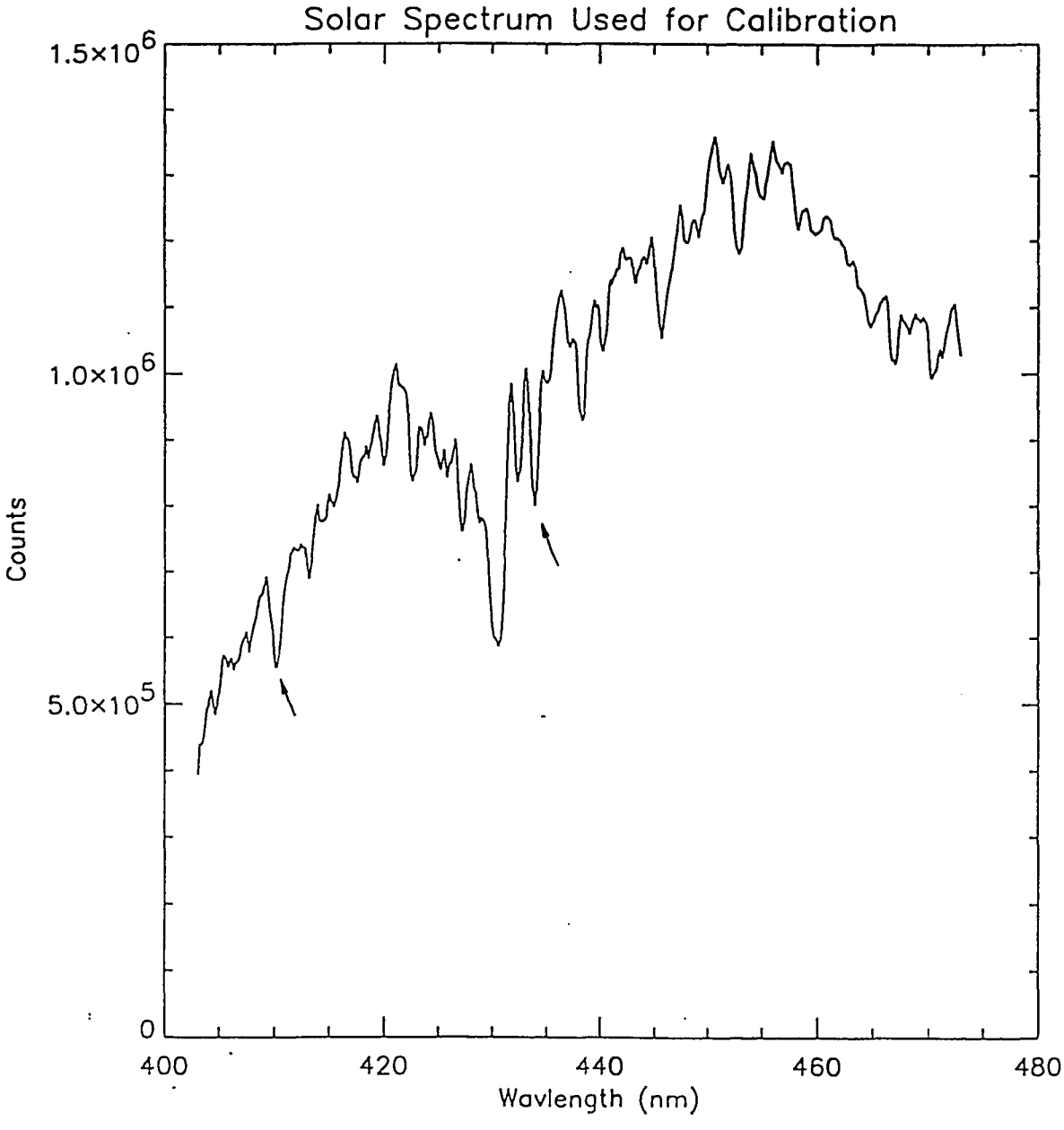

Figure 3.3: Measured solar spectrum used for wavelength calibration. The solar absorption lines at 410.1748 and 434.0475 nm were used.

calibrating the wavelength scale.

Table 3.3 Wavelength Accuracy of Spectrograph

Exact Solar Wavelength (nm)		Measured wavelength (nm)	difference (nm)
410.1748	Hδ	410.2440	+0.0692
422.6740	CaI	422.6262	-0.0330
434.0475	Hγ	434.0400	-0.0075
440.4761	FeI	440.4732	+0.0029
452.8627	FeI	453.2014	+0.3387
470.3003	MgI	470.9792	+0.6789

This particular spectrum was recorded some time after the wavelength calibration took place and the 410.1748 nm line no longer is correctly labeled. More importantly, it can be seen that the Fraunhofer lines beyond 450 nm are seriously misaligned implying that the dispersion is not linear (Eq. 2.4). This is not a serious a problem for a restricted range of wavelengths since the spectra are aligned to an Atlas Solar Spectrum. For the series of measurements presented in this work, the spectral range is restricted between 435 and 450 nm. Over this range, residuals are very low (< 0.02) which implies a very good fit. Thus, no error will be assigned to spectrograph wavelength offset and linearity. Attempts to fit over a wider spectral range, 435 to 460 nm, were unsuccessful.

Next, consider the errors involved in obtaining an electrical signal that ideally is directly proportional to the intensity of the light reaching the spectrograph detector. Photodiodes generate dark current due to the thermal recombination of electron hole pairs; this noise is proportional to $(kT)^{0.5}$ where k is Boltzmann's constant and T the temperature in Kelvin. This dark current, which must be subtracted from all subsequent measurements, is statistical in nature and may be assumed to have a Poisson distribution. Therefore the fractional uncertainty of n counts of dark current is $n^{0.5}/n$. Since the background correction was about 150,000 counts for an exposure time of 135 second, and at 90° solar zenith angle the corrected count was between 40,000 and 100,000, the uncertainty was ± 1.0 % to 0.4 % for each pixel. This uncertainty was studied further by taking one dark current measurement with an exposure of 135 s and subtracting it from 6 identical dark current exposures. The results of the six corrected exposures are shown in Table 3.4. The average standard deviation of the six exposures is 72.0 counts compared to the background standard deviation of 5119. Once the original background is subtracted from subsequent backgrounds, the standard deviation is greatly reduced because the even-odd gain difference in the amplifier circuit (described in Appendix A) has been removed for this

particular temperature. Thermal noise is random and for a constant temperature will not produce an overall offset to the derived measurement.

Table 3.4: Statistics for 135 s Background exposure

trial	mean value (counts)	standard deviation (counts)
1	1.4581×10^5	5.119×10^3
2	-1.4	43.9
3	4.7	57.6
4	3.7	59.2
5	19.5	77.2
6	25.5	86.6
7	25.9	91.0
avg.of 2-7	16.6	72.0

A more serious problem results from temperature changes of the photodiode between the time of the background correction and subsequent measurement. Dark current is measured to double for every 7° C increase in temperature; a 1° C increase results in a dark current increase of 9%. As will be shown below, this leads to an offset which causes errors in the amount of the absorber retrieved. Figure 3.4 shows background measurements taken at 440 nm for 1.35 s exposures at 293 K, 283 K, and 273 K. To investigate how an offset caused by changes in the background level, Ring

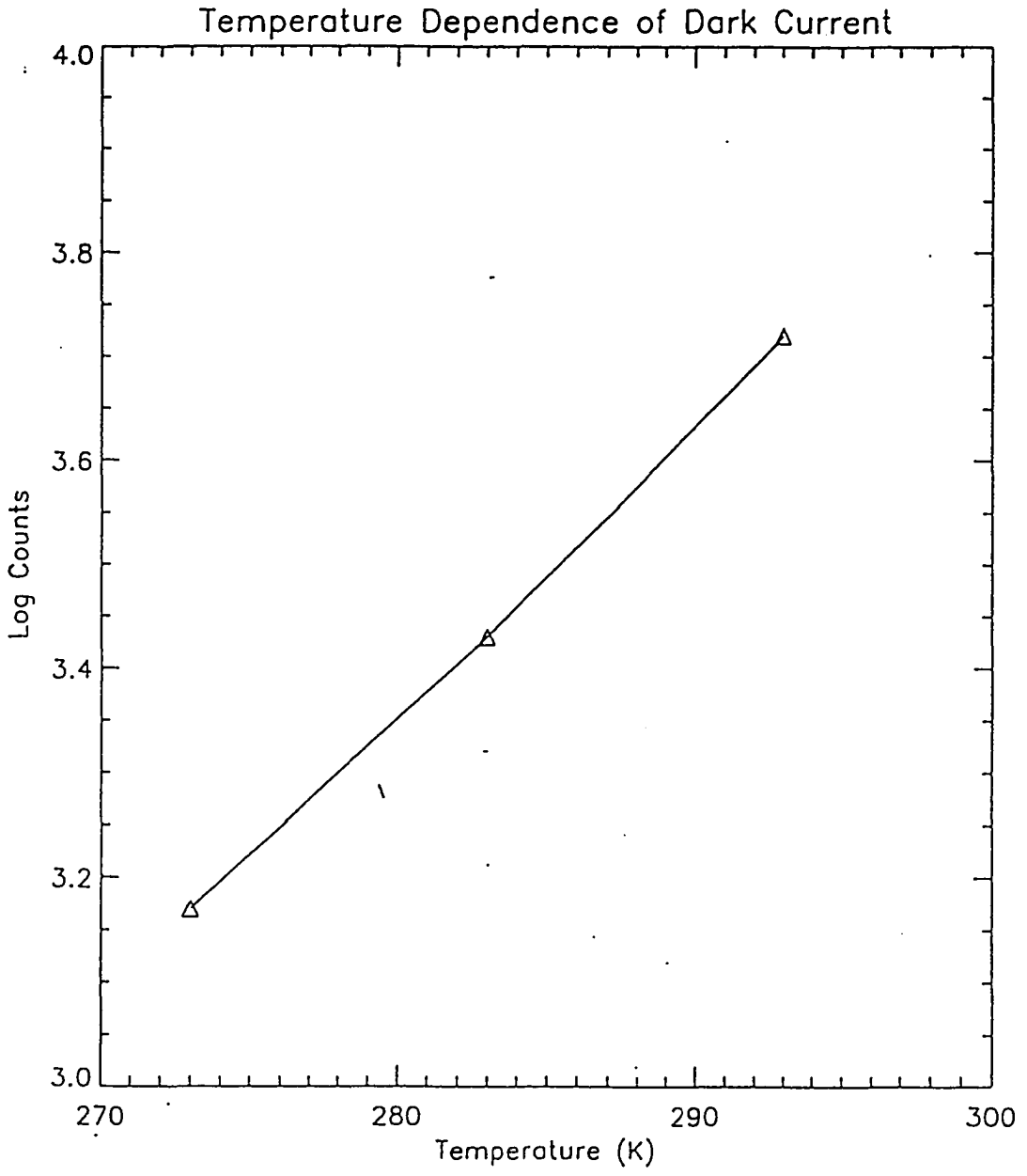

Figure 3.4: Dark current from exposures of 1.3 seconds for detector temperatures of 273 K, 283 K, and 293 K. Dark current is observed to double for each increase in temperature of 7 K.

Effect, or stray light, can affect retrievals, consider the case of an observation spectrum I with a nonzero offset C [*Johnston*, 1991],

$$I = I_o\, e^{-\tau} + C \tag{3.20}$$

and a control spectrum I' with an offset C',

$$I' = I'_o\, e^{-\tau'} + C' \tag{3.21}$$

with I_o and I'_o the solar spectra at the top of the atmosphere and τ and τ' are the atmospheric absorber optical depths. The unprimed quantities are the observations, and the primed are the control. The negative log ratio spectrum is

$$R = \ln(-\frac{I}{I'}) = \ln(I') - \ln(I) \ . \tag{3.22}$$

Now expand R in a Taylor's series, retaining only up to second order terms

$$R = h(1 - \frac{C}{I_o}) - h'(1 - \frac{C'}{I'_o}) + \ln(\frac{I}{I_o}) + (\frac{C'}{I'_o}) + f \tag{3.23}$$

$$where \quad f \approx \frac{1}{2}(\frac{C}{I_o})^2 + \frac{1}{2}(\frac{C'}{I_o})^2 \ . \tag{3.24}$$

These offsets produce an error in the $h(1 - C/I_o)$ term and cause inverse Fraunhofer shapes, $(C'/I_o' - C/I_o)$. It can be seen that a 5% increase of I relative to I_o caused by an offset, C, measured in the observation, I, yields a derived

absorber amount of 5% less.

Next, consider possible pixel to pixel variations in sensitivity. Figure 3.5 shows the spectrum of a 100 watt incandescent lamp placed in front of the spectrograph's entrance slit. The curve is smooth, but there is definite wave structure. This structure persists with the light scattered off of a diffusing screen in front of the entrance optics. However, this wave structure should have little effect on the retrievals since ratios are taken. Another factor affecting the measured signal are the statistical fluctuations of light which are well described by the Poisson distribution. Since twilight count rates are always greater than 50,000, this results in a statistical uncertainty of less than 0.5 %.

As mentioned before, the Ring Effect can to a first approximation be quantified by varying the offset term by less than 4% which will introduce Ring-like shapes which can be used to construct synthetic spectra that better fit the observed detrended ratio spectra. Another approach is to use a polarizer and record two sets of spectra with little time separation. Photons that have been subjected to the Ring Effect are expected to be unpolarized [*Solomon and Sanders*, 1987]. One measurement is taken with the entrance slit parallel to the line connecting the zenith and the sun, the other is taken with the entrance slit perpendicular to

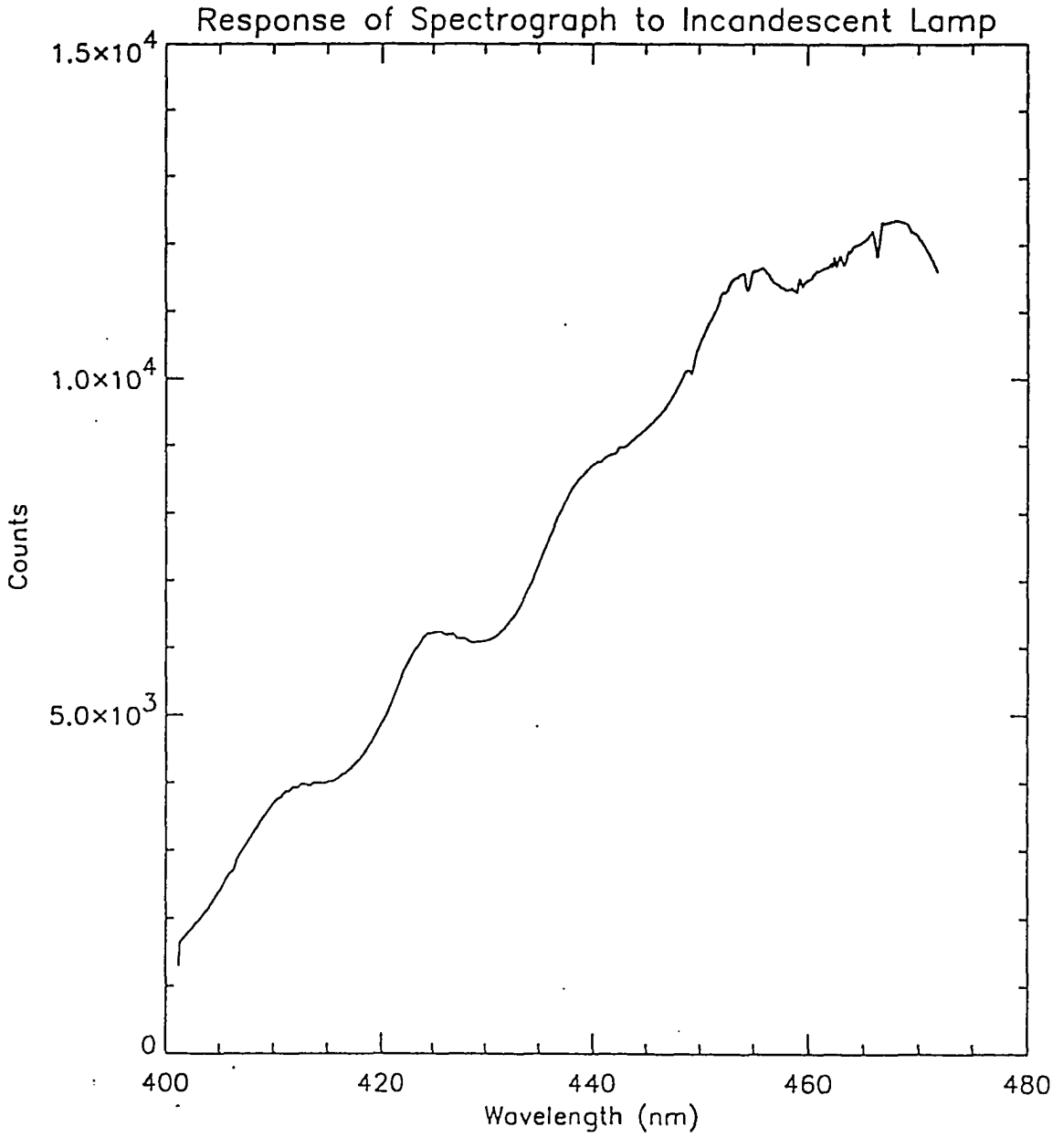

Figure 3.5: Response of spectrograph to an incandescent lamp.

this orientation. The ratio of these two spectra can be used to construct a Ring "cross section". Figure 3.6 (top) shows the results of such a set of measurements taken at Lauder, N.Z. on May 21, 1992. This is compared with Figure 3.6 (bottom) which shows the inverse of a spectrum recorded that same day. There are definite similarities to be noted.

There is also a grating polarization effect which can be quantified by varying the angle of a polarizer placed in front of the spectrograph pointed to the zenith. The resulting spectra are shown in Figure 3.7, (clear sky) and Figure 3.8 (partly cloudy sky), and 3.9 (cloudy sky). As expected, more light is transmitted through the polarizer from the cloudy sky which is less polarized than partly cloudy or clear skies. In all three cases, the most light is transmitted when the polarizer is at 180° or parallel to the entrance slit and hence also to the lines of the grating. Note that in Figure 3.7 and 3.8, there is an unexplained effect between 460 and 470 nm where several curves show different signs of concavity. This was investigated further by replacing the zenith skylight with randomly polarized incandescent light scattered off a white sheet of paper (Figure 3.10). Still the strange structure persists, indicating by process of elimination that it is an effect of the grating. This could cause some bias in retrievals made between 455 and 470 nm but will not affect

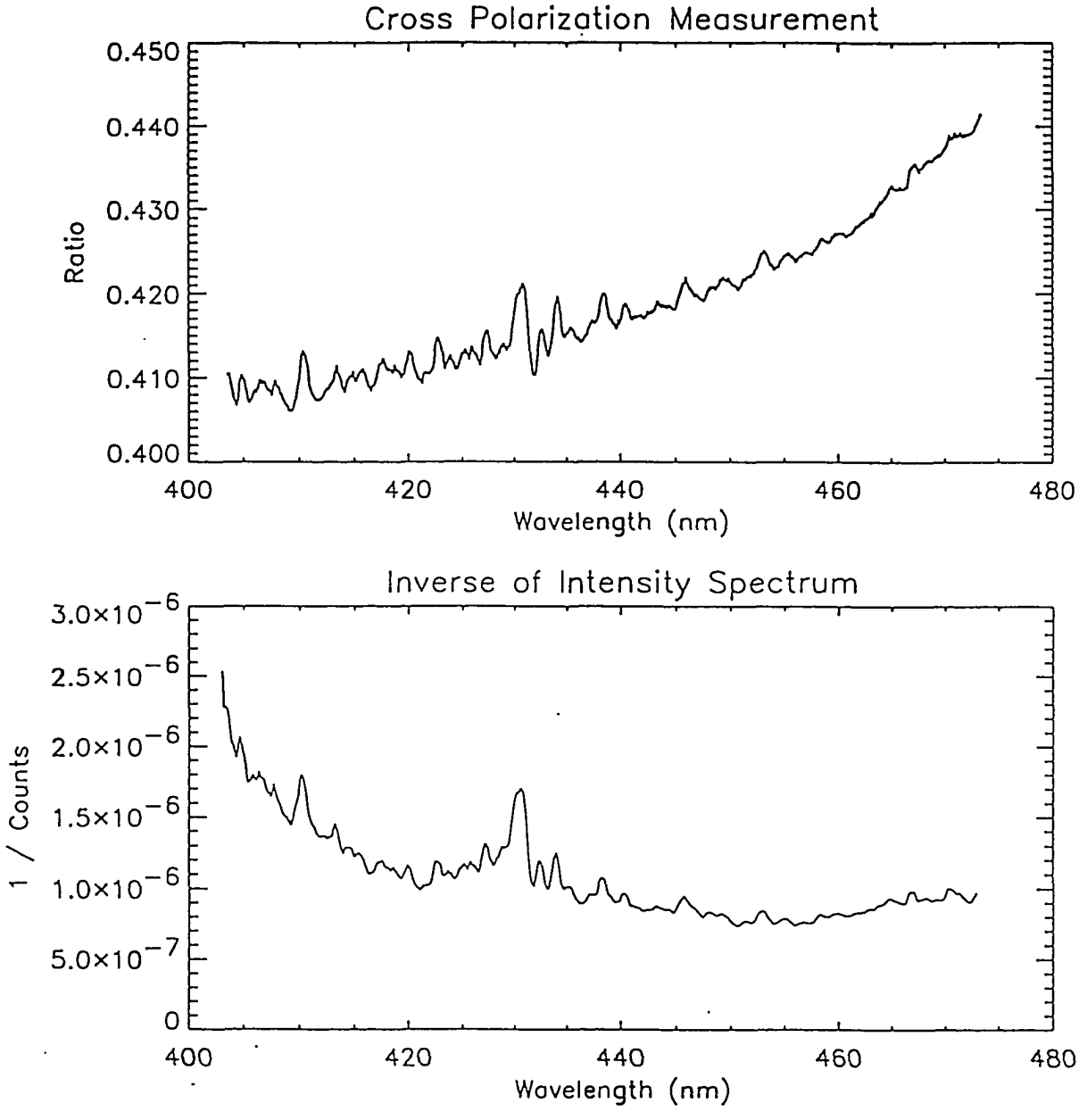

Figure 3.6: Ratio of intensities with spectrograph parallel to the axis to perpendicular to the axis of the sun and the zenith (top). The inverse of a spectrum is also shown (bottom). All measurements were taken on 5/21/92.

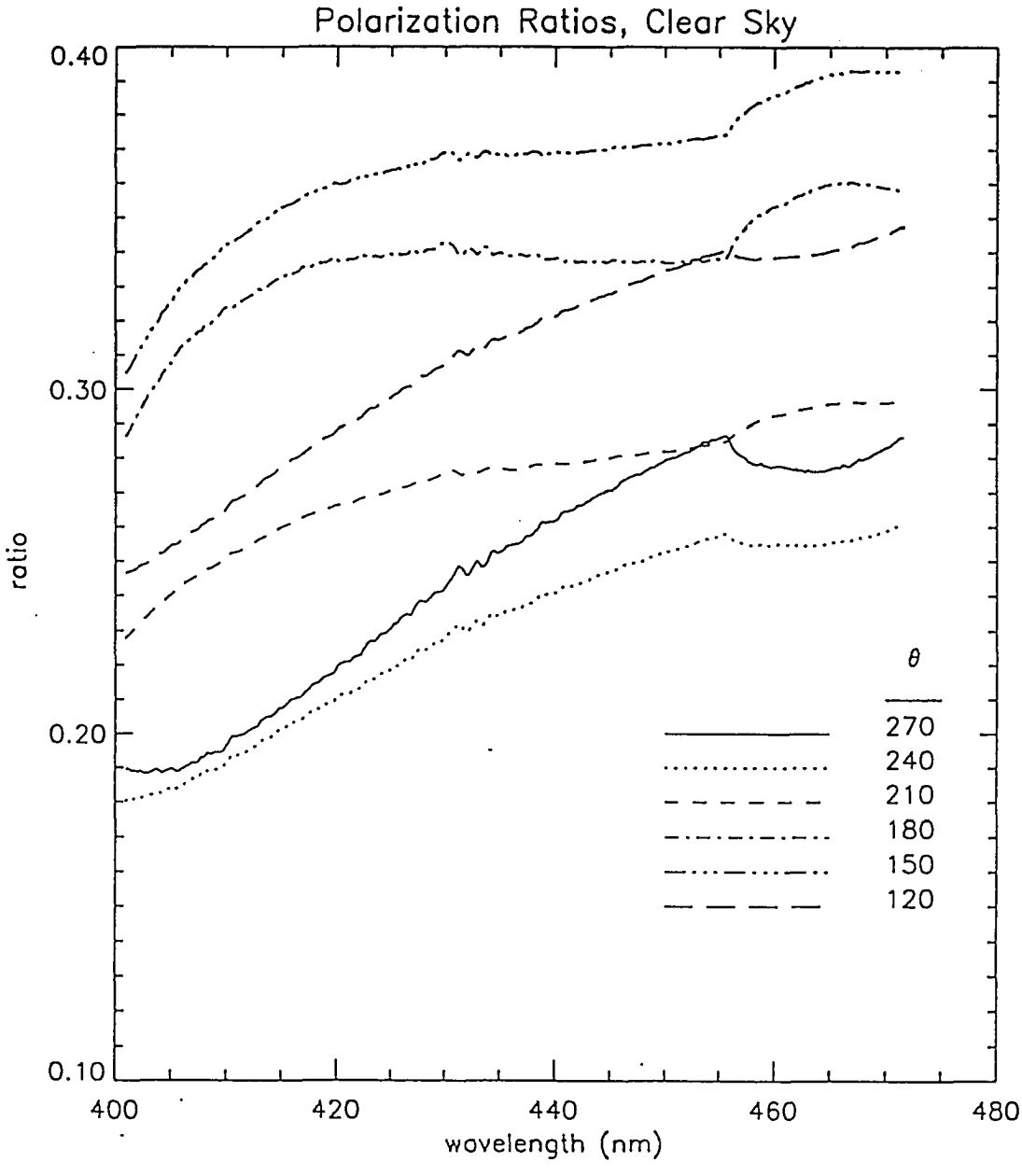

Figure 3.7: Ratio of intensities with polarizer at various angles θ to slit axis to no polarizer. Light source was clear sky.

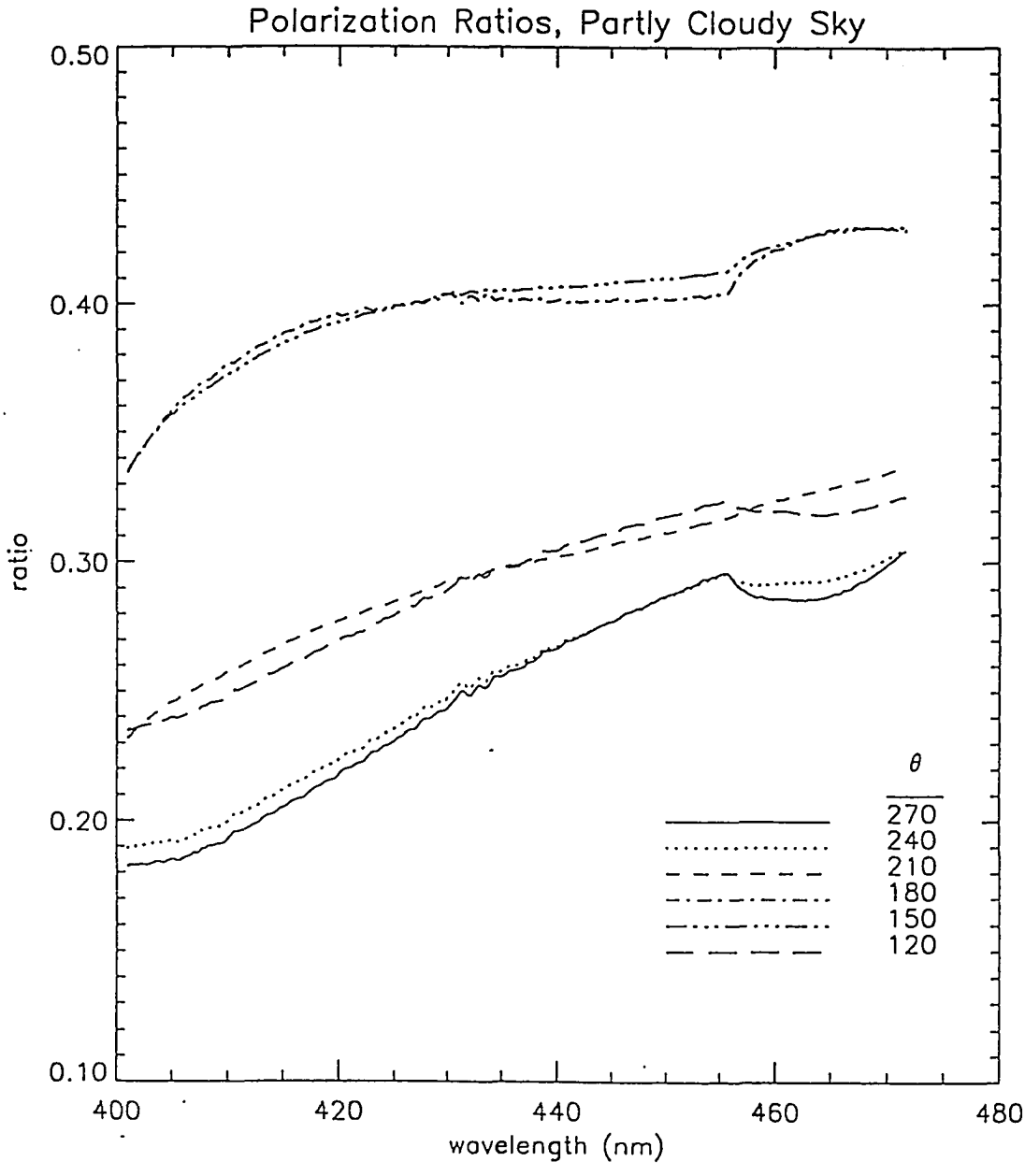

Figure 3.8: Ratio of intensities with polarizer at various angles θ to slit axis to no polarizer. Light source was partly cloudy sky.

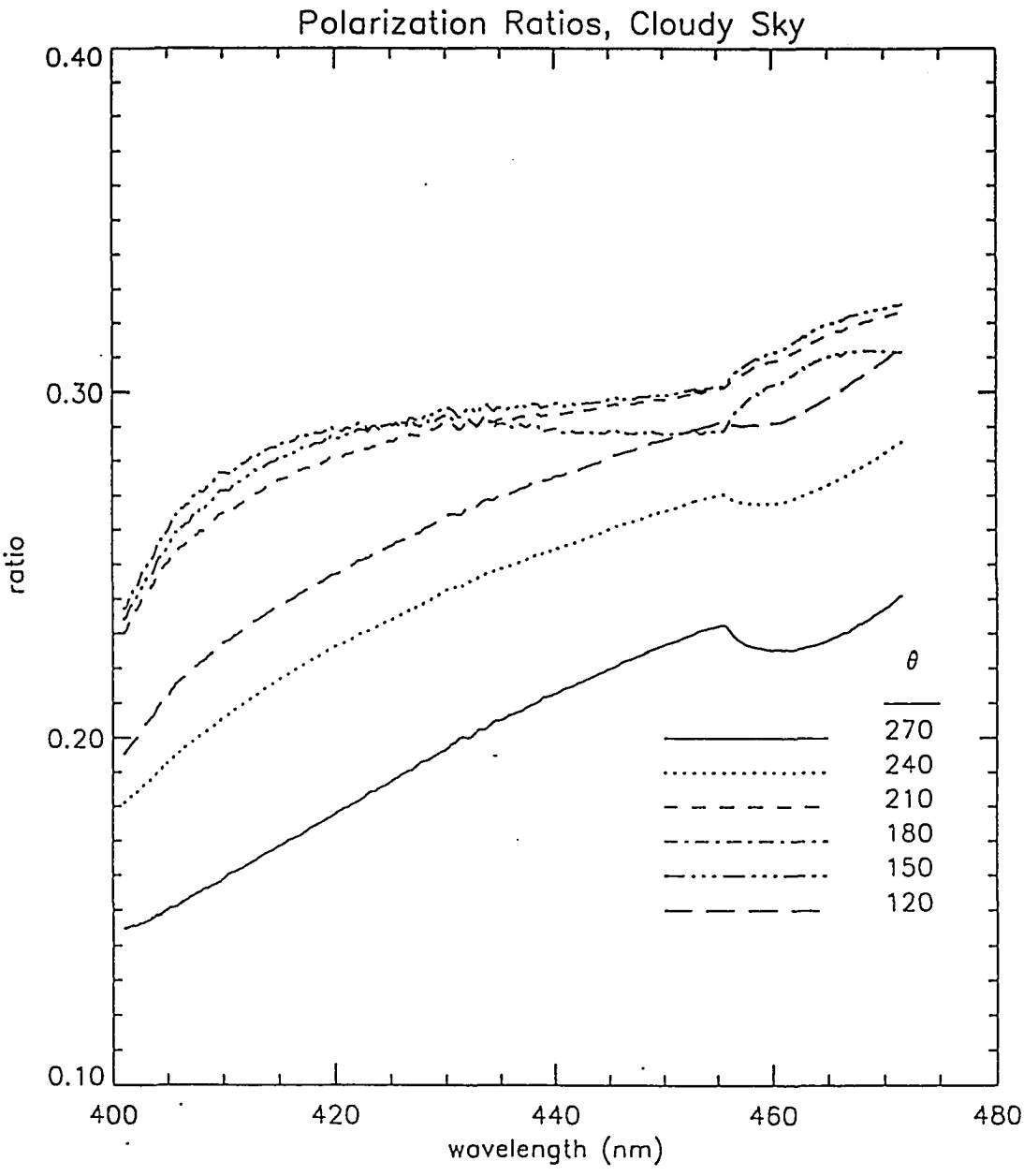

Figure 3.9: Ratio of intensities with polarizer at various angles θ to slit axis to no polarizer. Light source was cloudy sky.

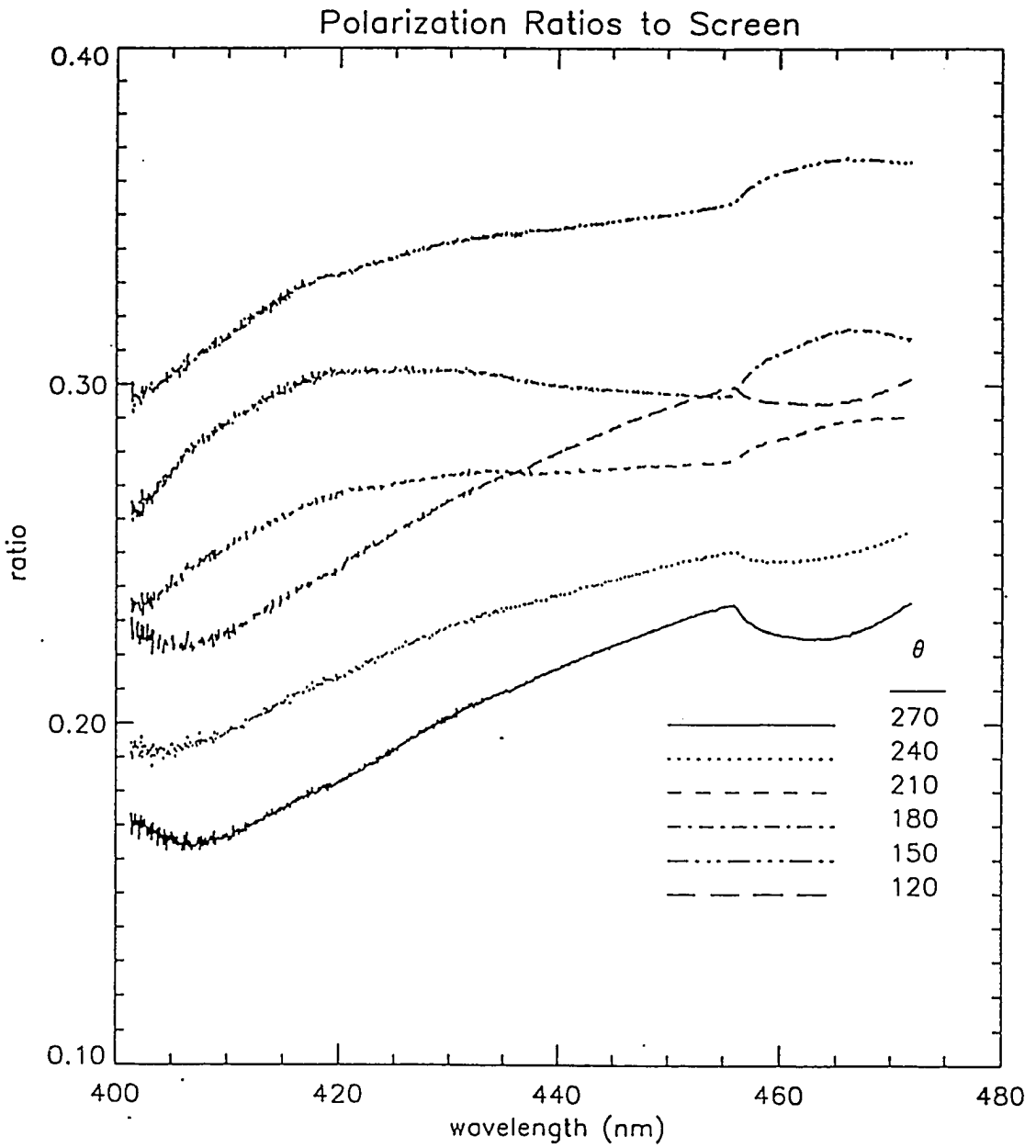

Figure 3.10: Ratio of intensities with polarizer at various angles θ to slit axis to no polarizer. Light source was screen illuminated by lamp.

the NO_2 retrievals in this study.

Since analysis of each observation spectrum yields the actual slant column abundance of various absorbers minus the amount in the control spectrum, the amount of the absorbers in the control must be determined. This requires knowledge of the air mass, δ, which is the ratio of the average optical path due to the absorber of the scattered light reaching the detector to the vertical path (optical depth). *McKenzie and Johnston* [1983] estimated the amount of absorber in the control, Y_c, as

$$Y_c = \left(\frac{Y_{a.m.} + Y_{p.m.}}{2\delta}\right) \sec\theta \qquad (3.25)$$

where δ is the air mass for the twilight measurement and θ is the solar zenith angle at the time the control was measured. It is assumed that the amount of absorber at local noon is the average of the a.m. and p.m. values, $Y_{a.m.}$ and $Y_{p.m.}$, and further, that the air mass at noon can be approximated by $\sec\theta$. Air mass will be more fully developed in Chapter 4. Using the air mass δ for noon is more accurate than $\sec\theta$, especially for the large solar zenith angles at noon during the winter. Table 3.5 shows a comparison of the air mass δ computed and $\sec\theta$ for large solar zenith angles.

Table 3.5: Comparison of air mass factor, δ, with secant of solar zenith angle

zenith angle (θ)	air mass factor δ	secθ
88°	12.3	28.6
86°	9.19	14.3
84°	7.32	9.57
82°	6.04	7.19
80°	5.12	5.76

For the corrections of the NO_2 amount in the control spectrum, an air mass of 16.7 was used for a solar zenith angle of 90°. This was computed with the radiative transfer model by placing the NO_2 uniformly between 25 and 34 km as will be described in Chapter 4. To calculate the air mass at noon, linear interpolation was applied to the air mass values at integer angles once the solar zenith angle of noon was determined. These corrections typically amount to 5 to 25 % of the total amount of the absorber depending on the solar zenith angle of the control. Since NO_2 increases during the day more rapidly from morning to noon than it does from noon to evening, there is an error in the assumption that the noon value is the average of a.m. and yp.m. values. This is conservatively estimated at ± 10 %. Total error in retrieved vertical column amounts due to

absorber in the control is thus estimated to be about 3 % of the total.

As first noted by *Brewer et al.* [1973], the ratio of NO_2/NO changes rapidly near sunset and sunrise making correction necessary. *Solomon and Sanders* [1987] used a simple photochemical model to estimate this correction factor. Using the graph supplied in the paper, this correction leads to an increase in the amount NO_2 at sunset of approximately 16% at evening. This affects the conversion of slant column abundances to vertical column abundance, as will be described in Chapter 4.

The role of tropospheric pollution contributing to the observed NO_2 slant column must be considered. NO_x is produced as a pollution by-product from the high temperature combustion of fossil fuels [*Finlayson-Pitts and Pitts*, 1986]. The spectrograph was located on the eighth floor of the Geophysical Institute, 30 m above a ridge which is 50 m above the Tanana River floodplain. Located about 1.0 km to the east is the University's coal burning power plant. On certain days in the winter, there are extremely high a.m. and (less often) p.m. values of NO_2 the day before or after typically small slant column abundances. Figure 3.11 shows a time series of one such day. The large magnitude of the noon value and the lack of a rapid increase in column abundance at evening twilight strongly suggest

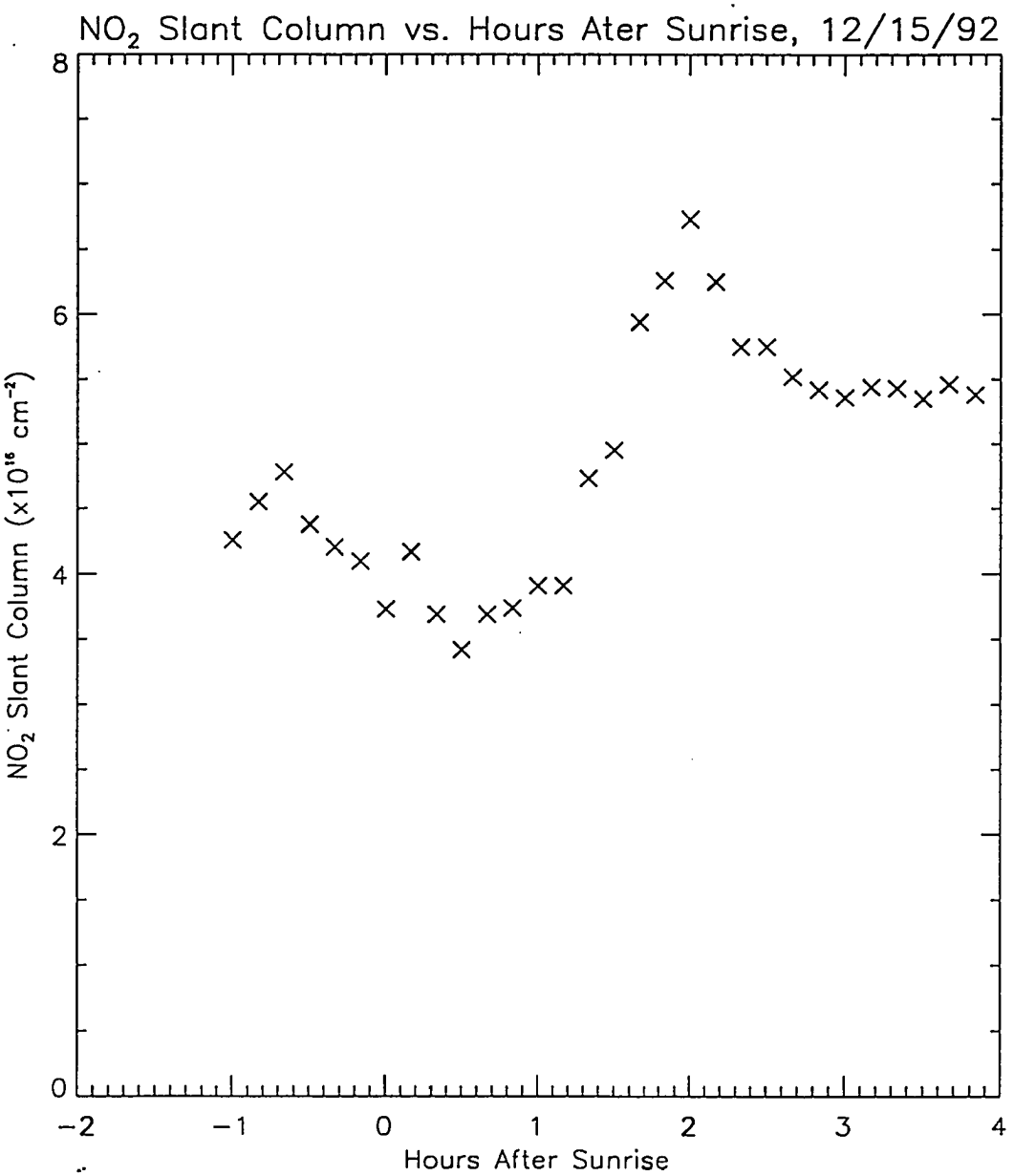

Figure 3.11: NO_2 slant column abundance vs. hours after sunrise for 12/15/92. The magnitude and shape of the time series indicate tropospheric pollution. Sunset is hour 3.33.

non-stratospheric sources of NO_2. Local winter temperature inversions are known to build up to 500 m and trap local pollutants [*Bowling et al.*, 1968]. It is assumed that these very large values are due to tropospheric pollution and are therefore cast out of the general analysis. Assuming an inversion layer of 500 m and an NO_2 mixing ratio of 100 ppbv results in a total column abundance of 13.4×10^{16} cm^{-2} for the polluted days, which is about double the highest values measured by the spectrograph. Thus several days when abnormally large values of NO_2 were recorded are ascribed to local pollution.

The least squares fitting code described in the previous section resulted in a minimum of residuals of the 7 absorbers while varying two additional parameters, the stretch and shift. It is interesting to consider whether the minimum of residuals thus obtained is the global minimum or just a local minimum. One way to approach this problem is to force the stretch and shift values to be far from the final values to see if the method converges. This was investigated for data acquired on April 15, 1993 at 90° solar zenith angle, a "clean" set of data. The initial stretch value was 0.985 (relative to 1.0 which is "unstretched") and the initial offset was 0.00 pixels. The resulting slant column abundances of NO_2, O_3, Rayleigh, and Ring amounts are shown in Table 3.6. The initial values of

stretch and shift were varied as shown in the table and the resulting slant column amounts and final stretch and slip values recorded. The values of stretch and shift do not reconverge exactly, especially if taken too far away from the correct values. This indicates a certain amount of "tuning" is necessary for this algorithm to obtain the global minimum of residuals.

Table 3.6: Sensitivity of algorithm to initial guess of stretch and shift

Initial stretch	Final stretch	Initial shift (pixel)	Final shift (pixel)	derived NO_2 ($x10^{16}$ cm^{-2})	resid-ual
1.000	0.9993	0.	-1.18	4.50	0.04
0.9875	0.9868	0.	0.42	4.57	0.02
0.9700	0.9687	0.	2.81	4.43	0.04
0.9875	0.9894	3.	4.33	3.58	0.38
0.9875	0.9852	-3.	-1.91	4.00	0.17

Another question is how important other absorbers are in relation to the final derived amounts of NO_2. This problem can be attacked by forcing the other absorbers sequentially to zero and observing the new amount of NO_2 derived. Table 3.7 shows the results of forcing other cross

sections besides NO_2 to zero, with the newly derived NO_2 amounts, and the percent difference between the initial and final NO_2 values. It can be seen that NO_2 retrievals are not particularly sensitive to the other absorbers.

Table 3.7: Sensitivity of final derived columns to other absorbers

Absorber set to zero	initial NO_2 ($x10^{16}$ cm^{-2})	final NO_2 ($x10^{16}$ cm^{-2})	percent difference
ozone	4.57	4.60	0.7
Rayleigh	4.57	4.64	1.5
Ring	4.57	4.60	0.7
O_4	4.57	4.69	2.6

The conversion of slant column to vertical column abundance is next considered. As will be discussed in Chapter 4, errors in this conversion are twofold. First, there is the uncertainty of the air mass calculations due to model input and numerics. The multiple scattering model used to derive these factors has been tested thoroughly and found to be accurate [*Stamnes et al.*, 1988]. The results of

air mass calculation will depend to some extent on the model atmosphere used, but *Perliski and Solomon* [1993] have shown that these effects are less that 5%. Second is the uncertainty in vertical distribution of NO_2 which changes the air mass for a given solar zenith angle. Assuming an initial Gaussian profile of NO_2 centered at 27.5 km of full-width half-maximum of 14 km, errors in air mass are estimated to be ± 10% for a shift in the center of the profile by ± 5 km. Changing the width of the profile by ± 4 km results in an air mass error of ± 2% [*Krehler et al.*, 1994].

Assigning a time and a zenith angle to each measurement must be taken into account. The timing for each measurement was taken off the computer clock. The computer clock was observed to drift approximately 1 minute per month, and was reset when the error reached more than one minute. This combines to an uncertainty of ± 0.7 minutes for the time assigned to a particular measurement. During this period of time, the solar zenith angle at 90° changes from a range of 0.04° on December 21 to 0.07 ° on March 21. This results in a change in air mass of approximately 0.7 % to 1.2 % on the two extreme dates. Thus timing uncertainties lead to an error in retrieved vertical column amounts of about the same percentage.

The random error of the measurement can be estimated by

the magnitude of the residual term from Eq. 3.6 for M wavelengths. This error is [*Nash*, 1979]

$$err = \frac{1}{M}\sqrt{\frac{\sum_{m}^{M} e_m^2}{\sum_{m}^{M} k_m^2}} \tag{3.26}$$

where e_m are the individual residuals from Eq. 3.6, k_m is the error in the cross section, and N is the number of wavelengths used in analysis. However, the errors are not random as the examination of a series of residual spectra will reveal. It is more useful to characterize the *reproducibility* or the ability to retrieve the same amount of NO_2 under identical conditions. Figure 3.12 shows such a set of measurements taken every 5 minutes on March 1, 1993 for a period of three hours around local noon. The standard deviation of these measurements is 0.1 x 10^{16} cm^{-2} an which is an indication of how precise or reproducible the measurement is under the same sky and absorber conditions. Bias errors are more difficult to quantify. *P. Johnston* [private communication, 1994] suggests a bias error of ± 0.3 x 10^{16} cm^{-2}, arising from grating polarization, Ring Effect, and the use of room temperature NO_2 absorption cross sections.

To get overall error estimates one may assume that the individual sources of error are random which allows taking

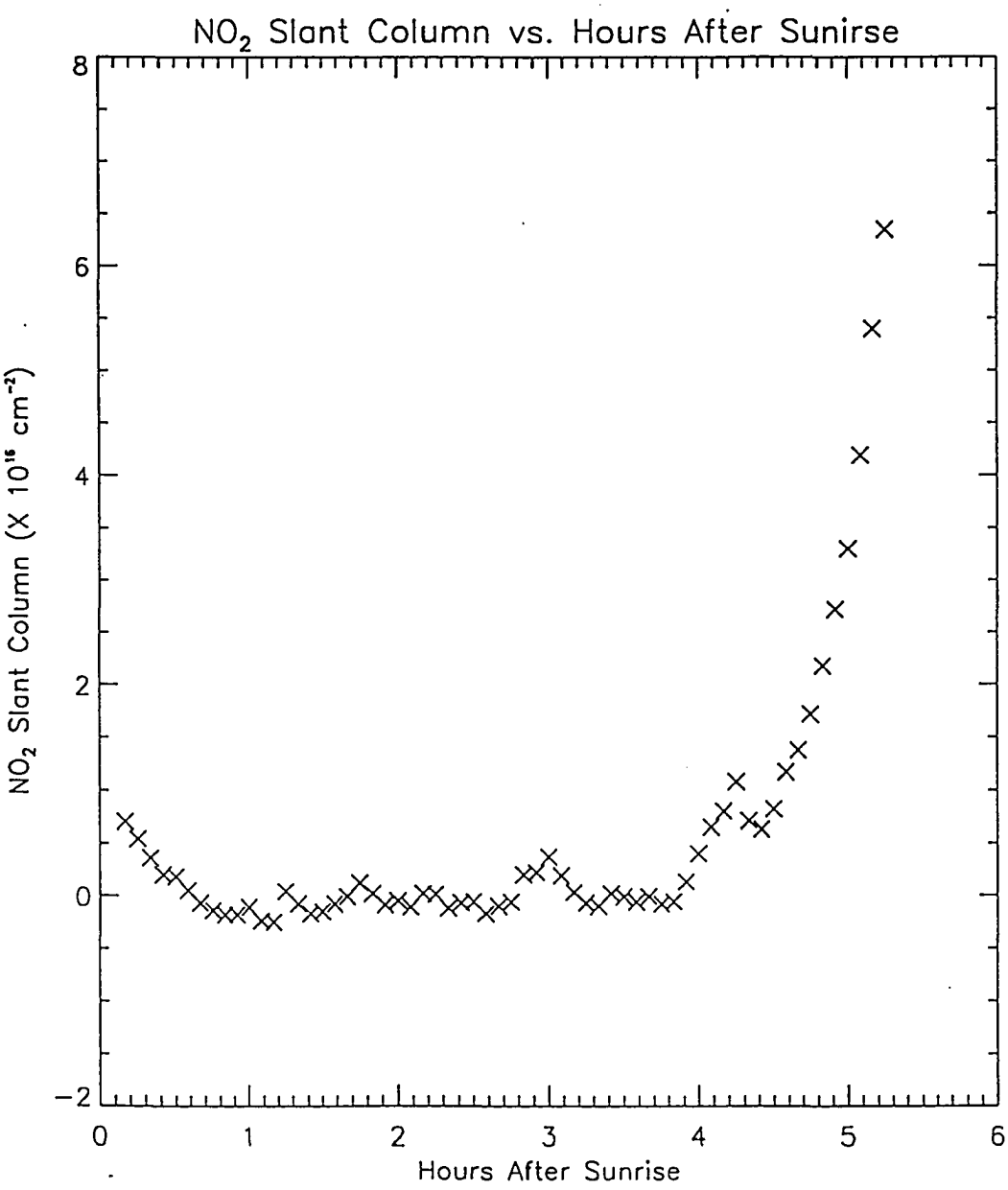

Figure 3.12: NO_2 slant column abundance vs. hours after sunrise for 3/1/93. The standard deviation for hour 1.00 through hour 3.50 was 0.14 x 10^{16} cm^{-2}. Sunset was at hour 5.00. Measurement at hour 2.42 was used for the control.

the root mean square of the individual errors. This yields an overall estimated absolute error in vertical column abundance of NO_2 of 14%, dominated by the uncertainty in air mass and cross sections. For slant column abundances the error is 10%, due mostly to by the uncertainty in the NO_2 cross sections. If one were interested in only the relative values of the slant columns, for instance in taking (a.m./p.m.) ratios, the errors would be an estimated 5%, with the largest source of error the NO_2 in the control spectrum. To reduce the errors in these retrievals would require accurate knowledge of the NO_2 vertical distribution, the use of temperature dependent NO_2 absorption cross section, and a more accurate determination of the amount of NO_2 in the control spectrum.

3.3: Lauder Intercomparsion

From May 10 to May 25, 1992, New Zealand's National Institute of Water and Atmosphere (NIWA), formerly the Department of Scientific and Industrial Research (DSIR), hosted the NO_2 UV-Visible Spectrometer Instrument Intercomparsion organized by the Network for the Detection of Stratospheric Change (NSDC). Groups from seven countries formally participated in this event with their ground based spectrographs and spectrometers designed to measure slant column NO_2. The University of Alaska (UAF) group was an informal participant to the intercomparison, which meant that this group took data simultaneously with the other groups but did not officially submit the data to referee Dr. David Hofmann of the Climate Monitoring and Diagnostic Laboratory in Boulder, Colorado. The intercomparison was blind-blind, so that no group had knowledge of the measurements of other groups. There was, however, free exchange of information regarding hardware setup and software routines to reduce the data. UAF took data every 10 minutes throughout daylight hours. A comparison is made of the two daily 90° solar zenith angle slant column measurements derived from UAF and NIWA data. Table 3.8 shows the results of morning measurements and Table 3.9 the

evening measurements of UAF compared with those of NIWA.

The UAF measurements were reduced to slant column abundances using the reduction least squares algorithm supplied by NIWA described above in section 3.1.2. The time of 90° solar zenith angle was computed and the slant column at 90° calculated by linear interpolation of the two measurements closest to 90°. The p.m. values are closer to the NIWA values, with an average difference of 8.7%, in contrast with the a.m. values, with an average difference of 29.1%. One possible reason for the larger a.m. errors is that in the morning the UAF detector cooler had just been turned on. Although the temperature control feedback circuitry had locked on, that is, the electronic temperature control circuitry was closed, the detector's temperature was not as well stabilized as it was by the evening. The control spectrum used for each day was taken on the relatively clear day 138 (May 17). NIWA used 12:06 NZST for I_o and the UAF group used 12:32 NZST.

NIWA had the only detector which used a single element photomultiplier; the other systems used photodiode arrays. Thus the NIWA system scanned the grating continuously and was therefore subject to transients caused by the passage of clouds across the spectrometer's field of view. The NIWA

Table 3.8: Results of Lauder Intercomparison a.m. Measurements

Day Number	UAF NO_2 slant $x10^{16}$ (cm^{-2})	NIWA NO_2 slant $x\ 10^{16}$ (cm^{-2})	% difference
133	2.67	2.05	+30.2
134	2.50	2.42	+3.3
135	3.46	2.53	+36.8
136	3.33	2.45	+35.9
138	--	--	--
139	2.24	2.07	+8.2
141	2.02	1.71	+18.1
142	2.37	1.77	+33.9
143	2.19	1.73	+26.6
144	1.70	1.04	+63.4

Table 3.9: Results of Lauder Intercomparison p.m. Measurements

Day Number	UAF NO_2 slant $x\ 10^{16}$	NIWA NO_2 slant $x\ 10^{16}$	% difference
133	3.72	3.99	-7.2
134	4.15	4.33	-4.3
135	4.46	4.57	-2.5
136	3.66	4.34	-15.7
138	3.66	4.39	-16.7
139	3.81	3.90	-2.3
141	3.88	3.63	+6.9
142	2.97	3.49	-14.9
143	2.71	2.67	+1.5
144	2.51	2.97	-15.5

group analyzed the spectral region from 430 to 470 nm while the UAF system analyzed the smaller region from 435-450 nm. One advantage in using the larger wavelength region is that the absorption structure of O_3 is most prominent between 450 and 470 nm and is thus easier to quantify.

Chapter 4

Air Mass Computations

4.1: Introduction

Spectroscopic measurements of scattered light to determine the slant column abundance of trace gases such as NO_2, OClO, and BrO make use of long optical paths through the atmosphere to maximize the absorption. *Brewer et al.* [1973], *Noxon et al.* [1979], *Harrison* [1979], *McKenzie and Johnston* [1982], *Mount et al.* [1987] and *Pommereau and Goutail* [1988] used visible light spectrometers to measure the differential absorption of NO_2. *Solomon et al.* [1988], and *Schiller et al.* [1990] extended the technique to measure OClO and BrO. Unlike the direct solar beam, which, in the absence of refraction, travels along a straight optical path to arrive at a detector, scattered light travels along a zig-zag or "random walk" path before reaching the detector. Conversion of slant column abundances to vertical column abundances, a quantity which may be inferred with photochemical models, requires dividing the slant column abundance by a dimensionless factor which represents the *average* slant optical path due to the absorber relative to the vertical path (optical depth). This quantity is known as the optical enhancement factor or more commonly the air

mass.

Computation of air masses requires a rather complete knowledge of the optical properties of the atmosphere including cross sections for absorption and scattering as well as profiles of radiatively active atmospheric constituents from which the optical depth, single scattering albedo, and phase function of each layer may be determined. Spherical geometry must be considered for the large solar zenith angles used, as must the effects of multiple scattering. The effects of refraction and surface albedo are insignificant in the case of stratospheric absorbers [*Perliski and Solomon*, 1993] and will be neglected in the computations that follow. Air mass is also required to retrieve vertical profiles from a time series of slant column abundances derived from scattered light measurements [*McKenzie et al.*, 1991].

4.2 Direct light transmission

Definition of air mass

All of the following arguments apply to monochromatic light; later the discussion will be expanded to include the effects due to different wavelengths. The optical depth $d\tau$ of an infinitesimal absorbing layer dz (cm) is given by

$$d\tau = -\sigma\, n\, dz\,. \tag{4.1}$$

The total optical depth across a layer of thickness Δz is

$$\tau = \sigma \int_{\Delta z} n(z)\, dz = \sigma N \tag{4.2}$$

where σ (cm^2) is the absorption cross section, n (cm^{-3}) is the absorber concentration, Δz (cm) is the thickness of the layer, and N (cm^{-2}) is the vertical column abundance of the absorber. The air mass, δ, for a particular absorber is defined as the ratio of the slant optical path, τ_s, to the vertical optical depth, τ, both due to that absorber

$$\delta = \frac{\tau_s}{\tau} = \frac{\tau_s}{\sigma N} \tag{4.3}$$

or

$$\delta = \frac{N_s}{N} \ . \tag{4.4}$$

Note the *optical depth* denoted by τ implies a vertical path while *optical path* is denoted by τ_s and implies a *slant path*. For direct solar radiation, the intensity of the beam passing through the atmosphere is given by the extinction law commonly known as Beer's Law

$$I = I_o e^{-\tau_{atm}} e^{-\tau_s} \ . \tag{4.5}$$

where I_o is the extraterrestrial solar irradiance, τ_{atm} is the optical path excluding the absorbing species of

interest, and τ_s is the optical path of that particular species.

For the direct beam through a plane parallel atmosphere, the air mass is simply

$$\delta = 1/\mu_o \ . \tag{4.6}$$

where $\mu_o = \cos\theta$ and θ is the solar zenith angle. This is illustrated in Figure 4.1. Thus, for overhead sun $\delta = 1$. For a curved atmosphere, the optical path for the direct beam is somewhat more complicated, but can still be computed from geometrical considerations.

Operational Definition of Air Mass in terms of Measured Intensities

Assume that there is a detector on the ground that measures the direct solar irradiance, I, for a particular solar zenith angle in the presence of an absorber with column abundance, N (cm^{-2}). Next, assume one could repeat the measurement in the absence of that absorber to obtain the resulting direct solar irradiance I'. Using Eq. 4.5 twice, taking the ratio, and then using Eq. 4.3 to solve for δ yields

$$\delta = -\frac{\ln(\frac{I}{I'})}{\sigma N} \ . \tag{4.7}$$

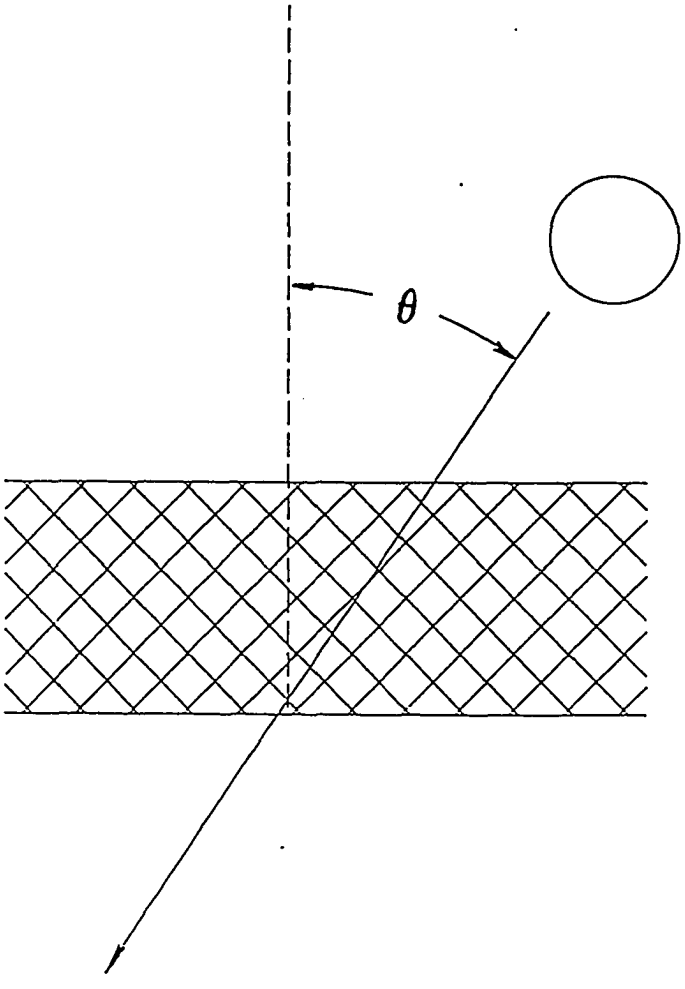

Figure 4.1: For the direct beam through an absorbing layer, the airmass is $1/\mu_o$. μ_o is the cosine of the solar zenith angle, θ.

Of course, in nature one cannot arbitrarily remove a gas from the atmosphere for the purpose of measuring its air mass using Eq. 4.7. The practical significance of this equation is that it can be used to *compute* the air mass by making one computation of the direct beam in which the absorbing gas is included and another in which it is absent.

4.3 Air Mass for Single and Multiple Scattering

Single Scattering

For scattered light measurements, it is typical for the detector to accept light from a small solid angle about the zenith direction. To compute the air mass for an atmosphere which includes single scattering, the approach is much the same as for the direct beam. However, singly scattered light follows many different optical paths through the absorbing layer on its way to the detector, so an average air mass δ^{avg} for singly scattered light is defined as

$$\delta^{avg} = \frac{\tau_{avg}}{\tau} = \frac{\tau_{avg}}{\sigma N} \tag{4.8}$$

where τ_{avg} is the average optical path due to the absorber of all the scattered light reaching the detector. This is illustrated in Figure 4.2 which shows singly scattered

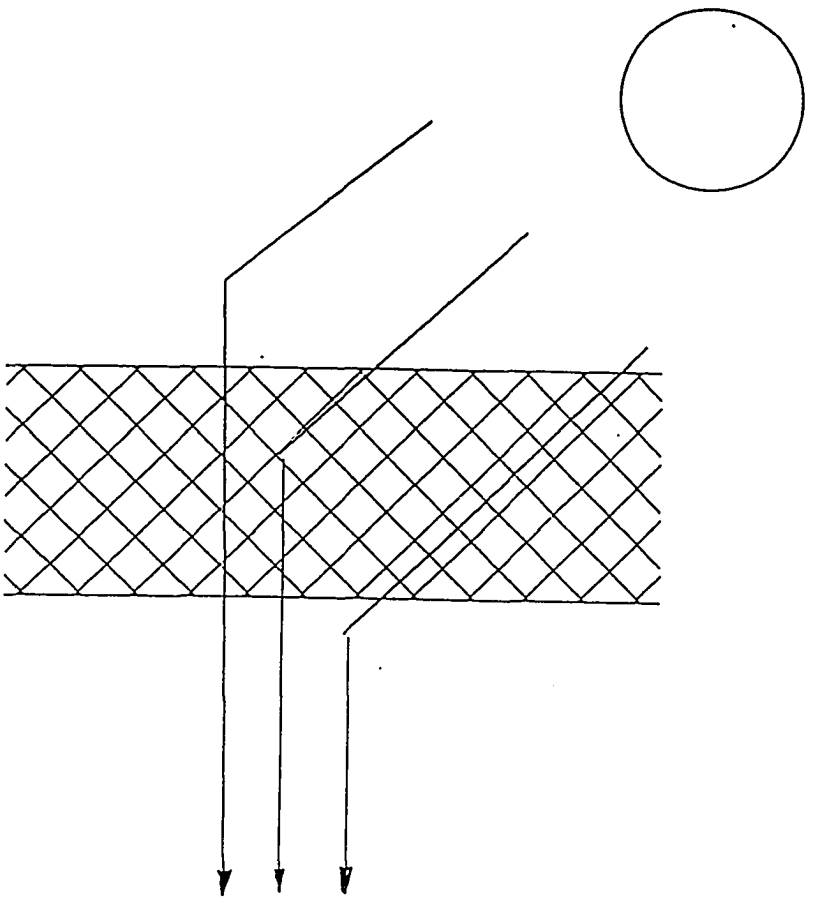

Figure 4.2: For single scattered light there are many different optical paths through the absorbing layer. Assuming for simplicity that there are only three as shown resulting in τ_1, τ_2 an τ_3, τ_{avg} may be calculated.

radiation along three optical paths reaching the detector. Assuming for simplicity that photons traveling along each of these paths is equally likely to reach the detector, τ_{avg} is the average of the three τ's. One can express the average air mass, δ^{avg}, in terms of the zenith sky intensity at the ground with the absorbing layer in place, using an equation identical to Eq. 4.3 except that τ_{avg} replaces τ_s

$$I = I_o e^{-\tau_{atm}} e^{-\tau_{avg}} . \tag{4.9}$$

Eq. 4.8 provides an operational definition of the average optical path of the absorber (which consists of a combination of slant path and vertical path as indicated in Figure 4.2) in terms of a measurable quantity. It also expresses how the scattered intensity is reduced in response to the average optical path due to the absorber. Next, express the zenith intensity without the absorber likewise and solve for δ^{avg} use Eq. 4.9 twice, take the ratio, and use Eq. 4.8 to obtain the average air mass

$$\delta^{avg} = -\frac{\ln(\frac{I}{I'})}{\sigma N} . \tag{4.10}$$

Note again that the practical consequence of Eq. 4.10 is that it can be used to *compute* air mass, although it was defined through a "thought" experiment.

Multiple scattering

Air mass factors may be defined for multiply scattered light through an absorbing layer in much the same way as for singly scattered light. Figure 4.3 illustrates the situation with three optical paths through the absorber resulting in photons reaching the detector. Assume for simplicity that τ_{avg} is the average of the three optical paths due to the absorbing layer. Some of the light reaching the detector may have been scattered more than once within the absorbing layer. One may think of "straightening out" the zig-zag path to get an overall pathlength $\Delta\tau$ through the layer and an optical path τ using Eq. 4.1. Multiple scattering within an absorbing layer results in a larger overall τ_{avg} than for single scattering.

The average air mass, δ^{avg}, may again be defined by Eq. 4.8 where again τ_{avg} is the average optical path due to the absorbing layer of all the light (singly and multiply scattered) reaching the detector; that is use Eq. 4.8 as an operational definition of air mass based on the "thought" experiment and proceed. Again, compute the zenith intensities with and without the absorber and solve for the air mass δ^{avg} using Eq. 4.10. The effects of multiple scattering will be minor except in the troposphere (where the atmosphere is dense) and at large solar zenith angles.

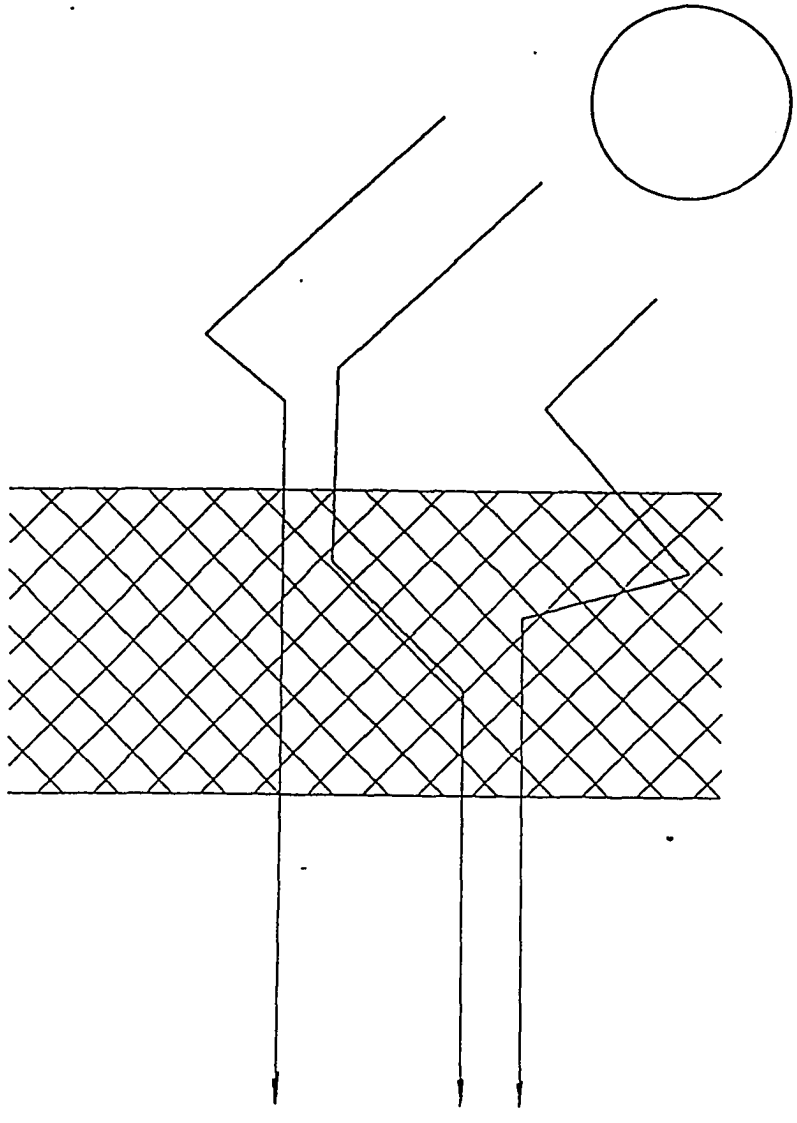

Figure 4.3: For multiply scattered light there are certain photons reaching the detector that have been scattered more than once within the absorbing layer. One can "straighten out" the zig-zag path and use Eq. 4.1 to yield τ_1, τ_2, and τ_3. τ_{avg} may be determined as before.

4.4: Results of Air Mass Computations

Corrections for a curved Atmosphere

To compute air mass, the *Stamnes et al.* [1988] discrete ordinate radiative transfer code which has been modified to include the curvature of the atmosphere [*Dahlback and Stamnes*, 1991] was used. Inclusion of spherical geometry is done in an approximate manner using a geometrical correction to treat the direct beam so that the basic equation to be solved is

$$u \frac{\partial I(r,u)}{\partial r} + \frac{1-u^2}{r} \frac{\partial I}{\partial u} = -k(r) \; [I - S] \; . \qquad (4.11)$$

with

$$S(r,u) = \frac{a(r)}{2} \int_{-1}^{1} p(r,u,u') \, I(r,u') \, du' + \frac{a(r)}{4\pi} p(r,u,\mu_o) \, F_s \exp[-\tau \, Ch(r,\mu_o)] \qquad (4.12)$$

where I is the azimuthally averaged intensity, u is the cosine of the polar angle, μ_o is the cosine of the solar zenith angle, r is the radial distance from the center of the earth, S is the source function, k is the extinction coefficient, a is the single scattering albedo, F_s is the irradiance at the top of the atmosphere (normal to the beam), p is the scattering phase function, τ is the optical depth, and Ch is the air mass, generally referred to as the Chapman function [*Dahlback and Stamnes*, 1991]. In the

pseudo-spherical approximation, the second term on the left hand side of Eq. 4.11 is ignored. The resulting equation is similar to the plane-parallel equation, except that the direct beam attenuation includes the effect of spherical geometry. For our purposes, this approximation yields accurate results as discussed in some detail by *Dahlback and Stamnes* [1991]. The atmosphere is divided into a suitable number of layers to adequately resolve the optical properties. An exponential-linear-in optical depth approximation is used to compute the direct beam source within each layer [*Kylling and Stamnes*, 1992]. With these modifications, zenith intensities can be computed including all orders of scattering.

Clear sky air masses

Air masses were computed from zenith intensities using Eq. 4.10. An NO_2 layer 5.0 km thick and with a column abundance of 3.0×10^{15} cm^{-2} was placed sequentially every 5.0 km starting from 0 and ending at 45 km. The nine values of air masses with the absorber at various levels were determined as a function of solar zenith angle ranging from 70° to 95°. A 69 layer Subarctic Winter atmosphere was used and the wavelength taken to be 440 nm. The results of these computations are shown in Figure 4.4. It can be seen that, in general, the higher the absorbing layer is placed, the

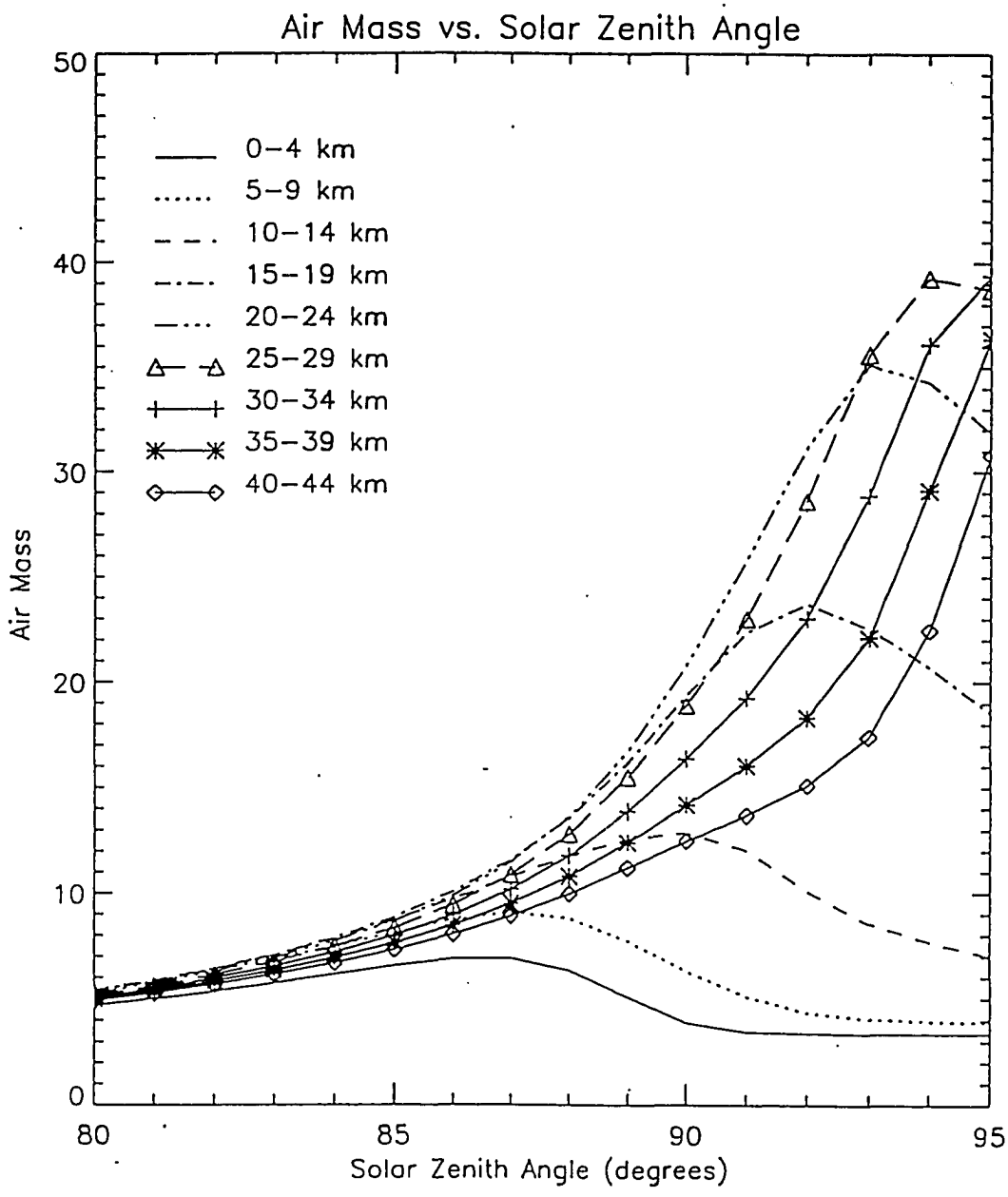

Figure 4.4: Air mass values computed using Eq. 4.10 at 440 nm for absorber placed in 5 km layers. The effect of interconversion between NO and NO_2 was ignored.

larger the maximum of the air mass. Further, the higher the absorbing layer, the larger the solar zenith angle at which the maximum air mass occurs. It will be seen in Chapter 5 that air masses can be used to determine the vertical profile of the absorber from a time series of slant column abundance measurements.

Effect of aerosols

Stratospheric aerosols are known to change the scattering geometry of the twilight radiation field [*Volz and Goody*, 1962; *Shaw*, 1981]. A layer of optical thickness of only 0.01 alters the radiance and radiance gradient by one order of magnitude. A series of computations were performed to estimate aerosol effects on retrieved NO_2 slant column abundances and air masses. To simulate the volcanic stratospheric sulfate aerosol layer, a scattering layer was introduced into the model atmosphere between 19 and 20 km. A single scattering albedo of 0.99 and an asymmetry factor of 0.8 were chosen, corresponding to an aerosol that is a sulfuric acid and water mixture [*Pinto et al.*, 1989].

To estimate the effect of this aerosol layer on slant column abundances retrieved from spectral measurements, a synthetic spectrum of zenith intensities was constructed by the radiative transfer model at wavelengths from 432 to 469 nm. The solar zenith angles were 30° and 90°; the 30°

spectrum served as the "control" and the 90° as the "measurement". The aerosol optical depth was varied from 0.00 to 0.10. These computations were made in 0.1 nm increments and the results interpolated to a wavelength spacing of 0.069 nm to simulate the spectral measurements. The NO_2 profile input to the model was a Gaussian concentration profile of 12 km full-width half-maximum centered at 20 km with total column abundance of 3.0×10^{15} cm^{-2}. These synthetic spectra were analyzed by the NO_2 analysis code to retrieve slant column abundances. A plot of the aerosol optical depth vs. retrieved NO_2 amounts is shown in Figure 4.5 (top).

As a check on the consistency of these computations, the vertical column abundance was computed for the clear sky retrieval. This was accomplished by adding the NO_2 slant column amount in the 30° control to the 90° slant column retrieved as in Eq. 3.1, and dividing the sum by the air mass appropriate for this profile. The air mass for this profile was computed using Eq. 4.10. The resulting vertical column of 2.94×10^{15} cm^{-2} is 2% smaller than the amount of NO_2 input to the model. This small difference indicates the retrieval algorithm is robust and that the multiple scattering computations provide inputs for the retrievals and air mass values that are consistent. This exercise serves to strengthen confidence in the entire analysis

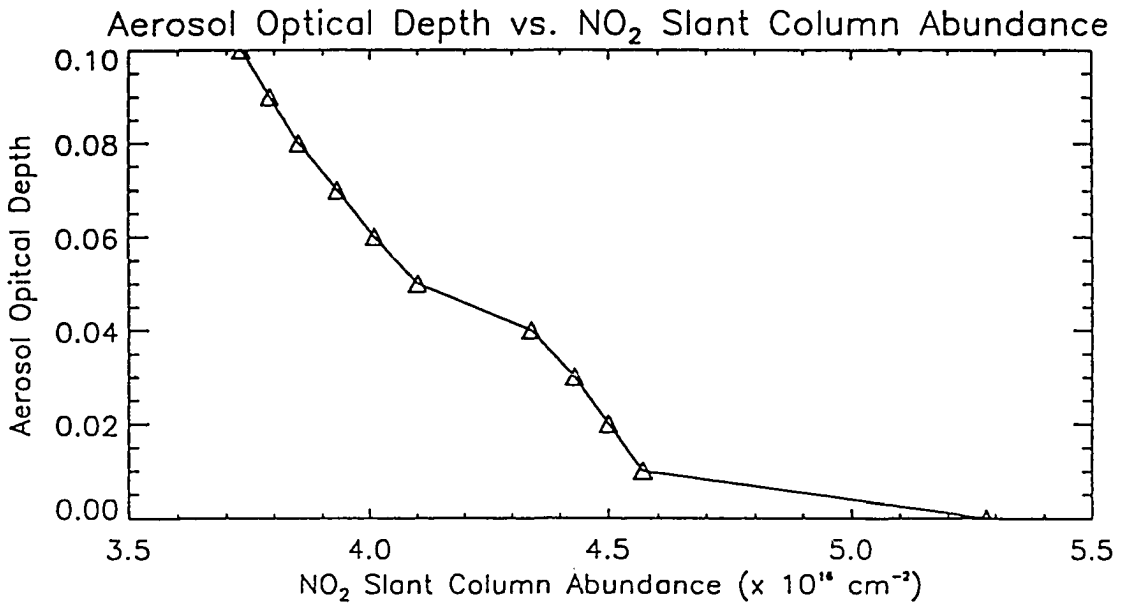

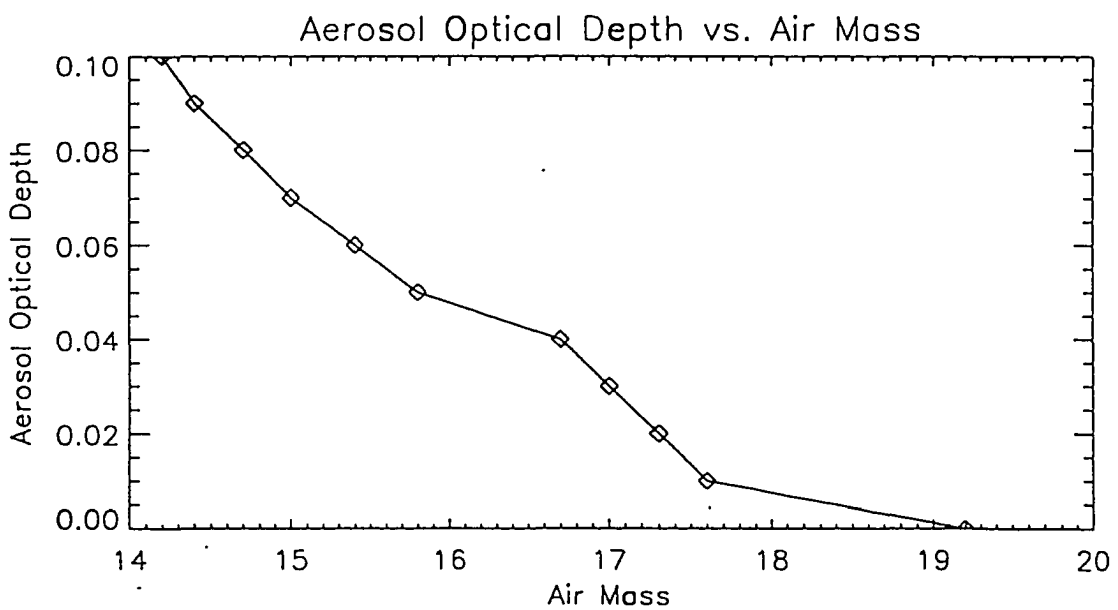

Figure 4.5: Effect of varying the optical depth of an aerosol layer placed between 19 and 20 km on retrieved NO_2 slant column abundance (top) and on air mass (bottom). In the first case the radiative transfer model generated synthetic spectra which were analyzed using the NO_2 data retrieval code. In the second case the model computed the air mass.

package, including the NIWA retrieval algorithm, as well as the multiple scattering computations used to determine air mass values.

The effect of aerosols on air mass was investigated by varying the aerosol optical depth from 0.00 to 0.1 and determining air mass at a solar zenith angle of 90° using Eq. 4.10. The NO_2 profile input to the model was the same Gaussian centered at 20 km as above. The results are shown in Figure 4.5 (bottom).

These calculations show the strong sensitivity of the NO_2 retrievals to stratospheric aerosols located at the same altitude as the peak of the NO_2 profile. A modest stratospheric aerosol optical depth of $\tau = 0.02$ results in an underestimation of the NO_2 slant column abundance of 15%. However, if this slant column is converted to a vertical column by dividing by the air mass computed with the aerosol layer, the underestimation of the vertical column is only 6%. Thus, it is important to use the air mass computed with the appropriate aerosol profile.

It is more typical that the peak of the NO_2 concentration is above the aerosol layer. To test the impact of an aerosol layer beneath the peak concentration, air mass values were calculated using the same NO_2 Gaussian profile as above centered at 25 km. Except for an initial 5% reduction of the air mass for an optical depth of 0.01

compared with the clear sky, air mass values are fairly insensitive to further increases in optical depth of the aerosol layer. Next, the NO_2 profile was moved to a lower altitude so the maximum was centered at 15 km. The results are plotted in Figure 4.6 showing the strong dependence of air mass on aerosol optical depth. It can be concluded that air mass is most sensitive to the stratospheric aerosols when the bulk of the absorber is at the same height or lower than the aerosol layer.

4.5: Comparison of Air Mass Computations: Monte Carlo Versus Discrete Ordinate Radiative Transfer Techniques

Air Mass Computations

Air mass may be calculated in at least two different ways. One method [*Perliski*, 1992] determines the air mass δ by computing zenith intensities at the ground level and using Eq. 4.9. The second method pursued here is a weighting scheme that is justified as follows.

The atmosphere is divided into L adjacent layers. Figure 4.7 shows the geometry of the method. Consider single scattering only. Radiation that has been scattered only once within layer i and emerges at the lower boundary of layer i from the zenith direction, is denoted by I_i. Before entering the detector, these photons follow a vertical path and are attenuated by a factor $exp(-\tau_{iL})$ where

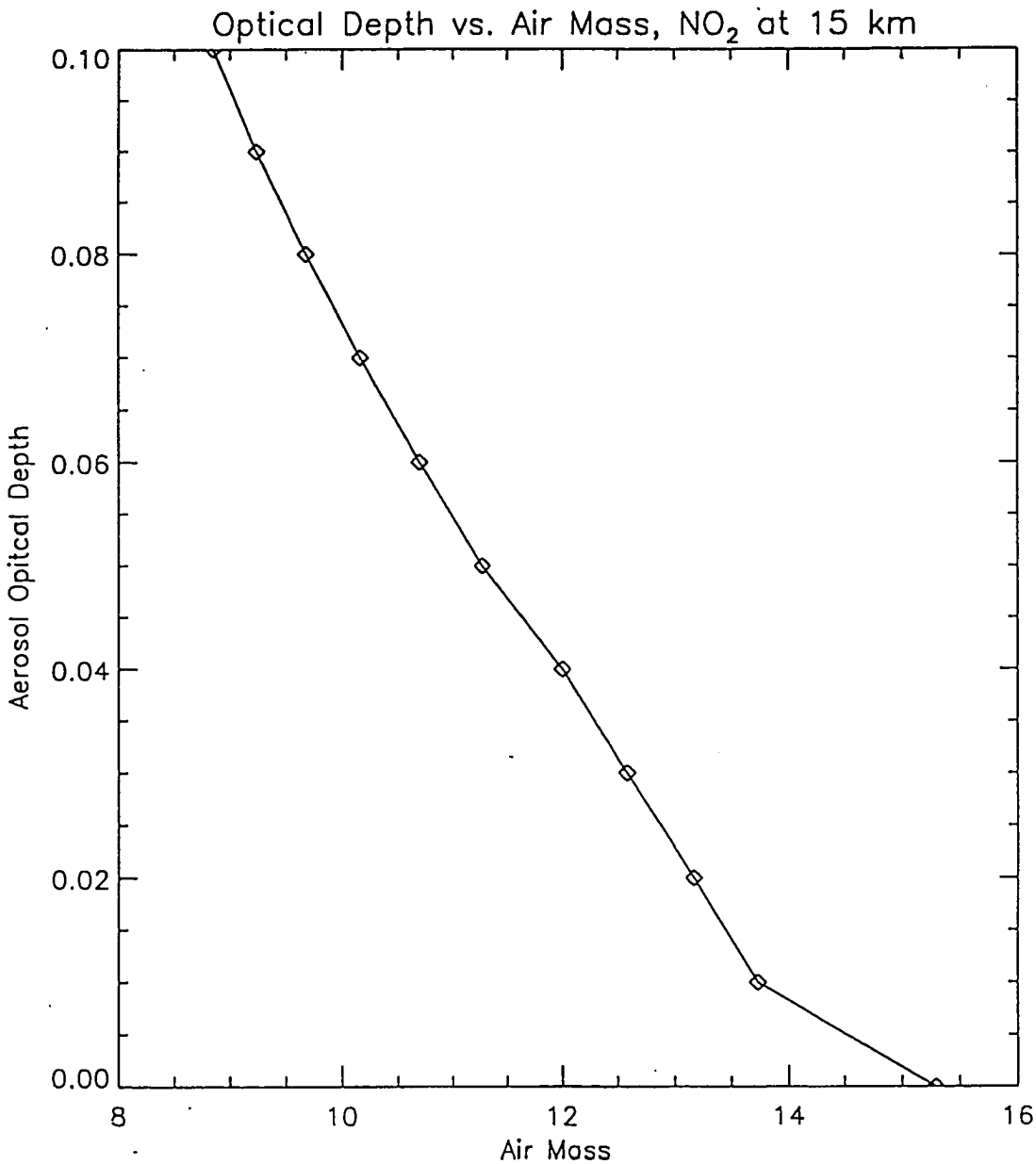

Figure 4.6: The effect of lowering the NO_2 profile on air mass sensitivity to aerosols. The optical depth of the aerosol layer between 19 and 20 km was varied as in Figure 4.5. The NO_2 profile was centered at 15 km.

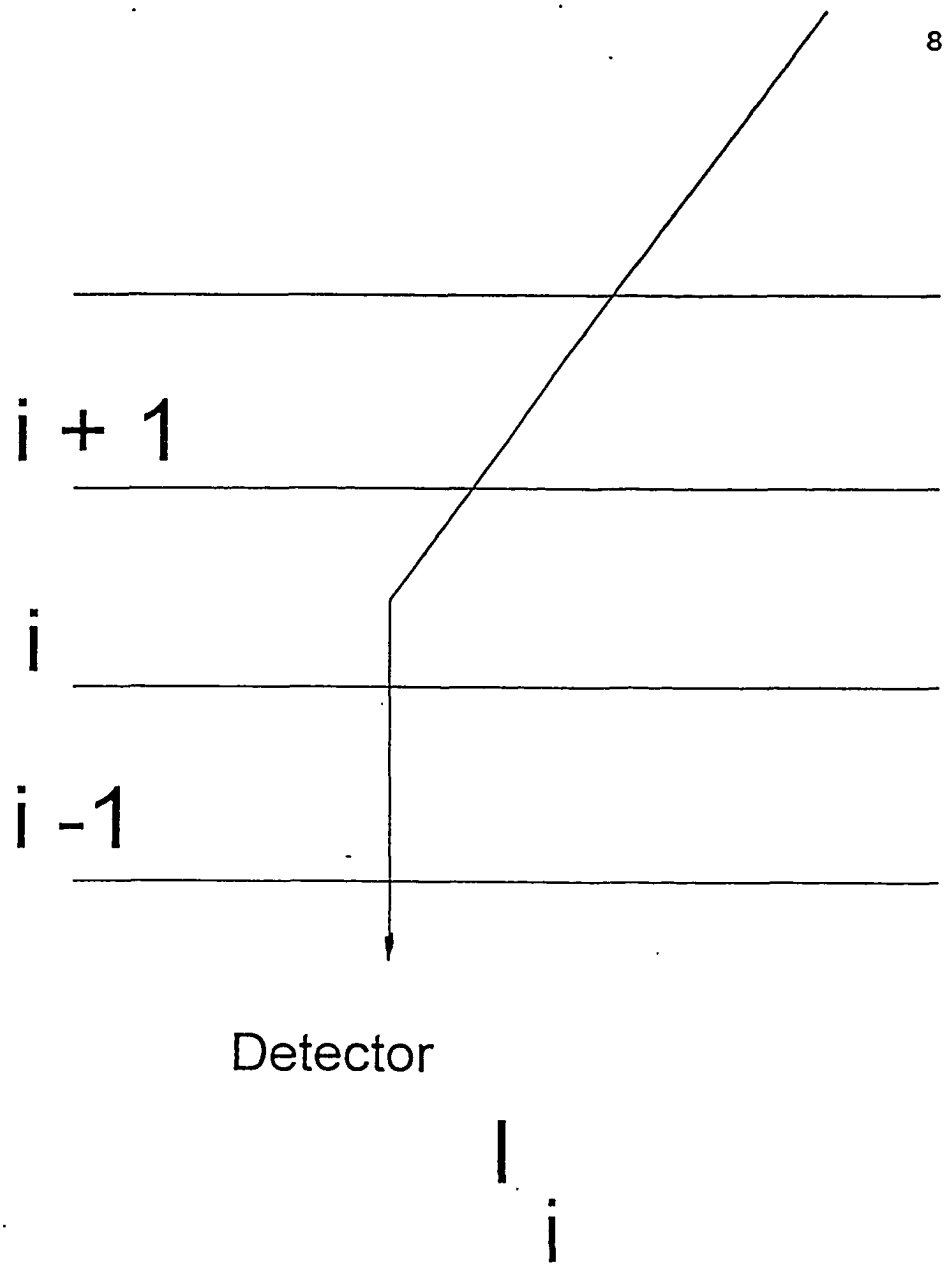

Figure 4.7: The geometry of the weighting method. The radiance that has been scatterd only one within layer i from the zenith direction is denoted I_i. The photons scattered within layer i are attenuated by exp $(-\tau_{iL})$, where τ_{iL} is the vertical optical depth of the different scattering levels within layer i and the ground.

τ_{iL} is the vertical optical depth from the center of layer i to the detector at the ground. τ_{iL} represents the average optical depth between the different scattering levels within layer i and the ground.

The total radiance of singly scattered radiation in the zenith direction at the ground, i.e., the contribution from all layers, is

$$I_{total} = \sum_{i=1}^{L} I_i \ . \tag{4.13}$$

The probability that the singly scattered radiation received by the detector arises from scattering within layer i can be described by the probability density function P_i

$$P_i = \frac{I_i e^{-\tau_{iL}}}{\sum_{i=1}^{L} I_i \ e^{-\tau_{iL}}} \ . \tag{4.14}$$

The absorber total optical path of the constituent studied (here NO_2) along the slant path (before it is scattered) plus the vertical path (which has been followed by the photons that arise from the scattering within layer i) is denoted by τ_i^{abs}. The effective absorber optical path (slant plus vertical) is obtained by weighting the absorber optical paths, τ_i^{abs}, with the probability density function P_i

$$\tau_{eff}^{abs} = \sum_{i=1}^{L} P_i \, \tau_i^{abs} \; . \qquad (4.15)$$

The air mass is obtained by taking the ratio of the effective absorber optical path, τ_{eff}^{abs}, and the absorber optical depth, τ^{abs} (the absorber optical path in the vertical column from the top of the atmosphere to the ground). To account for multiple scattering, I_i, appearing in the probability function, P_i, is calculated for multiple scattering. With this procedure, only attenuation between the center of the layer i and the ground is accounted for. Note that in this methodology, once a photon is scattered within the absorbing layer, it is constrained to travel straight down to the detector without the possibility of being scattered again.

Radiative Transfer Models

The Stamnes model has already been described. The Backwards Monte Carlo method works as follows. The propagation of light through an absorbing optically thin scattering spherical shell atmosphere is modeled by first allowing light to emerge in a given direction from a hypothetical detector. The directions and optical distances between each subsequent scattering event are then simulated as a random walk process, with the probability of a scattering event occurring at a particular location being

proportional to the local scattering coefficient. The direction the light takes after a scattering event is selected randomly by consideration of either the Rayleigh or Mie scattering phase function, depending on whether the scattering event was selected to be molecular or aerosol scattering. At each scattering location, the direct flux is computed and weighted by the appropriate phase function.

Absorption is computed along each scattering path and along the direct solar beam path. The combination of the direct beam and the scattered radiation reaching the detector along a particular path constitutes an "intensity history." In general, on the order of a thousand intensity histories are computed and averaged for each solar zenith angle considered, resulting in a zenith intensity for each integral "final scattering" altitude. The backwards Monte Carlo technique used in this study is described in more detail by *Perliski* [1992] and is conceptually similar to that described by *Collins et al.* [1972], *Adams and Kattawar* [1978]; *Kattawar and Adams* [1978] and *Lenoble and Chen* [1992].

Comparison of Air Mass Calculations

In the tests that follow, these three methods were used:

DISORT I: Discrete ordinate method using Eq. 4.10, by

computing ratios of zenith intensities.

DISORT II: Discrete ordinate method using the weighting scheme described by Eqns. 4.13 - 4.15.

MONTE CARLO: The Monte Carlo statistical method using Eq. 4.10, by computing ratios of zenith intensities.

The following tests were designed to compare the three methods for consistency and time of computation. Air mass was computed for two absorber heights at two wavelengths. In the first case, a layer 5.0 km thick of total column abundance 3.0×10^{15} cm^{-2} was placed between 20 and 25 km. In the second, the same layer was placed between 0 and 5 km. Air mass was computed at solar zenith angles from 70° to 95° in 1° increments at two wavelengths, λ = 450 and 650 nm. The same atmospheric profile of 75 layers, each 1 km thick, was used as input to each of the three models; the surface albedo was set to 0.3.

Figure 4.8 shows air mass versus solar zenith angles for λ = 450 nm and 650 nm for the three methodologies with the absorber between 0 and 5 km and 20 and 25 km. Figure 4.8 (a) shows the case for a stratospheric absorber at 450 nm. The agreement is within 6.0% at a solar zenith angle of 90°. Figure 4.8 (b) shows air mass versus solar zenith

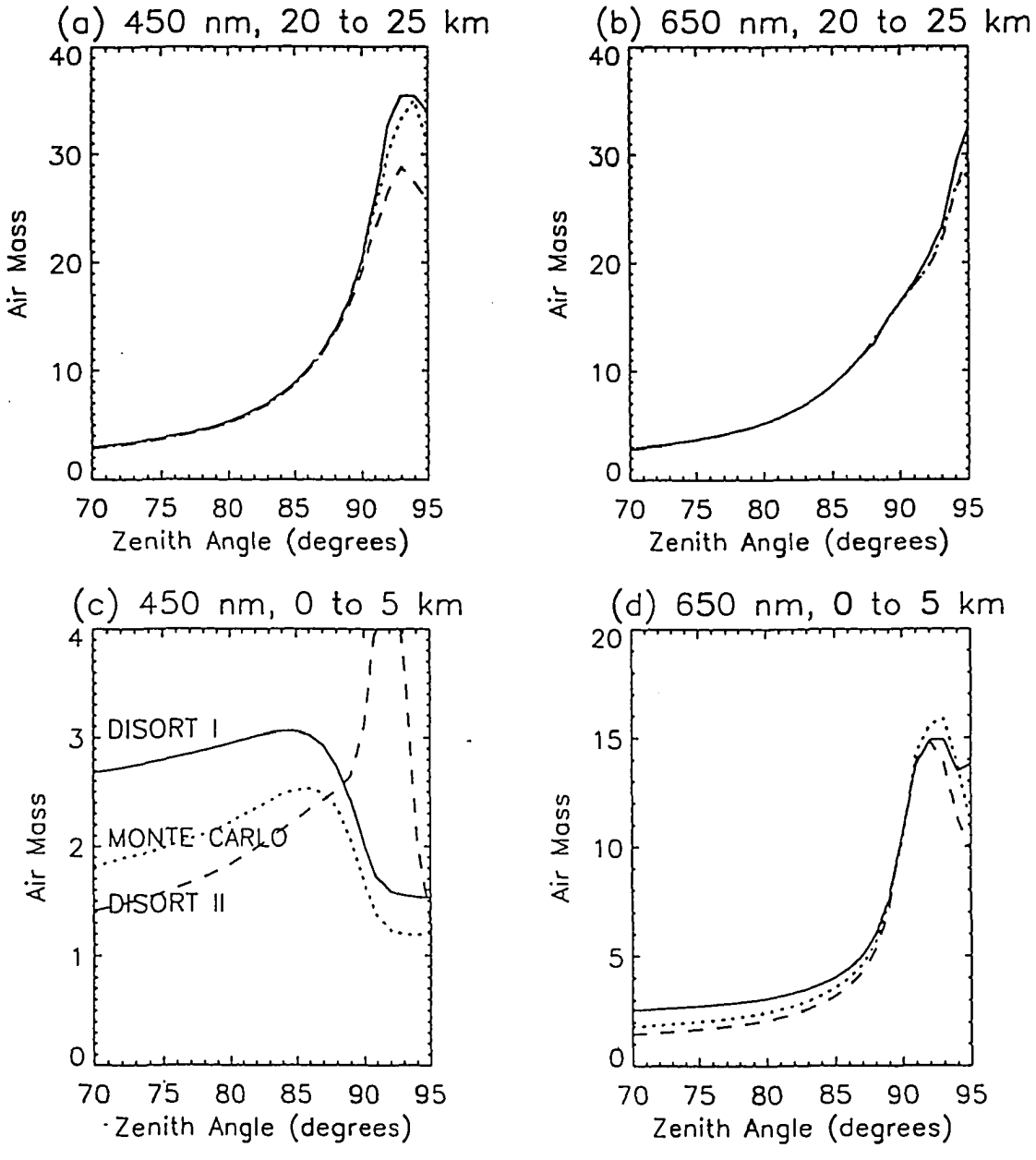

Figure 4.8: Air mass computed with three different methods: DISORT I (solid), Monte Carlo II (dotted), and DISORT II (dashed). Calculations were with the absorber between 20 and 25 km at 450 nm (a) and 650 nm (b). The absorber was between 0 and 5 km at 450 nm (c) and 650 nm (d).

angles for λ = 650 with the absorber between 20 and 25 km. Again, the agreement is good, differing by 5.5% at 90°. Thus, when the bulk of NO_2 is in the stratosphere, as is always the case in the absence of tropospheric NO_2 pollution, all three methods are in satisfactory agreement.

The agreement at 90° solar zenith angle is not as good when the absorber is located in the troposphere as is shown in Figure 4.8 (c) at 450 nm where the difference is 21% and Figure 4.8 (d) at 650 nm where the difference is 4%. To investigate the reasons for the poor agreement, several tests were conducted.

It is the direct beam that drives the scattering at each layer, so this quantity was compared at each layer for a solar zenith angle of 60°. The optical properties of each of the 75 layers (Rayleigh optical depth, absorption optical depth) were determined from the model atmosphere by the DISORT driver and inserted directly into each of the radiative codes. Figure 4.9 shows the percentage difference between the DISORT I and the Monte Carlo direct beams (dotted line), and the DISORT I and DISORT II direct beams (solid line) at each layer of the atmosphere. The agreement of the direct beam is to within 5% at the bottom of the atmosphere for all three models. All three models attenuate the beam using Beer's Law so the disagreement must be due to different path geometries since identical optical inputs are

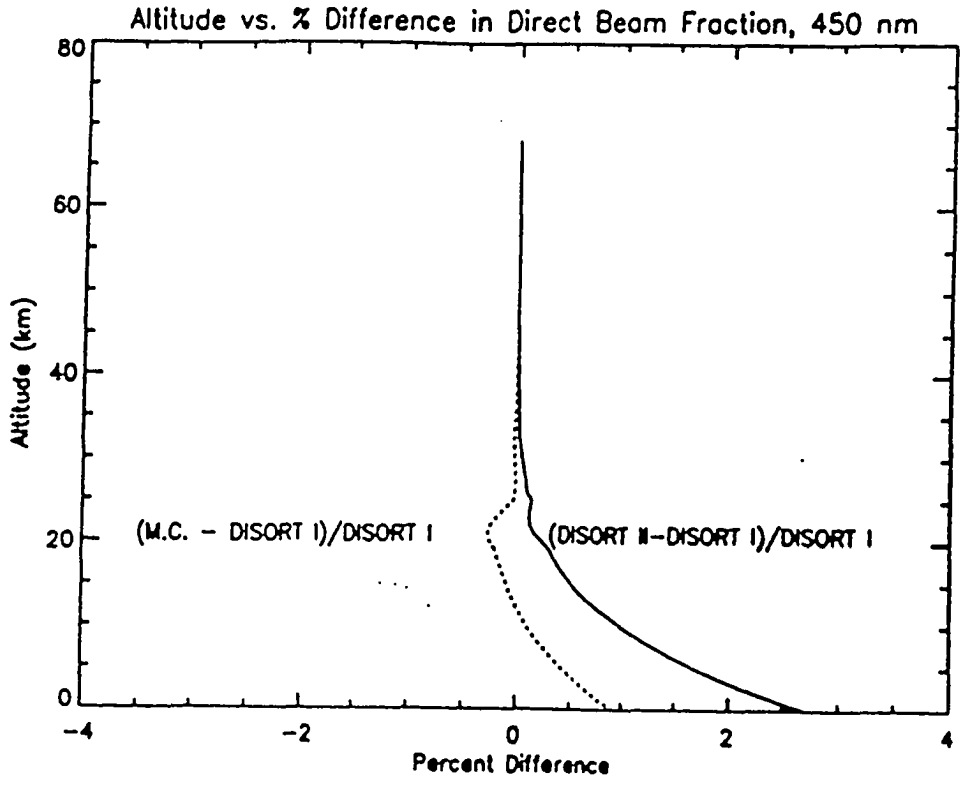

Figure 4.9: Comparison of the direct beam in each layer of the model atmosphere for a solar zenith angle of 60°. The percentage difference between Monte Carlo and DISORT I (dotted) and DISORT I and DISORT II (solid) are shown.

used.

Next, the effect of the phase function on the intensities and air mass was checked. Using DISORT I, zenith intensities with and without the NO_2 absorbing layer were computed for isotropic and Rayleigh scattering. The results of these computations are shown in Table 4.1 for the tropospheric absorber and Table 4.2 for the stratospheric absorber. Although the intensities are consistently larger for isotropic than for Rayleigh scattering, the ratios of intensities with and without the absorber are virtually the same. The air masses for isotropic and Rayleigh scattering agree to within 4% for tropospheric and stratospheric absorbers.

The agreement among the models for the zenith intensities with NO_2 and without NO_2, shown in Table 4.3 (tropospheric absorber) and Table 4.4 (stratospheric absorber), is not as good as for the direct beam. Note the close agreement between isotropic intensities from DISORT I (Table 4.1 and 4.2) and the intensities from the Monte Carlo method (Tables 4.3 and 4.4). It is tempting to conclude that the Monte Carlo method is using isotropic rather than Rayleigh scattering. Note the very close agreement in the

Table 4.1: Comparison of intensities using different phase functions: tropospheric absorber

Phase Function	wavelength (nm)	intensity ($W/m^2/nm$)	air mass factor
Rayleigh	450 NO_2	0.001922	2.01
	w/o	0.001928	
isotropic	450 NO_2	0.002379	1.92
	w/o	0.002386	
Rayleigh	650 NO_2	0.001011	10.53
	w/o	0.001012	
isotropic	650 NO_2	0.001318	10.48
	w/o	0.001319	

Table 4.2: Comparison of intensities using different phase functions: stratospheric absorber

Phase Function	wavelength (nm)	intensity ($W/m^2/nm$)	air mass factor
Rayleigh	450 NO_2	0.001870	20.32
	w/o	0.001927	
isotropic	450 NO_2	0.002315	20.24
	w/o	0.002386	
Rayleigh	650 NO_2	0.001011	16.41
	w/o	0.001012	
isotropic	650 NO_2	0.001318	16.39
	w/o	0.001319	

ratio of zenith intensities with and without absorber, (I'/I). This is consistent with the finding above, that the ratio is insensitive to the type of scattering utilized. In spite of the close agreement in these ratios, when the natural log of the ratio is taken, as is done in the computation of the air mass for the DISORT I and the Monte Carlo methods, minute differences are magnified. This is because for small x, ln(1-x) is close to -x. For instance, at 450 nm with a tropospheric absorber (the worst agreement among the four cases), the DISORT I and Monte Carlo ratios differ by only 0.05%, yet the log ratios (and hence the air mass values) differ by 21%.

The weighting method (used in DISORT II) gives good agreement with the other two models for a stratospheric absorber where multiple scattering is minimal, but poorer agreement for a tropospheric absorber where multiple scattering is significant. As mentioned, the weighting method (used in DISORT II) does not allow photons to scatter again once they have scattered in the absorbing layer which could be the source of this method's disagreement with the other two models. When the weighting method (DISORT II) and DISORT I method both use single scattering only, the air mass results are much closer than when both are run using multiple scattering, thus giving further evidence that

multiple scattering below the absorbing layer is the reason these two methods give different results.

Table 4.3. Comparison of Zenith Intensities with Tropospheric Absorber with and without NO_2

λ (nm)	DISORT I x 10^3 ($w/m^2/nm$)	Ratio	Monte Carlo I x 10^{-3} ($w/m^2/nm$)	Ratio
450 NO_2	1.922	.99698	2.365	.99761
w/o	1.928	--	2.370	--
650 NO_2	1.011	.99943	1.263	.99945
w/o	1.012	--	1.263	--

Table 4.4: Comparison of Zenith Intensities with Stratospheric Absorber with and without NO_2

λ nm	DISORT I x 10^{-3} ($w/m^2/nm$)	ratio	Monte Carlo I x 10^{-3} ($w/m^2/nm$)	ratio
450 NO_2	1.870	.9699	2.300	.9704
w/o	1.928	--	2.370	--
650 NO_2	1.011	.9993	1.268	.9991
w/o	1.022	--	1.270	--

Conclusions

Air masses have been computed by three different methodologies. The agreement among these three methods is to within 6% at 90° solar zenith angles at 450 and 650 nm

when the absorber is in the stratosphere. Thus, the conversion of 90° solar zenith angle slant column abundances to vertical column abundances using these air masses will agree to within 6% for a stratospheric absorber. Larger differences in air mass occur when the absorber is in the troposphere where multiple scattering becomes significant. Because the optical enhancement for tropospheric absorbers at large zenith angles is small, the ratio of intensities with and without absorbers is very close to 1. Any numerical noise is amplified leading to significant differences in air masses.

Practically speaking, these differences in tropospheric air masses are not important to the community of stratospheric spectroscopists interested in measuring NO_2, BrO, or OClO column abundances because there is normally so little of these gases in the troposphere. The differences in tropospheric air masses will not greatly affect the air masses for NO_2 whose major fraction of total column is above 20 km. However if one were to calculate air mass for a tropospheric absorber or if there were significant tropospheric pollution, serious differences would ensue when computing air mass values by these methods. Air masses computed using the weighting method (used in the DISORT II method) show the biggest disagreements with the other two methods for a tropospheric absorber. This is probably

because this formulation fails to fully treat multiple scattering.

Both DISORT I and II require less computing time than the Backwards Monte Carlo method. Significant savings of computing time result from using the Discrete Ordinate method without loss of accuracy over the backwards Monte Carlo method. A DEC-5000 workstation running ULTRIX for the Discrete Ordinate method took about 60s of CPU time for 26 solar zenith angles at one particular wavelength. This compares with execution times of about 2500s for similar computations using the Monte Carlo technique running on a Cray MP.

Chapter 5

Vertical Profile Retrieval

5.1 Introduction

The conversion of slant column abundance to vertical column abundance requires dividing by the air mass, a quantity which varies with the vertical distribution of the absorber. Tropospheric air masses are about ten times smaller than those in the stratosphere. Thus, in order to accurately convert slant column abundances to vertical column abundances, one needs to know the absorber profile. Inference of the vertical distribution of a trace gas in the stratosphere from ground-based measurements of scattered light originated with the Umkehr ozone measurements carried out by *Götz et al.* [1934] at Spitzbergen. Ozone absorbs strongly in the ultraviolet Hartley and Huggins bands causing some absorbing layers to be optically thick. By contrast, in the visible, the much weaker absorption by NO_2 and O_3 renders each layer optically thin. Because of this, the enhancement factors for individual layers of NO_2 and O_3 are unaffected by the abundance of these gases in the other atmospheric layers, that is, each layer's individual

enhancement is independent of the distribution of gas in the other layers.

Effects of NO/NO_2 Chemistry on Slant Column Abundances

Unlike ozone, however, the concentration of NO_2 changes rapidly in twilight, making some correction necessary to account for the reaction that produces the NO_2 gas

$$NO + O_3 \rightarrow NO_2 + O_2 \tag{5.1}$$

and those that destroy it:

$$NO_2 + h\nu \rightarrow NO + O \tag{5.2}$$

$$NO_2 + O \rightarrow NO + O_2 \ . \tag{5.3}$$

This work will use the air masses computed by Dr. Susan Solomon [*McKenzie et al.*, 1991] which take into account the twilight photochemical reactions of NO_x and O_x. Solomon used a model to determine the ratio of the amount of NO_2 present at a particular solar zenith angle and level to that at 90°. The observed slant column abundance is (Eq. 4.4)

$$(NO_2)_{slant} = \delta \ N \tag{5.4}$$

where δ is the air mass factor and N is the vertical column abundance (cm^{-2}). N(z), the profile at 90° solar zenith angle, is the sought quantity. The profile, however,

changes with solar zenith angle as the NO/NO_2 partitioning shifts in response to the twilight radiation environment.

If the atmosphere is divided into J layers, the air mass, δ_{ij}, for each layer, j, at solar zenith angle, i, may be computed. Then for a particular solar zenith angle the slant column abundance is the air mass factor for each layer times the amount of NO_2 in that layer, summed over all of the layers. Thus Eq. 5.4 may be written as

$$(NO_2)_{i\ slant} = \sum_{j=1}^{J} \delta_{ij} NO_2(z_j) \qquad (5.5)$$

where $(NO_2)_{i\ slant}$ is the NO_2 slant column abundance at solar zenith angle i, $NO_2(z_j)$ is the column amount of NO_2 in the layer denoted by j, and J is the total number of layers. $NO_2(z_j)$ is changing with solar zenith angle, so $N_{i\ slant}$ in Eq. 5.5 is corrected for this fact by adjusting the air mass factors δ_{ij}. These air masses reflect the changing amount of NO_2 at various levels as the sun rises or sets. This is done despite the fact that the air mass for a given wavelength and layer depends only upon solar zenith angle; it is by definition the ratio of slant optical path to optical depth.

Altitude and Geometry Effects on Scattering

Consider singly-scattered light from the zenith sky

reaching a detector on the ground with a narrow field of view around the zenith direction. Three photon paths are shown in Figure 5.1 where γ is the solar depression angle (the solar zenith angle minus 90°) , r is the radius of the earth, h is the tangent height of the middle ray, z is the altitude of the middle ray's scattering point, and (180° - θ) is the scattering angle. For a given solar zenith angle, the light received by the detector is the sum of the downward scattered radiation from each level, attenuated by the extinction of the intervening medium on its way down to the detector. For simplicity of the illustration, the contributions due to multiple scattering are ignored here. In order for singly-scattered light to reach the detector, it must originate from directly above the detector. The intensity of this light singly-scattered in all directions, $I(z)_{scat}$, is given by

$$I(z)_{scat} \quad \alpha \quad \sigma_R n(z) I_z \tag{5.6}$$

where I_z is the direct beam intensity at level z, σ_R is the Rayleigh cross section and n(z) is the molecular number density. The direct beam intensity, I_z, has been attenuated from its value at the top of the atmosphere, I_o, by scattering and absorption

$$I_z = I_o e^{-\tau_{ext}} \tag{5.7}$$

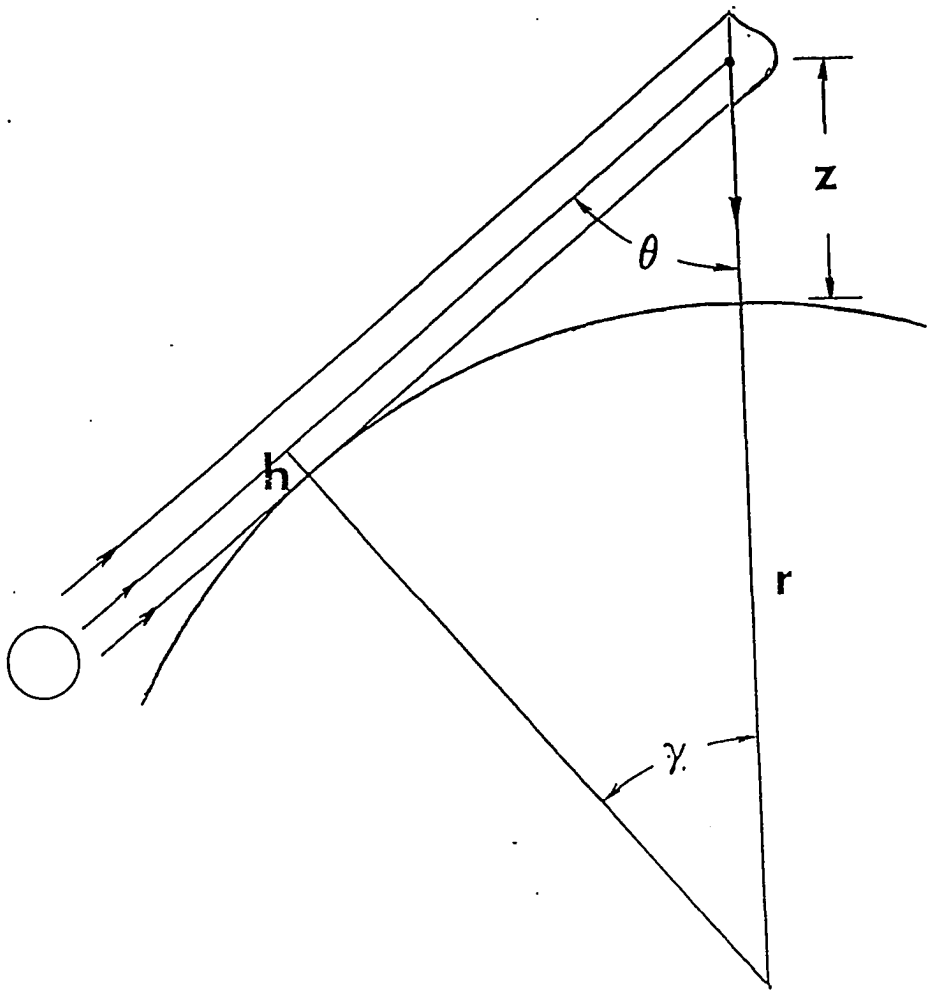

Figure 5.1: The geometry of twilight considering only single scattering. The perigee height of the middle ray is h, r is the radius of the earth, γ is the solar depression angle, z is the altitude where scattering is maximum, and (180° - θ) is the scattering angle. The Gaussian shape centered at altitude z represents the intensity of the scattered light originating at different altitudes.

where the optical path, τ_{ext}, is

$$\tau_{ext} = \tau_{scat} + \tau_{abs} , \qquad (5.8)$$

τ_{scat} is the optical path due to scattering, and τ_{abs} that due to absorption.

According to Eq. 5.6, the scattered light, $I(z)_{scat}$, will maximize at some altitude because the direct beam intensity, I_z, increases with altitude, Eq. 5.7, whereas the molecular density decreases approximately exponentially with altitude. Rayleigh scattering is proportional to $1/\lambda^4$, so light of shorter wavelengths will be scattered more efficiently than light of longer wavelengths. Thus, for a given solar zenith angle, the altitude at which $I(z)_{scat}$ maximizes is higher for shorter wavelengths. The position of the maximum moves to higher altitudes as the solar zenith angle increases because of the longer path lengths through the dense lower levels of the atmosphere. In addition, the lower levels of the atmosphere are in shadow as the solar zenith angle exceeds 90°. The Gaussian shape in Figure 5.1 represents the scattered intensity from different altitudes which reaches its maximum at altitude z and decreases at higher and lower altitudes. The width of the scattering region is between 15 and 30 km [*Volz and Goody*, 1962]. *Shaw* [1981] gives a general treatment of single scattered light at twilight including the retrieval of stratospheric aerosol

altitude profiles from the sky color ratio (λ_1/λ_2) and the logarithmic brightness gradient which express how quickly the scattered light reaching the ground diminishes as the sun sets.

The intensity of radiation originating from a particular altitude and singly-scattered into to an angle ϵ (180° - θ in Figure 5.1) with respect to the direction of incidence is obtained by multiplying Eq. 5.6 by the fraction of light scattered in this particular direction, i.e. the phase function, $P(\epsilon)$

$$I(z,\epsilon)_{scat} = I_o\, e^{-\tau_{ext}}\, n(z)\ \sigma_R\, P_R(\epsilon) \qquad (5.9)$$

where one assumes that the scattering is by molecules only so that the appropriate phase function is that for Rayleigh scattering, $P_R(\epsilon)$.

5.2 Theoretical Basis for Inversion

The kernel and inversions

It was shown that for each solar zenith angle there is an altitude from which the greatest fraction of scattered light originates. The optical path due to an absorbing layer for scattered light reaching the detector will be greatest when the bulk of the absorber is located at this altitude. This is because at this solar zenith angle most of the light reaching the detector has traveled through the

absorber in an extended path. It is for this reason that the air masses for different layers in Figure 4.4 show maxima at different solar zenith angles. Air mass values in conjunction with a measured time series of NO_2 slant column abundance can be used to determine the NO_2 profile.

The problem of using a set of measurements to infer a second quantity indirectly when the two are connected by a Fredholm integral has been discussed by *Twomey* [1977] and *Chahine* [1977]. The problem relates the measured quantity, a function of one variable, to the desired quantity, a function of a second variable, via the kernel, which is a function of both of the variables. The kernel may be thought of as the contribution or weighting function which, when convolved with the desired function yields the measured function. In the present case, the desired quantity is the NO_2 profile (a function of z), the measured quantity is series of measured NO_2 slant column abundances (a function of solar zenith angle), and the kernel a set of air masses (a function the two). The approach will be to reconstruct a time series of NO_2 slant column abundances using Eq. 5.5 and compare this with the measured time series of NO_2 slant column abundances. The differences between the reconstructed and measured time series will be minimized by judiciously adjusting the NO_2 profile.

In the case of a discrete set of measurements, g_i,

taken at integer solar zenith angles, i

$$g_i = \sum_{j=1}^{J} K_i(z_j) f(z_j) \equiv \sum_{j=1}^{J} K_{ij} f_j \tag{5.10}$$

where $g(i) = (NO_2)_{i\ slant}$, $f_j = f(z_j) = NO_2(z_j)$ and $K_{ij} = K_i(z_j) = \delta_{ij}$. $K_i(z_j)$ is the kernel and $f(z_j)$ is the unknown quantity. Inversion is the process of solving for $f(z_j)$.

If measurements are made at N solar zenith angles, one finds

$$\begin{aligned} g_1 &= \sum_{j=1}^{J} K_{1j} f_j = K_{11} f_1 + K_{12} f_2 + \ldots + K_{1J} f_J \\ g_2 &= \sum_{j=1}^{J} K_{2j} f_j = K_{21} f_1 + K_{22} f_2 + \ldots + K_{2J} f_J \\ &\vdots \\ g_N &= \sum_{j=1}^{J} K_{Nj} f_j = K_{N1} f_1 + K_{N2} f_2 + \ldots + K_{NJ} f_J \end{aligned} \tag{5.11}$$

which may be written in matrix form as

$$\vec{g} = \tilde{K}\,\vec{f} \tag{5.12}$$

where

$$\vec{g} = \begin{vmatrix} g_1 \\ g_2 \\ \vdots \\ g_N \end{vmatrix}, \quad \vec{f} = \begin{vmatrix} f_1 \\ f_2 \\ \vdots \\ f_J \end{vmatrix} \tag{5.13}$$

and K is the N x L matrix

$$\tilde{K} = \begin{vmatrix} K_{11} & K_{12} & \cdots & K_{1L} \\ K_{21} & K_{22} & \cdots & K_{2L} \\ \vdots & & & \\ K_{N1} & K_{N2} & \cdots & K_{NL} \end{vmatrix} \tag{5.14}$$

The NO_2 profile is sought, which requires the inversion of Eq. 5.12. The set of measured NO_2 slant column abundances at different solar zenith angles i, $g_i = (NO_2)_{i\ slant}$ can be used with the kernel corresponding to the air mass values for various levels $K_{ij} = \delta_{ij}$ to invert for the NO_2 profile, $f_j = NO_2(z_j)$. Thus, the computation of δ_{ij}, using Eq. 4.10 from solar zenith angles from 85° to 95° in 1° increments for each of the nine layers from 0 to 45 km, results in a 11 x 9 matrix of air masses. Figure 4.4 showed air mass versus solar zenith angle for the 9 layers with clear sky, no aerosols or chemistry included. For angles of less than 87°, the air mass values show little difference implying a high degree of linear dependence in the kernel for these angles.

The actual slant column abundance is the sum of the measured slant column abundance of NO_2 plus the slant column amount of NO_2 in the spectrum used as a control (Eq. 3.1). Thus, the actual observed slant column amount $F^{obs}{}_i$ at angle i is

$$F_i^{obs} = (NO_2)_{i\ slant} + F_o \tag{5.15}$$

where F_o is the amount of NO_2 in the control and $(NO_2)_{i\ slant}$ is the observed slant column at angle i. This actual observed time series is compared with the reconstructed time series of slant column abundances $F^{recon}{}_i$ which is the matrix multiplication of the air mass factors at each level times the profile:

$$F_i^{recon} = \sum_{j=1}^{9} \delta_{ij} NO_2(z_j) \qquad (5.16)$$

where $F^{recon}{}_i$ is the reconstructed slant column corresponding to a solar zenith angle i, δ_{ij} is the air mass for layer j at angle i, and $NO_2(z_j)$ is the amount of NO_2 in layer j. Inversion of the matrix Eq. 5.11, were δ_{ij} square and non-singular, would yield the absorber profile $NO_2(z_j)$. If one makes the matrix square by reducing the number of angles to 9 and inverts, the solution vector oscillates wildly. This is primarily due to measurement uncertainties which increase with solar zenith angle as the signal to noise decreases. Furthermore, there is little information to distinguish the layers at solar zenith angles of less than 87° (see Figure 4.4). Inverting measurements with noise or using air mass values that exhibit linear dependence over some range of angles can yield physically unreasonable results, so a constraining process is needed.

Following the work of *McKenzie et al.* [1991], the

weighted iterative Chahine method was used to constrain the solutions [*Chahine,* 1977; *Twomey,* 1977]. Each layer has a solar zenith angle for which the air mass reaches its maximum. The angles of maximum response for the various layers are used to adjust the profile during iteration when comparing the measured time series with the modeled time series. This method converges most quickly when there are distinct maxima for each separate altitude but also works if each altitude response function is distinct from the others. As can be seen from Figure 4.4, at altitudes greater than 30 km there is not a unique correspondence between zenith angle and maximum of the air mass. Thus, less information about the NO_2 distribution in these upper levels can be obtained.

To solve for the species concentration at each level, the air mass matrix is multiplied by the current (n^{th}) profile solution vector $[NO_2(z_j)]^n$ in Eq. 5.12 to compute the reconstructed F_i^{recon} at each angle. Repetition for each solar zenith angle yields the reconstructed time series. The profile is adjusted by comparing the reconstructed time series to the measured time series. The differences between the observed and the reconstructed slant columns at each angle, $F^{obs}{}_i - F^{recon}{}_i$, are summed and squared, resulting in the overall residual

$$Res = \sum_i (F_i^{obs} - F_i^{recon})^2 \ . \qquad (5.17)$$

Using the iteration formula, a new profile, $[NO_2(z_j)]^{n+1}$, is generated and the process continued until the residual is acceptably low. The unweighted Chahine formula for the $(n+1)^{st}$ estimate of the vertical profile C_j^{n+1} is

$$NO_2(z_j)^{n+1} = NO_2(z_j)^n (F_{k(j)}^{obs} / F_{k(j)}^{recon}) \qquad (5.18)$$

where k(j) is the solar zenith angle at which layer j has the maximum air mass. The weighted Chahine iteration formula used in the McKenzie algorithm is

$$NO_2(z_j)^{n+1} = NO_2(z_j)^n \cdot p \qquad (5.19)$$

with

$$p = \sum_{m=1}^{J} [W_{jm} \cdot (F_{k(m)}^{obs} / F_{k(m)}^{recon})] \ . \qquad (5.20)$$

W_{jm} are normalized weighting factors to insure convergence in view of the linear dependence in some of the rows of S_{ij}. The unnormalized factors W'_{jm} are computed by

$$W'_{ij} = S_{k(m)j} \ / \ S_{k(m)m} \qquad (5.21)$$

for the layers m. W'_{jm} are normalized using

$$W_{jm} = W'_{jm} / X_m \qquad (5.22)$$

with

$$X_m = \sum_{j=1} W_{jm} \ . \qquad (5.23)$$

Dr. Richard McKenzie [personal communication, 1993] kindly made available his profile retrieval software. Three measured time series of slant column abundances for NO_2 were linearly interpolated to get slant column abundance at integer solar zenith angles from 85° to 95°. The dates of the inversion were February 25 (p.m.), March 14 (a.m.), and April 9 (p.m.). Figure 5.2 shows the profiles. It can be seen that the maximum concentration of NO_2 centered around 27.5 km in late winter and early spring of 1993. From these three measurements, there is no evidence of a shift in the profile maximum.

5.3 Errors Associated with Retrievals

The errors with the retrievals are associated with measurement noise of the slant column values, initial guess of profile, effects of other atmospheric absorbers, effects of NO_2 twilight chemistry, amount of NO_2 in the control spectrum, and possible tropospheric pollution.

To test the consistency of the inversion scheme, the radiative transfer model was used to compute twilight zenith intensities and then this simulated time series was inverted to retrieve the NO_2 profile in the model. A layer of NO_2 in

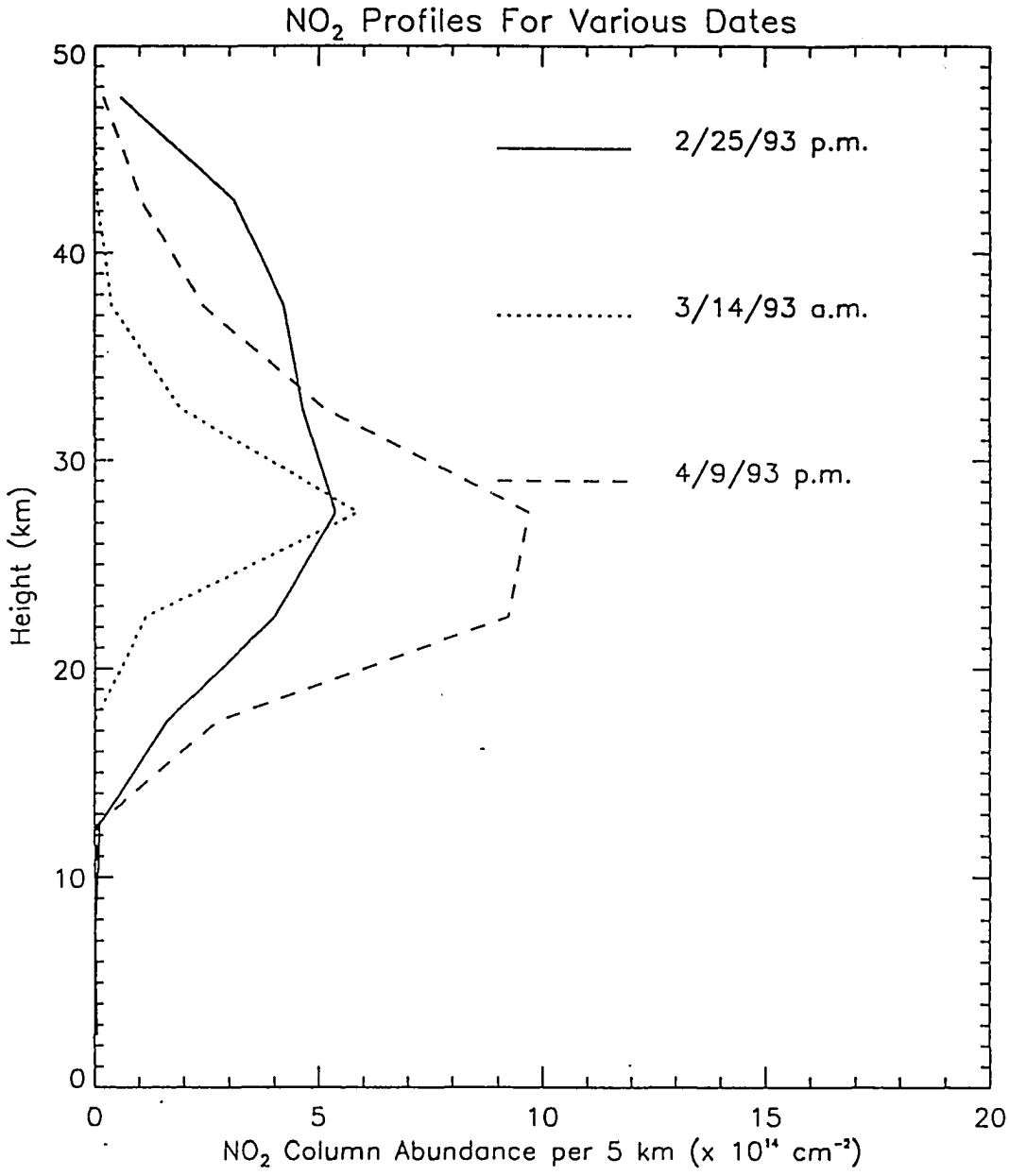

Figure 5.2: NO_2 vertical profiles retrieved from 2/25/93 p.m. (solid), 3/14/93 a.m. (dotted), and 4/9/93 p.m. (dashed).

the shape of a Gaussian with peak concentration at 27.5 km, full width half maximum (FWHM) of 10 km, and total column abundance 3.0×10^{15} was input to the model. Zenith intensities were computed with the radiative transfer model at 450 nm, with and without absorber, from 85° to 95°. Air mass factors were determined using Eq. 4.10. Simulated slant column abundances were obtained by Eq. 5.12. Measurement uncertainty was included with the simulated time series, increasing continuously with solar zenith angle from 3% at 85° to 21% at 95°. This time series was inverted with the McKenzie algorithm and the retrieved profile compared with the model starting profile as shown in Figure 5.3. Both have peaks at 27.5 km, but the retrieved profile is somewhat broader with a FWHM of 13 km. The total column abundance of the retrieved profile is 9.2% greater than that of the profile input to the radiative transfer model. The differences are probably due to using Solomon's air mass values for the inversion which do not include multiple scattering.

As another test of the consistency of the algorithm, the February 25, 1993 time series was inverted to yield a profile. The reconstructed time series was then used as input to the algorithm and a second profile retrieved. Figure 5.4 shows the comparison of the two profiles revealing only minor differences. Next, simulated random

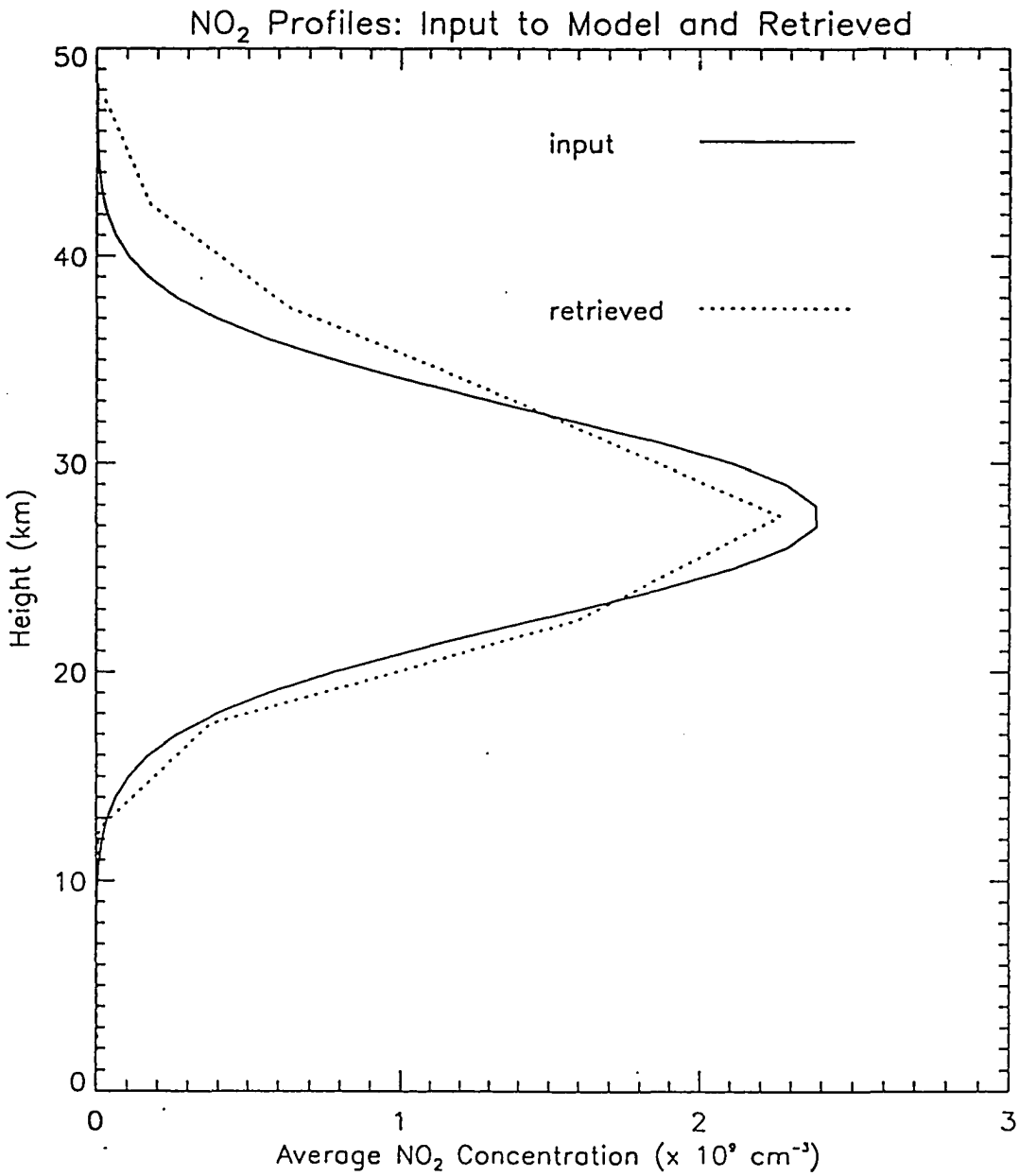

Figure 5.3: NO_2 vertical profiles retrieved from modeled zenith intensities (dotted) compared with input to model (solid).

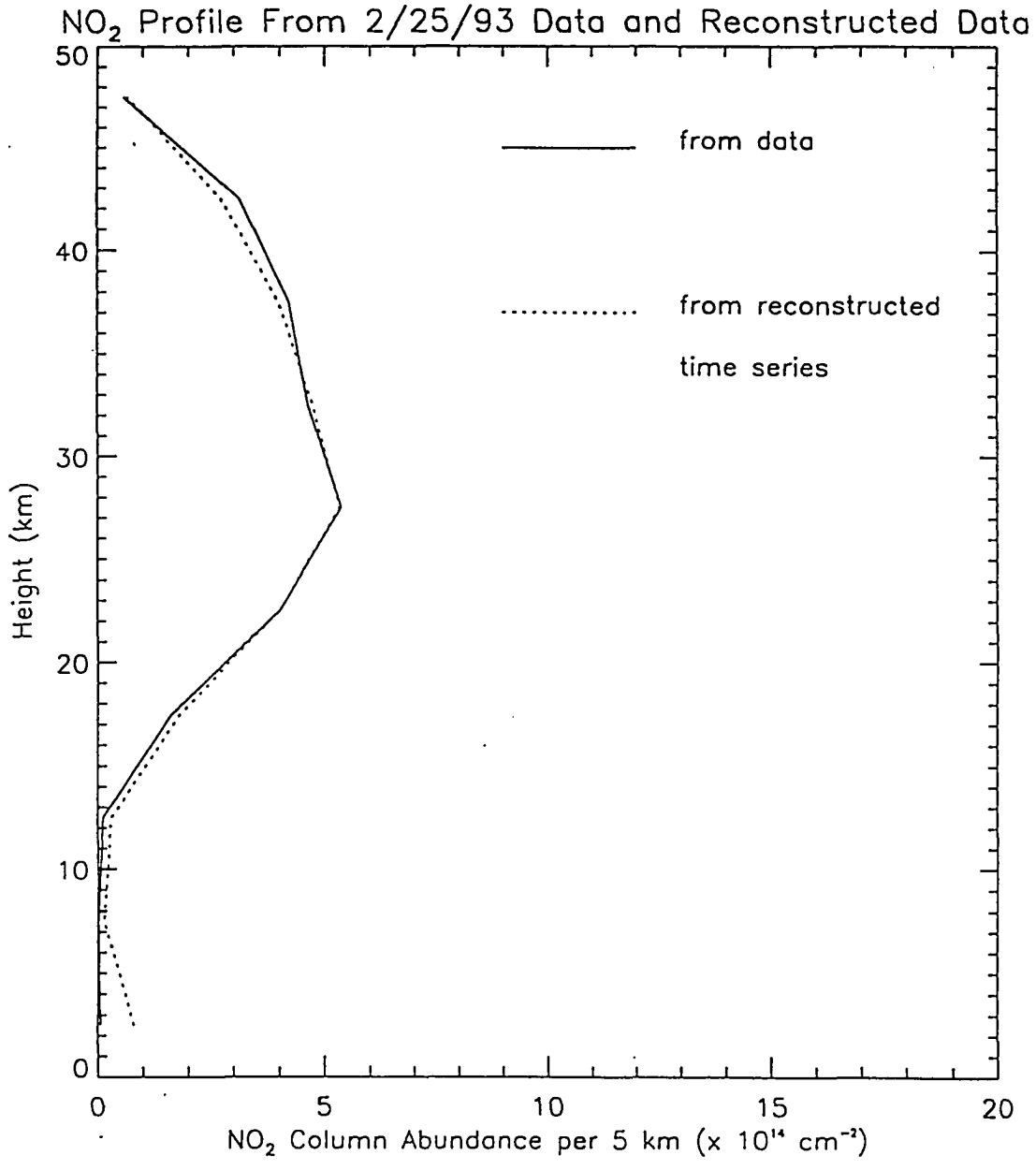

Figure 5.4: NO_2 vertical profiles retrieved from 2/25/93 p.m. measurements (solid) and from reconstructed time series (dotted).

measurement noise was added to this same time series with maximum noise values of 1, 5, and 10% (corresponding to r.m.s noise of 0.7, 3.5, and 7%). The profiles resulting from inverting these degraded times series is shown in Figure 5.5. The profiles are all similar in shape except for the one derived from the time series with the largest noise. This indicates the soundness of the inversion algorithm.

Next the effect of including NO/NO_2 chemistry on retrievals of measured slant columns was studied . Figure 5.6 shows the retrieved profile from the p.m. slant column abundances taken at Fairbanks on April 9, 1993 using air masses without NO/NO_2 chemistry (solid line) and with chemistry included (dotted line). Using air masses that account for chemistry results in a broader and lower maximum with a slightly higher tropospheric contribution. The total column abundance using air masses without chemistry was 2.78 x 10^{15} and for those using chemistry is 3.08 x 10^{15}, a difference of 10.1%. The number of iterations were 500 for both no chemistry and including chemistry but the residuals of Eq. 5.13 were 2.20 for no chemistry and 0.12 for chemistry.

The amount of NO_2 contamination in the control was another source of error in retrieved profiles. This value was estimated by using Eq. 3.25 [*McKenzie and Johnston*,

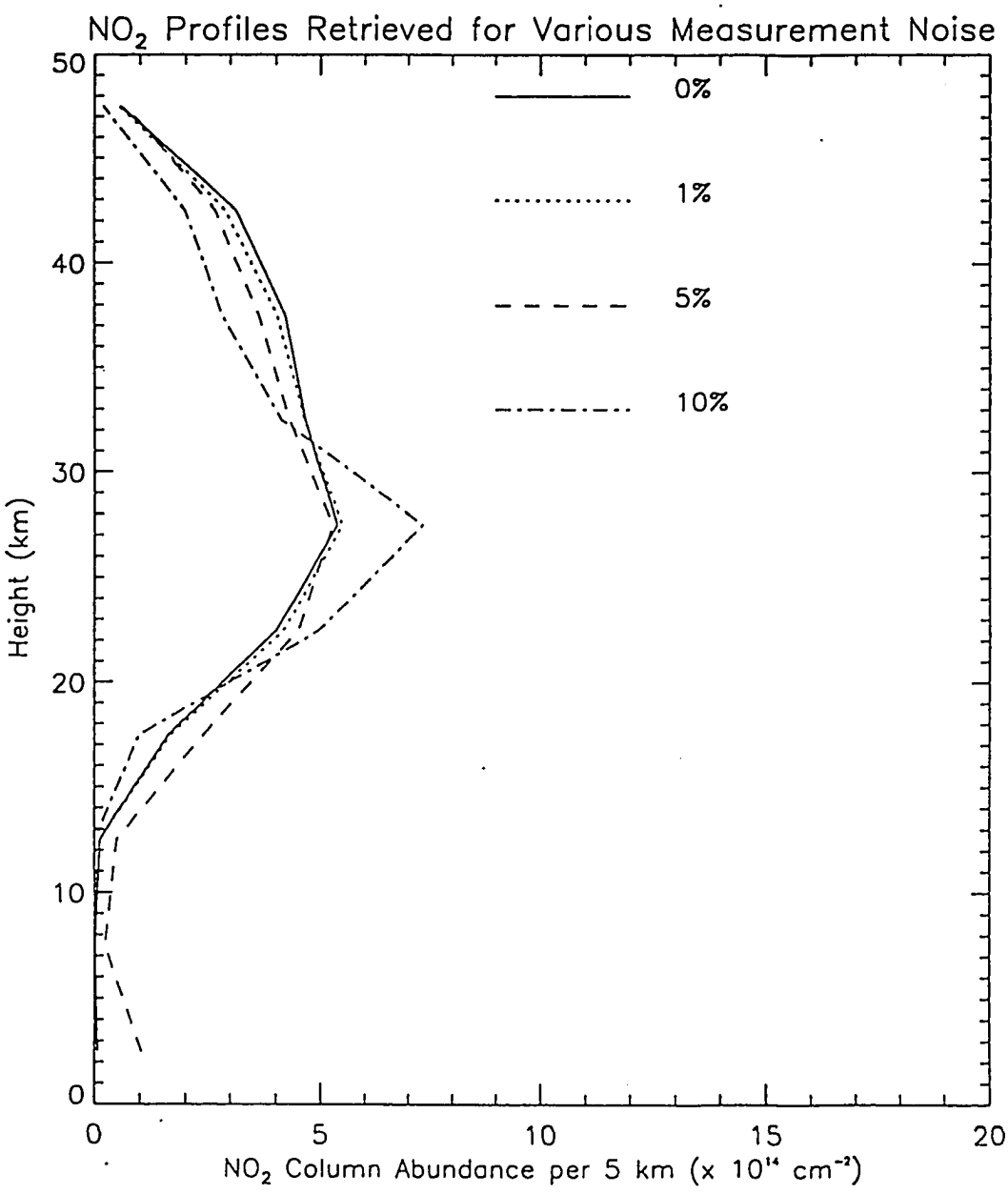

Figure 5.5: NO_2 vertical profiles retrieved from 2/25/93 p.m. for various amounts of random noise added to the measured time series: 0% (solid), 1% (dotted), 5% (dashed), 10% (dashed–dotted).

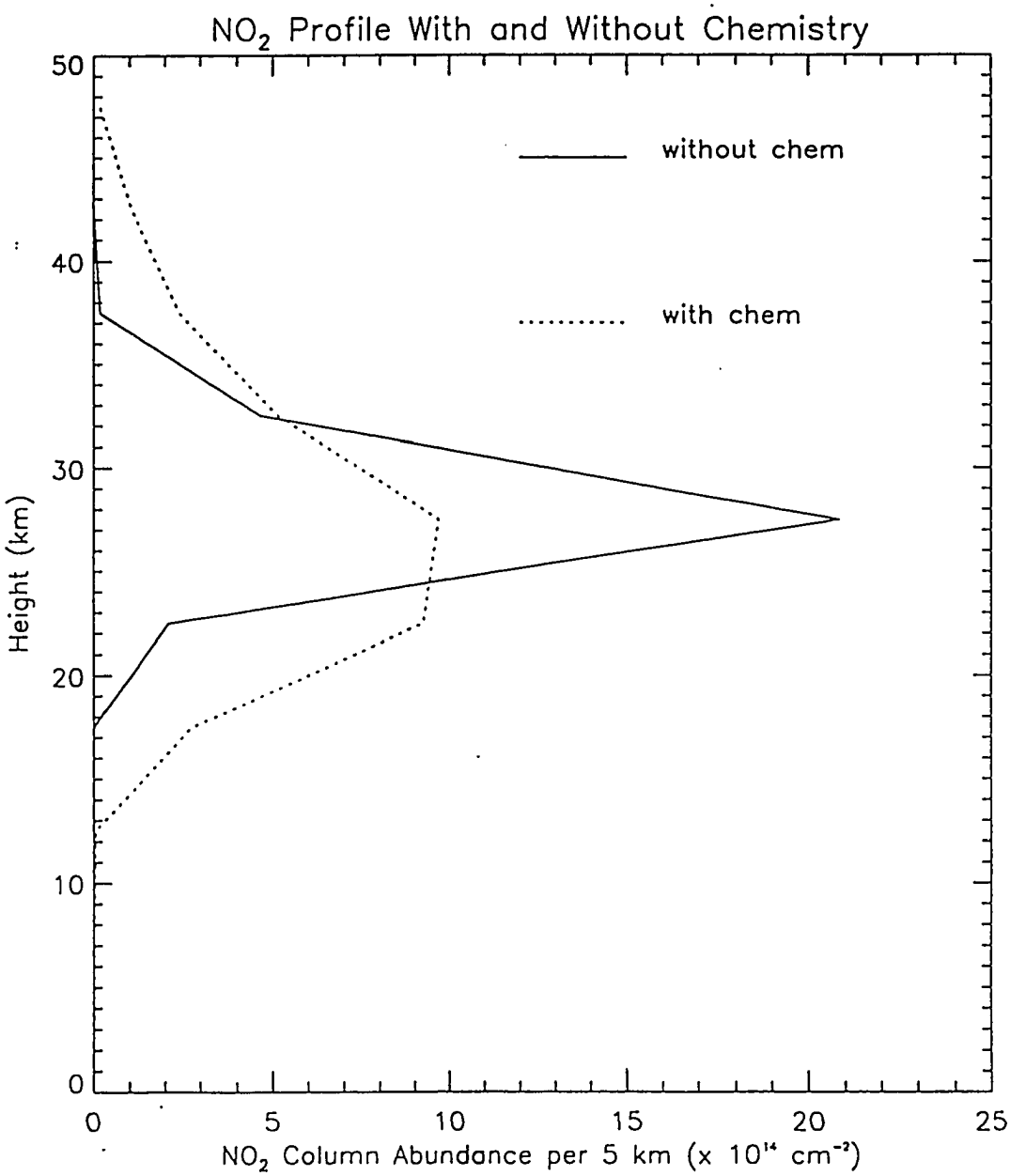

Figure 5.6: NO_2 vertical profiles retrieved from 4/9/93 p.m. using airmass factors computed with and without chemistry.

1983]. The amount of NO_2 in the control was 0.43 x 10^{16} cm^{-2} for April 9; this value was multiplied by 0.5 and 1.5 to see the effect on the retrieved profile. Figure 5.7 shows the retrieved profile for April 9, 1993 using the control multiplied by 0.5 (dashed line), by 1.0 (solid line) and by 1.5 (dash-dotted line). Having less NO_2 in the control shifts the profile to levels where it is at a maximum, and having too much shifts it to the lower levels. The estimated uncertainty in the control is about ± 10%.

Another source of error in the inversion scheme was the uncertainty in the air mass. The adopted air masses include chemistry, but were computed with a radiative transfer model utilizing single scattering and so are expected to be less accurate at large solar zenith angles. To investigate the effect of multiple scattering, the range of angles were truncated at 95°, 94°, 93°, and 92° and the retrieved profiles compared. Figure 5.8 shows profiles retrieved over ranges of angles ending at 95° (solid), 94° (dotted), 93° (dash-dotted), and 92° (dash-dot). It is seen that cutting off the largest solar zenith angles pushes the profile lower. This is because most of the information about the highest levels comes from the largest solar zenith angles when the height of maximum scattering is at these levels.

Sensitivity to initial guess was next investigated.

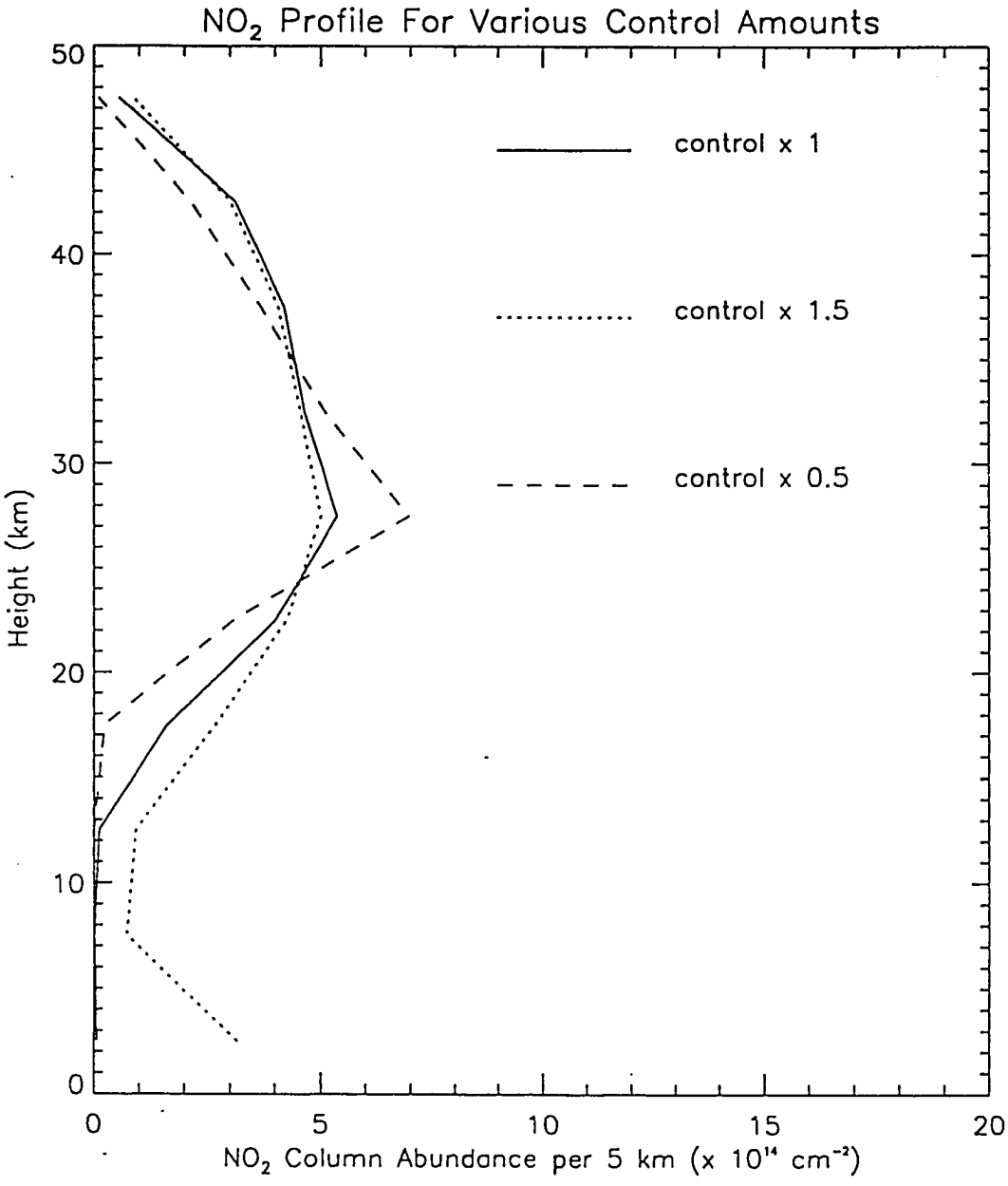

Figure 5.7: NO_2 vertical profiles retrieved from 4/9/93 p.m. measurements with various amounts of control added.

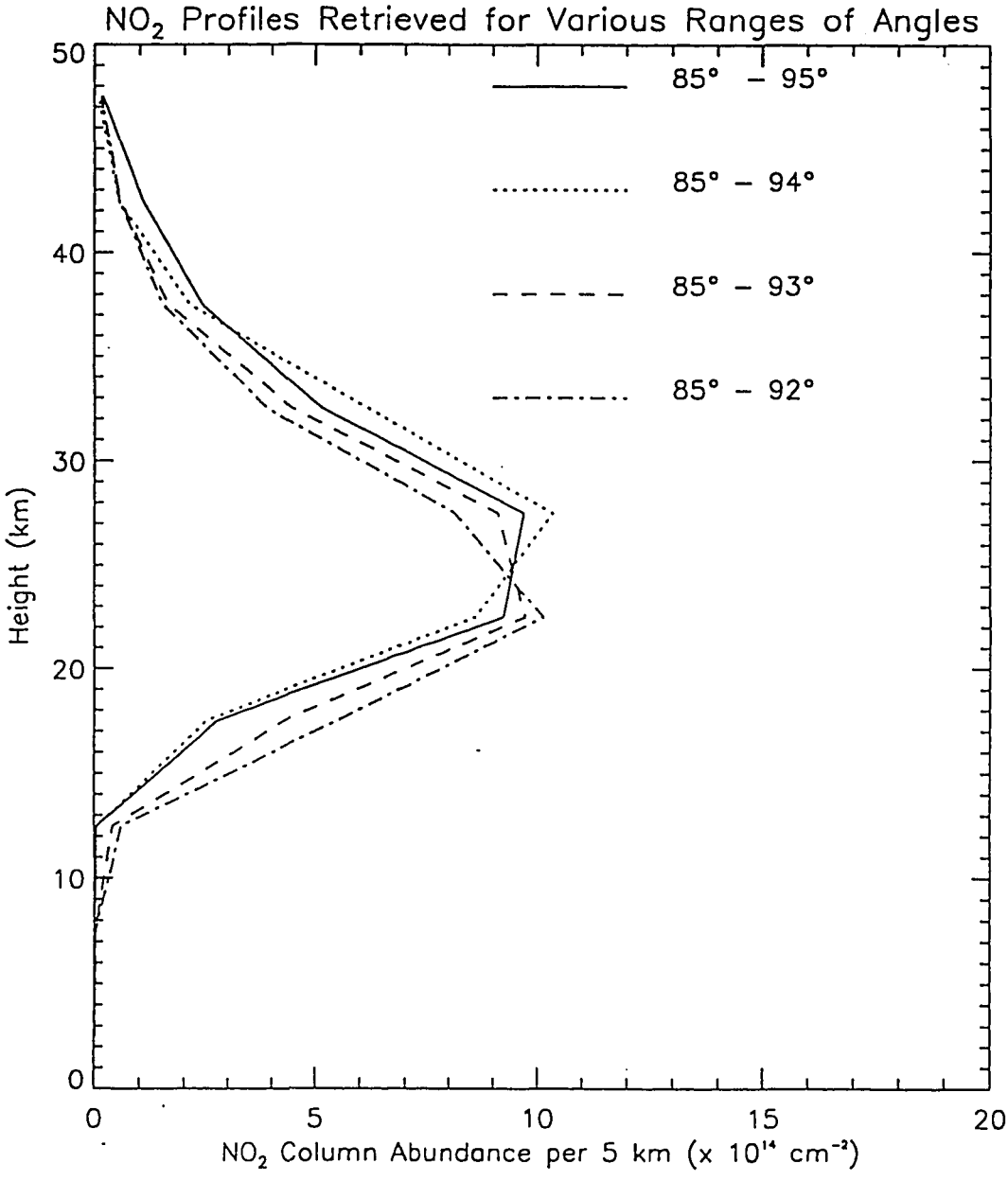

Figure 5.8: NO_2 vertical profiles retrieved from 4/9/93 p.m. for various ranges of angles: 85° – 95° (solid), 85° – 94° (dotted), 85° – 93° (dashed), 85° – 92° (dash–dotted).

Figure 5.9 shows profiles retrieved under various initial guesses: constant concentration (solid line), constant mixing ratio which is an exponential falloff in concentration (dashed line), an NO_2 profile climatology (dotted line), a Gaussian centered at 25 km (dashed-dot). Although all four converged, the profile retrieved using the climatology as an initial guess resulted in the smallest fitting errors, suggesting that knowledge of NO_2 climatology is useful for accurate retrieval of profiles.

Vertical profiles which are roughly consistent in shape with those obtained by *McKenzie et al.* [1991] at 45° S have been determined from time series of slant column abundances. Determination of the NO_2 distribution above 30 km was limited by the low signal to noise for measurements with the solar zenith angle greater than 95°. Use of air masses that included NO/NO_2 chemistry resulted in smaller fitting errors and faster convergence, indicating the importance of chemistry in determining the profile.

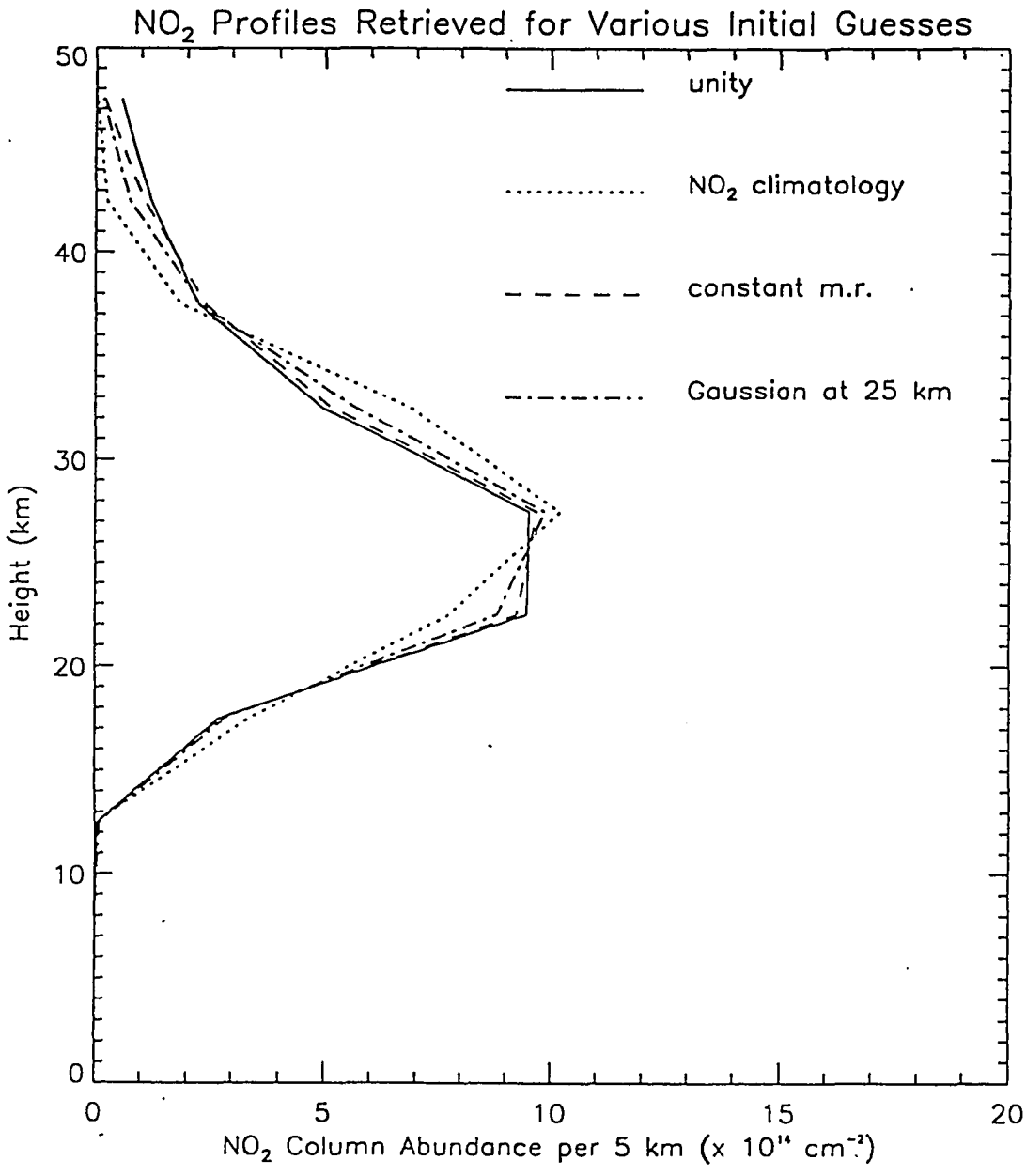

Figure 5.9: NO_2 vertical profiles retrieved from 4/9/93 p.m. with initial guess of unity (solid), NO_2 climatology (dotted), constant mixing ratio (dashed), and Gaussian centered at 25 km (dash–dotted).

Chapter 6

Fairbanks Campaign

6.1 Theoretical Chemical Considerations in Polar Latitudes

A question of key importance to the study of the Arctic stratospheric ozone budget is the extent of heterogeneous reactions of nitrogen compounds on the surfaces of aerosols composed of water and sulfuric acid [*Mozurkewitch and Calvert,* 1988]. It is hypothesized that these reactions are occurring on sulfate aerosols. This will be tested by analyzing a series of NO_2 and HNO_3 column measurements, upper air temperatures, and lidar measurements to determine the extent of the aerosol layer. These heterogeneous reactions have important implications for ozone abundance because they convert N_2O_5 to HNO_3, a more stable nitrogen reservoir. This leads to a decreases in NO_x (NO and NO_2) which allows ozone destroying atomic Cl to build up. Of these reactions the most important one is

$$N_2O_5 + H_2O\ (sulfate\ aerosol) \rightarrow 2\,HNO_3\ . \qquad (6.1)$$

A less important reaction in the stratosphere requiring colder temperatures is

$$ClONO_2 + H_2O\ (sulfate\ aerosol) \rightarrow HOCl + HNO_3\ . \qquad (6.2)$$

Reaction (6.1) occurs on aerosols composed of mixed sulfuric acid and water and is known to proceed with high efficiency in the laboratory [*Hanson and Ravishankara,* 1991; *Tolbert et al.,* 1988a, 1988b] at temperatures higher than those required for the formation of polar stratospheric clouds (PSCs). Reaction (6.2) is thought to require frozen aerosols and thus colder temperatures; even under these conditions it is much slower than reaction (6.1) [*Hanson and Ravishankara,* 1991].

Normally the stratospheric aerosol layer is so thin that heterogeneous reactions such as (6.1) and (6.2) do not proceed with measurable efficiency. Exceptions occur in the polar winter when polar stratospheric clouds form and after major volcanic eruptions when the aerosol surface area is greatly enhanced. The Mount Pinatubo eruption in June 1991 was one of the largest of the century, resulting in the production of the order of 20-30 Megatons of new aerosols [*McCormick and Veiga,* 1992].

The Second Arctic Airborne Stratospheric Experiment flew extensive missions in the Arctic during winter 1992-93 to characterize the stratospheric chemistry of this region. *Wilson et al.* [1993] measured the aerosol size distribution at around 20 km with a Condensation Nucleus Counter and

determined that in late 1991, the total aerosol surface area was enhanced by a factor of 30 or more over pre-volcanic levels. Assuming an exponential decline, the e-folding time of the stratospheric aerosol layer after a major volcanic eruption is estimated to be about one year [*McCormick et al.*, 1978]. Therefore, by the winter of 1993, the stratospheric aerosol total surface area would be expected to have decreased by approximately 80 percent of its post-volcanic maximum.

Although stratospheric temperatures over Fairbanks were never cold enough for the formation of PSCs, it is useful to briefly summarize the heterogeneous reactions that occur on the surfaces of PSCs. In the frigid Antarctic and in the somewhat warmer Arctic stratosphere, PSCs provide aerosol surfaces on which heterogeneous reactions may proceed. These reactions reduce reactive nitrogen such as NO_2 and release reactive chlorine such as Cl_2 allowing catalytic ozone destroying reactions involving chlorine compounds to proceed. There are two major types of PSCs. Type I form at -78°C and are composed primarily of nitric acid trihydrate, NAT. Type II, composed of ice and NAT, form at -85°C. A prerequisite for the chlorine induced ozone losses in Antarctica is low levels of NO_2 which allow ClO to build up. ClO reacts with NO_2 and a third molecule to form the relatively stable compound chlorine nitrate

$$ClO + NO_2 + M \rightarrow ClONO_2 + M \quad (k_3 = 4.3x10^{-12}\ cm^6 s^{-1}) \ . \quad \textbf{(6.3)}$$

The reaction coefficient k_3 was calculated using the *DeMore et al.* [1990] formula for 220 K and 35 mbar (about 23 km). ClO reacts with NO_2 with a much greater probability than it does with O_3.

$$ClO + O_3 \rightarrow OClO + O_2 \qquad (k_4 = 1.3x10^{-20}\ cm^3 s^{-1}) \ . \quad \textbf{(6.4)}$$

OClO is an important reaction intermediate to ozone destruction (Eqns. 1.22-1.30).

To better characterize the chemical budget of species, it is useful to group the trace gases into families. NO_x is defined as $(NO + NO_2)$ and O_x is $(O + O_3)$. Odd nitrogen, defined as $NO_y = (NO + NO_2 + ClONO_2 + HONO_2 + 2N_2O_5 + HNO_3)$, forms a series with NO at one end (the most reduced) and HNO_3 at the other (the most oxidized). The chlorine family is defined as $Cl_y = (ClO + 2Cl_2O_2 + HOCl + ClONO_2 + HCl)$. $ClONO_2$ is common to both families and thus links the two. Compounds of the HO_y family $(OH + HO_2 + 2H_2O_2 + HO_2NO_2)$ are less important than the NO_y and Cl_y families in the lower stratosphere, although at higher altitudes they play a more dominant role. In the polar winter stratosphere, the partitioning of the nitrogen oxides (NO_y) and the chlorine species (Cl_y) between the reactive species such as NO, NO_2, and ClO, and the relatively inert reservoir species such as N_2O_5, HNO_3, $ClONO_2$ and HCl, influences the ozone abundance

through various competing catalytic cycles. Figure 6.1 shows the major reactions within the NO_x, ClO_x, and HO_x families [*World Meteorological Organization,* 1986].

NO_x and N_2O_5 diurnal chemistry

The nitrogen oxides are partitioned due to the radiation environment of the stratosphere except in the case of heterogeneous reactions. In daylight, NO and NO_2 are in a rapid photochemical equilibrium, with their abundance ratio depending mainly on solar zenith angle, altitude and ozone abundance [*Brasseur and Solomon,* 1986]. The major reactions governing the NO/NO_2 ratio in the lower stratosphere are

$$NO_2 + h\nu \rightarrow NO + O \ (\lambda < 405nm) \tag{6.5}$$

$$NO_2 + O \rightarrow NO + O_2 \tag{6.6}$$

$$NO + O_3 \rightarrow NO_2 + O_2 \ . \tag{6.7}$$

There are additional reactions of NO_x with the oxides of chlorine, hydrogen and bromine whose abundances are normally much smaller than NO_x or O_x. An exception is within the Antarctic and to a lesser extent the Arctic vortices where ClO abundances are enhanced. During the daylight NO and NO_2 reach a steady state. In the chemically unperturbed lower stratosphere, where $[O_3] >> [O]$ or $[ClO]$ or $[HO_2]$, the only reactions forming and destroying NO_2 are (6.5) and (6.7).

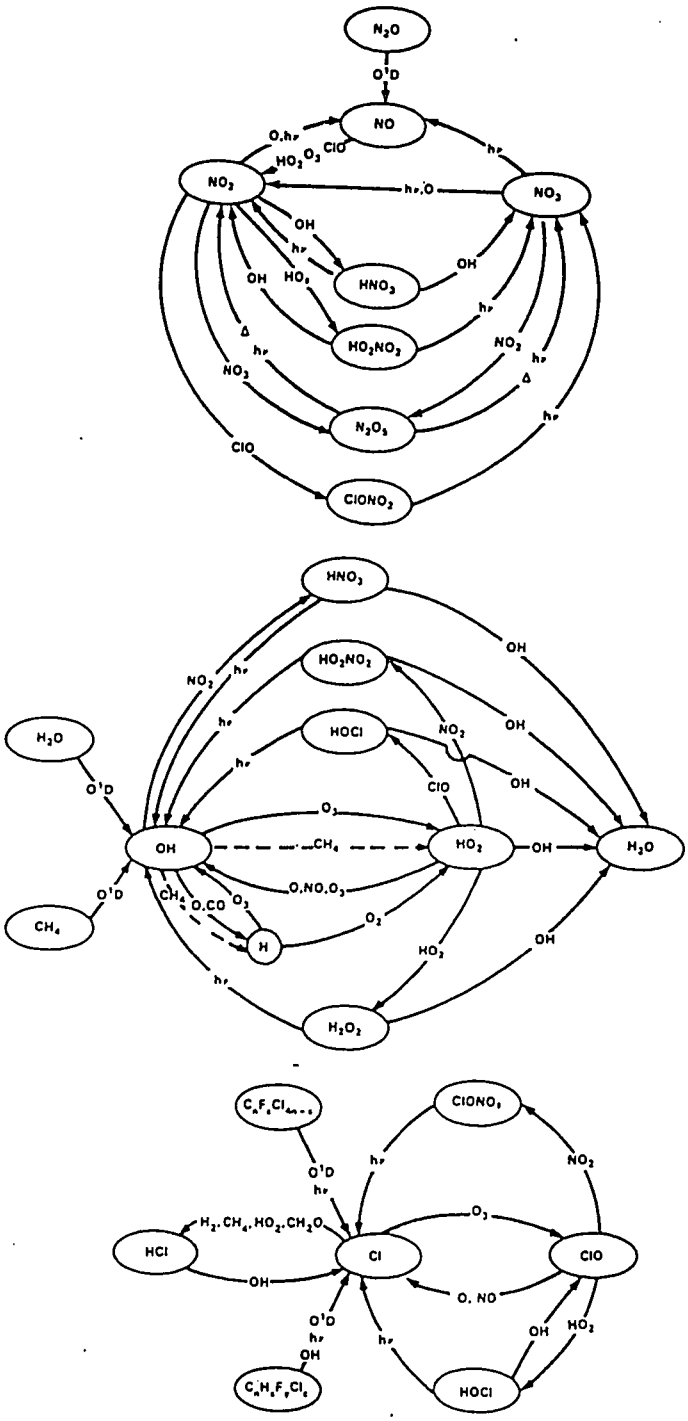

Figure 6.1: The various chemical cycles of the NO_x (top), HO_x (middle), and ClO_x (bottom) families. From *Atmospheric Ozone, 1985,* World Meteorological Organization, Geneva, 1986.

One can write

$$\frac{d[NO_2]}{dt} = 0 = k_7 [O_3] [NO] - J_{NO_2} [NO_2] \quad . \tag{6.8}$$

Thus the ratio of NO to NO_2 concentrations is approximately

$$\frac{[NO]}{[NO_2]} \approx \frac{J_{NO_2}}{k_7 [O_3]} \quad . \tag{6.9}$$

The partitioning of odd nitrogen shifts from NO to NO_2 during twilight and then proceeds towards NO_3 and N_2O_5 once the sun has set. NO_3 cannot build up during the daytime because it is so easily photolyzed

$$NO_3 + h\nu \rightarrow NO_2 + O \quad (\lambda < 662 \ nm) \quad . \tag{6.10}$$

NO_3, formed by NO_2 reacting with ozone, starts to increase as soon as the sun sets

$$NO_2 + O_3 \rightarrow NO_3 + O_2 \quad (k_{10} = 1.2 x 10^{-13} e^{-2450/T}) \quad . \tag{6.11}$$

NO_3 reacts with NO_2 and a third molecule to form the temporary NO_x storage reservoir species, N_2O_5, a molecule central to this study

$$NO_3 + NO_2 + M \rightarrow N_2O_5 + M \quad . \tag{6.12}$$

The N_2O_5 molecule is photolyzed rather easily and thus begins to return to NO_2 as soon as the morning sun rises

$$N_2O_5 + h\nu \rightarrow NO_2 + NO_3 \quad (\lambda < 380 \ nm) \quad . \tag{6.13}$$

N_2O_5 also undergoes thermal decomposition, the reverse of reaction (6.12), at a rate that depends upon pressure and temperature. At a pressure of 16.8 mbar (an altitude of about 27.5 km) and 220 K, its thermal lifetime is about 64 hours [*DeMore et al.*, 1990]. After 12 hours, thermal decomposition results in a 17% reduction of N_2O_5. For comparison, the photolysis lifetime at 20 km for a constant solar zenith angle of 80° is on the order of 30 hours [*Kawa et al.*, 1992].

N_2O_5 begins to accumulate in the polar night as more is formed than can be photolyzed during the day. An important diagnostic tool in studying the partitioning of the odd nitrogen species is the ratio of sunrise to sunset NO_2, which for a particular level allows calculation of the fraction of NO_2 that has been transformed into N_2O_5 overnight. The fastest of the two steps for the formation of N_2O_5 is reaction (6.11), which is extremely temperature sensitive. *Naudet et al.* [1981] showed in a detailed chemical calculation that the NO_3 produced from reaction (6.11) quickly attains a steady state concentration. This means that every NO_3 molecule formed from reaction (6.11) reacts with another NO_2 molecule in reaction (6.12). Thus, reactions (6.11) and (6.12) consume two NO_2 molecules overall. It is assumed that the only reaction for NO_2 to form NO_3 is reaction (6.11). One may therefore write

$$\frac{d[NO_2]}{dt} = -2k_{11}[O_3][NO_2] \quad . \qquad (6.14)$$

Eq. (6.14) may be integrated to determine the changing nighttime concentration of NO_2 at a particular level:

$$[NO_2]_f = [NO_2]_i \exp(-2k_{11}[O_3]\,dt) \qquad (6.15)$$

where $[NO_2]_f$ is the final concentration and $[NO_2]_i$ is the initial concentration of nitrogen dioxide, $[O_3]$ is the ozone concentration, and dt is the integration time. It is assumed that the ozone concentration remains unchanged during reaction (6.11), which is justified since the ozone concentration at 25 km is 3 orders of magnitude greater than that of NO_2. This simple expression for the overnight decay of NO_2 has been confirmed by *in situ* measurements by *Webster et al.* [1990]. It can be assumed that the nighttime increase at each level in N_2O_5, $\Delta(N_2O_5) = (NO_{2\ pm} - NO_{2\ am})$. The ratio of sunrise NO_2 (corresponding to $[NO_2]_f$) to sunset NO_2 ($[NO_2]_i$) for a particular level is

$$\frac{NO_{2_{am}}}{NO_{2_{pm}}} = \exp(-2\,k_{11}\,[O_3]\,dt) \quad . \qquad (6.16)$$

This relationship assumes only gas phase chemistry, with no thermal decomposition of N_2O_5, or transport of odd nitrogen. It also assumes there is no other reaction possible for the production of NO_3 molecules other than reaction (6.11).

Chemistry of HNO_3

The end product of odd nitrogen oxidation is nitric acid, HNO_3, the most stable and resistant to photolysis of all the odd nitrogen species. Nitric acid and N_2O_5 constitute the polar winter nitrogen reservoir which does not react with ozone. Nitric acid is formed and destroyed by the following gas phase reactions

$$NO_2 + OH + M \rightarrow HNO_3 + M \qquad (6.17)$$

$$HNO_3 + h\nu \rightarrow NO_3 + OH \quad (\lambda < 330\ nm) \qquad (6.18)$$

$$HNO_3 + OH \rightarrow H_2O + NO_3\ . \qquad (6.19)$$

The lifetime of HNO_3 , τ_{HNO3}, in the winter polar stratosphere may be estimated by taking the reciprocal of the photolysis rate of nitric acid, J_{HNO3}. At 90 mbar (about 17 km), for a constant solar zenith angle of 80°, J_{HNO3} is 7 x 10^{-8} s^{-1} [*A. Kylling*, personal communication, 1993] which gives τ_{HNO3} of over 100 days. At higher altitudes, photolysis of nitric acid is not shielded by ozone absorption and J_{HNO3} is larger; at 27 km, for a constant solar zenith angle of 80°, the lifetime is only 20 days. Nitric acid will resist photolysis at altitudes less than 25 km. For a solar zenith angle of 60° at 17 km, not reached until March 21, J_{HNO3} increases to about 2 x

10^{-6} s^{-1}, yielding a lifetime of about 10 days. Because of the large solar zenith angles of the winter high latitude, stratosphere OH is scarce, so reactions (6.17) and (6.19) can be neglected in the lower levels of the stratosphere. This is because OH is primarily formed by the oxidation of H_2O by $O(^1D)$

$$H_2O + O(^1D) \rightarrow 2OH \ . \qquad (6.20)$$

$O(^1D)$ requires ultraviolet radiation of $\lambda < 310$ nm which in the high latitude winter stratosphere is effectively blocked by the ozone above

$$O_3 + h\nu \rightarrow O(^1D) + O_2 \qquad (\lambda < 310\,nm) \ . \qquad (6.21)$$

Above the ozone layer (higher than 25 km) OH abundances are larger because the abundance of $O(^1D)$ is enhanced. Thus, at lower altitudes in the high latitude winter stratosphere HNO_3 has no major gas phase or photochemical sources or sinks, but above 25 km, photolysis and reaction with OH must be accounted for.

Next, consider the possible heterogeneous reactions on the surfaces of water and sulfate aerosols reaction (6.1) and the less probable (6.2). These lead to a shift in the NO_y partitioning towards HNO_3, resulting in less NO_2. This allows the ClO concentration to increase, making possible the chlorine catalytic cycles (reactions 1.22-1.26). Furthermore, the shift of NO_y from NO and NO_2 towards HNO_3

alters the hydrogen and chlorine oxide partitioning to favor catalytic ozone destroying reactions [*Toumi*, 1993].

The influence of transport

Not all the changes in species abundance are due to photochemistry or chemistry; some are due to advection. The time rate of change in abundance of a particular atmospheric species, n, is determined by the continuity equation

$$\frac{\partial n}{\partial t} + \nabla \bullet (n \cdot v) = P - nL \ . \qquad (6.22)$$

The second term on the left represents advection where v is velocity, n (cm^{-3}) is the concentration, L is the loss frequency (in units of s^{-1}), and P is the production rate (cm^{-3} s^{-1}). Production is limited to chemistry but loss terms may be either chemical or photochemical. There are three distinguishing cases relating the chemical lifetime, τ_{chem}, and the dynamical timescale, τ_{dyn} [*Solomon*, 1991]:

1) $\tau_{chem} << \tau_{dyn}$: the chemical lifetime is much shorter than the transport lifetime. This is the case for $O(^1D)$ in the stratosphere. In this case the influence of dynamics may be ignored.

2) $\tau_{chem} >> \tau_{dyn}$: the photochemical lifetime is so much longer than its dynamical lifetime that chemical effects can be ignored. This is the case for the gas phase reactions of

HNO_3 in the lower polar winter stratosphere. However, heterogeneous reactions can produce HNO_3 on timescales similar to dynamical lifetimes.

3) $\tau_{chem} \approx \tau_{dyn}$: the dynamical and chemical lifetimes are comparable. This case applies to N_2O_5, so the effects of both dynamics and chemistry must be considered.

NO_2 and N_2O_5 in the winter polar stratosphere have comparable chemical and dynamical lifetimes, so chemistry and transport are both important. It will be shown that some of the variations in measured NO_2 total column abundance are the result of horizontal transport due to planetary waves, and others the result of photochemistry.

6.2 Measurements of Column Abundance of NO_2: Seasonal Effects

To investigate the diurnal and seasonal behavior of NO_2 during the winter season 1992-1993, its slant column abundance was determined using the spectrograph described in Chapter 2. Slant column abundances were converted to total vertical column abundances by dividing by the air mass value of 16.7 appropriate for the measurement situation as described in Chapter IV. Figure 6.2 shows the time series of NO_2 vertical column abundances from November 10, 1992 through April 30, 1993. The total error in vertical column abundances in each measurement is estimated

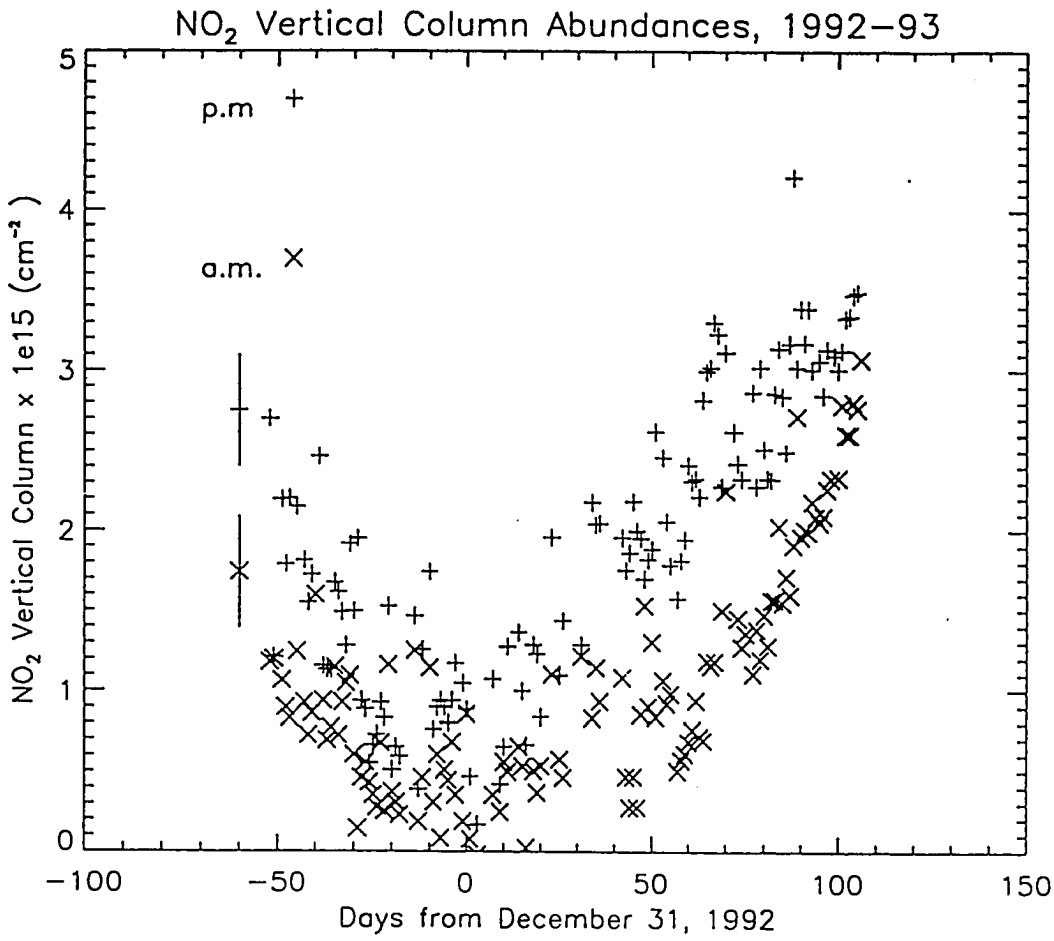

Figure 6.2: NO_2 a.m. and p.m. vertical column abundances for 1992–93. Shown are the a.m. (x) and p.m. (+) values. The error bar for daynumber −60 is shown which is typical for other days.

to be ± 20. The precision of the measurements is estimated at ± 10%. Days in 1992 are labeled on the graph as number of days before December 31. For instance, -50 corresponds to November 10, daynumbers (316 minus 366). Daynumbers from January 1 to April 30, 1993 are all positive, labeled as 1 to 120. The plus signs (+) represent 90° p.m. values and the x's (x) the 90° a.m. values. Measurements of total NO_2 slant column abundances were taken every 10 minutes near sunset and sunrise with integration times of 135 s. The times of sunrise and sunset were computed and the slant column abundance for 90° solar zenith angle determined by linear interpolation of the two measurements directly before and after 90°.

The original time series had several very large values which were assumed to be due to pollution. To eliminate the effects of tropospheric pollution, a quadratic curve was fitted to the time series (using MATLAB software) and subtracted from it. Outlying data points > ± 2σ about the resultant were rejected as being due to tropospheric pollution. Before these days were eliminated, the radiosonde temperature profile was checked to see if there was an inversion that day which would trap NO_x pollutants and cause large NO_2 values. In all cases, there were inversions to at least 900 mbar (1 km), and in some cases as high as 700 mbar (3 km).

The length of daylight has an obvious effect on the NO_2 column abundances. There is a decrease in both the NO_2 evening and morning column abundances from daynumber -61 (from December 31) until a minimum is reached around daynumber -6. This is consistent with the lengthening night which allows more N_2O_5 to accumulate due to less photolyzing sunlight during the short days. Daynumbers -10 through 20 show the lowest recorded column abundances, but several days have been rejected due to pollution. The average NO_2 column abundance during this period is about 1.0×10^{15} cm^{-2} for the p.m. and 0.5×10^{15} cm^{-2} for the a.m. measurements.

Measurements made in the southern Hemisphere show minimum austral fall p.m. NO_2 total column abundances of about 2.0×10^{15} cm^{-2} for daynumbers 110 to 120 (corresponding to daynumbers -72 to -62 in our study) measured at Halley Bay (78°S) in 1987 [*Solomon and Keys,* 1992]. At a latitude similar to Fairbanks (64° S) but later in the year towards austral spring for daynumbers 255 to 275 (corresponding to daynumbers 72 to 92 for our measurements), 1989, *Gil and Cacho* [1992] report p.m. NO_2 column abundances of between 2.0 and 3.0×10^{15} cm^{-2} and a.m. values between 1.5 and 2.5×10^{15} cm^{-2}. These compare with Fairbanks NO_2 column abundances of between 2.5 and 4.0×10^{15} cm^{-2} for p.m. values and 1.5 and 3.0×10^{15} cm^{-2} for a.m. values. Thus the Fairbanks NO_2 data shows a more rapid recovery of

column abundances in the spring compared with measurements of Gil and Cacho.

The Fairbanks a.m. and p.m. NO_2 column abundances both increase from daynumbers 30 to 120, which is consistent with the increasing duration of sunlight and smaller solar zenith angles. This increases photolysis of the storage reservoirs N_2O_5 and HNO_3 through reactions (6.13) and (6.17). Also, the decreasing length of night allows less time for the overnight decay of NO_2 into N_2O_5 through reactions (6.11) and (6.12).

6.3 Dynamical Effects on NO_2 Column Abundances

Superimposed on the parabolic shape of the NO_2 time series in Figure 6.2 are rather regular periodic variations in the amplitude. It can be shown that these variations are due to the transport of NO_2. Similar 3 to 5 day variations in the NO_2 time series of column abundances have been noted by *McKenzie and Johnston* [1984], *Mount et al.* [1987], and *Gil and Cacho* [1992]. *Noxon et al.* [1983] investigated large-scale horizontal advection of NO_2 in the polar winter by measuring its total column and using 10 mbar geopotential maps to chart upper air advection. He noted that the NO_2 column increased when the stratospheric flow was from the south, and decreased when the flow was from the north. He attributed this to different photochemical histories of the

air parcels: air from the south had been recently exposed to more sunlight resulting in increased photolysis of the storage reservoirs. Conversely, the air from the north had undergone less photolysis and contained less NO_2.

The temperature of the air parcel also affects NO_2 abundances by altering the NO/NO_2 partitioning through reaction (6.7). An increase in temperature from 200 to 230 K would decrease the ratio of NO/NO_2 inferred from Eq. (6.9) by more than a factor of two.

To investigate possible effects of horizontal transport, a Fourier Analysis was performed on the NO_2 time series. Using MATLAB software, a parabola was fitted to the data using a least squares fit; then this parabola was subtracted from the data. A Fourier transform was performed on the detrended data. The resulting power spectrum is shown in Figure 6.3. The power spectral density of p.m. slant column abundances shows a large maximum at 12 days. Rossby's Equation below allows calculation of the period of various wavenumber stratospheric planetary waves around the 65° latitude parallel. Stratospheric planetary waves are known to originate from tropospheric waves [*Andrews et al.*, 1987]. The phase velocity C of a planetary wave is given by [*Dutton*, 1986]

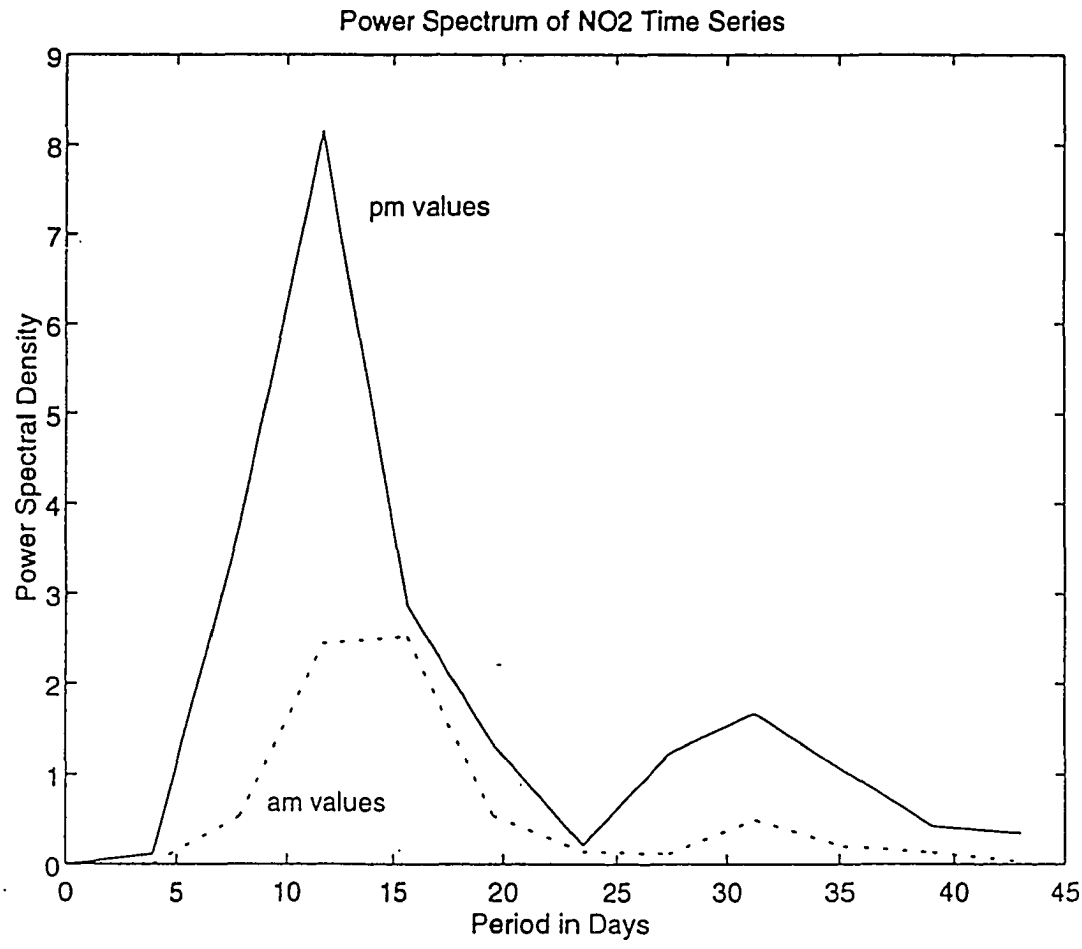

Figure 6.3: Power spectrum of NO_2 time series.

$$C = U - \frac{\beta L^2}{4\pi^2} \tag{6.23}$$

where U is the zonal mean of the wind velocity (westward component), L is the wavelength (equal to circumference of the earth divided by the wavenumber), β is the gradient of the Coriolis parameter f, df/dy, and y is the latitude.

The zonal wind U was found to be 20 m/s by averaging the westerly component of the 100 mbar wind vector for six days in March, 1993. Table 6.1 shows the phase velocities and periods for various wavenumbers. Negative phase velocities indicate waves traveling east to west. Wavenumbers 4 (a period of 12.5 days) and 5 (11.4 days) explain the periodicities fairly well. These wavenumbers correspond to fast-moving, short-lived tropospheric disturbances. In other words, these wavenumbers corresponds to synoptic scale disturbances.

There are many peaks in the NO_2 time series of Figure 6.2 due to planetary waves, reaching maxima at daynumbers 325 (-41), 338 (-28) and 348 (-18) in 1992. No clear wave structure is evident from daynumbers -10 1992 to 20 in 1993. The structure starts to reappear with clear maxima on daynumbers 37, 49, and 63. These maxima are roughly consistent with the 12 day periodicity determined by the Fourier Transform of the time series. It should be noted

that the zonal wind U was taken to be constant which is not strictly true. Using different values of U for each day would result in different periods computed from Eq. (6.21).

Table 6.1 Period of Various Stratospheric Planetary Waves

Wave Number	Phase speed (m/s)	Period (days)
1	-50	3.9
2	2.5	78.2
3	12.3	16.0
4	15.6	12.5
5	17.2	11.4
6	18.0	10.8

To further investigate the role of dynamics, 100 mbar temperatures (shown in Figure 6.4, top) and geopotential heights (shown in Figure 6.4, bottom) were obtained from the Fairbanks National Weather Service. There are periodic maxima in the 100 mbar temperatures and geopotenital heights; sometimes these two are correlated, and at other times uncorrelated. From daynumber 0 to 40, 1993, the temperatures and the geopotential heights show little correlation or are anticorrelated. This indicates baroclinic situations (surfaces of equal pressure do not coincide with surfaces of equal density) where cold air

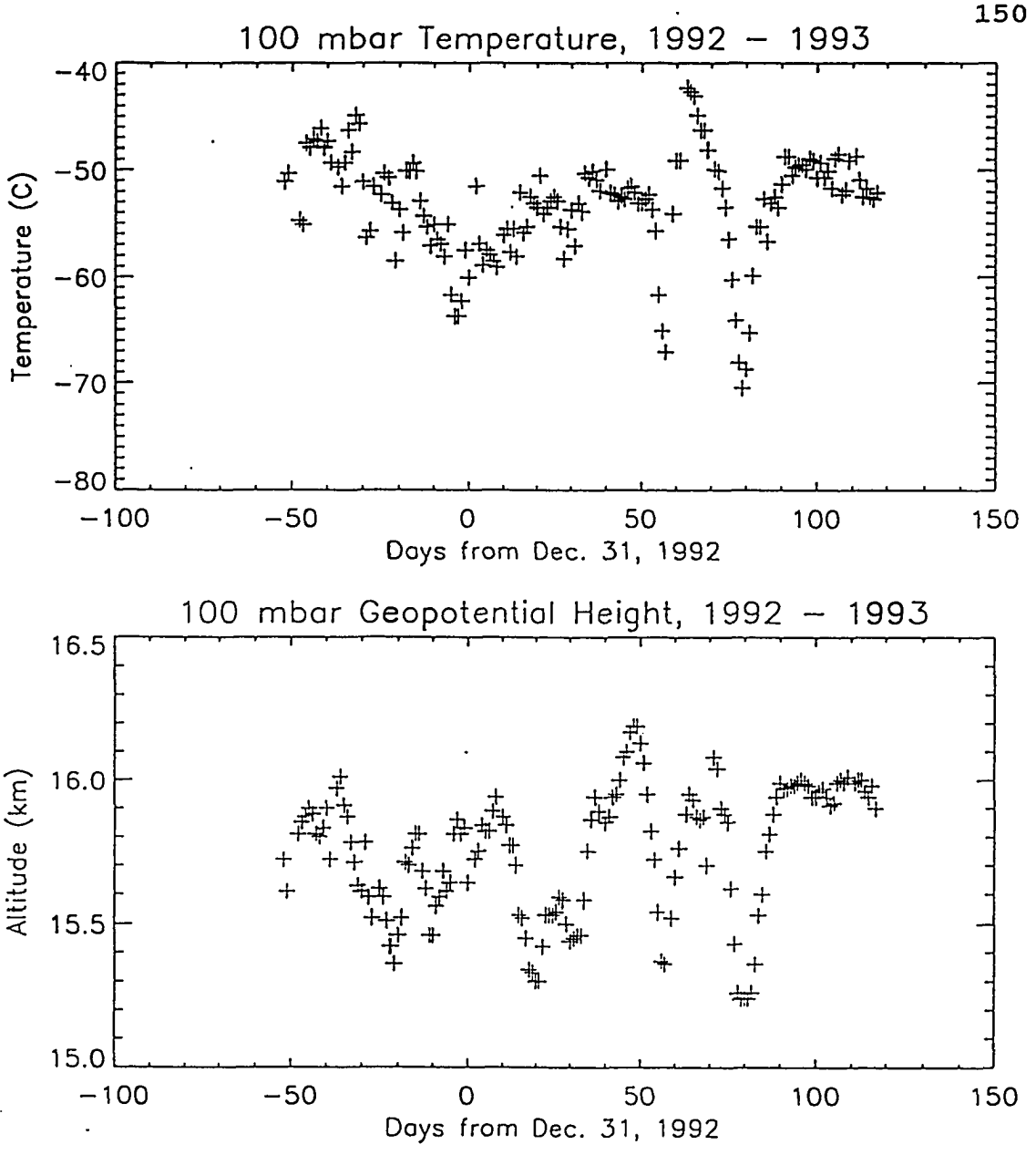

Figure 6.4: 100 mbar temperature (top) and 100 mbar geopotential height (bottom) measured by radiosondes sent up over Fairbanks.

overlies warm air and there is the potential for frontogenesis and advection. From daynumbers 40 to 120, temperature and geopotential are generally in phase, indicating equivalent barotropic (surfaces of equal pressure coincide with surfaces of equal density) conditions with less advection.

Some of these temperature and geopotential minima and maxima correlate well with NO_2 total column abundances, for instance on daynumber 63 when the NO_2, temperature and geopotential height all show maxima. This can be explained by an intrusion of stratospheric air from the south which has been exposed to sunlight for longer periods of time than the air at 65°N. This southerly air is also warmer and less dense so the geopotential height of the 100 mbar pressure level is greater. On daynumber 80, the NO_2, temperature and geopotenital height are at a minimum reflecting a northerly flow of cold and dense air which has been in darkness for longer than the air over Fairbanks.

At other times the NO_2 column abundance is anticorrelated with the temperature and geopotential height, for instance daynumber 90 when NO_2 shows a minimum but the 100 mbar temperature and geopotential remain nearly constant. A possible explanation lies in two competing temperature-dependent reactions affecting NO_2 abundances. The temperature effect of reaction (6.10) drives more NO_2

towards NO_3 and N_2O_5 for warmer temperatures. Since NO_2 is only destroyed in reaction (6.10) during in the dark, this effect is more pronounced for periods of long darkness, and could not explain the anticorrelation seen for daynumber 90 when the period of darkness in the stratosphere is less than 12 hours. There is the opposing effect of reaction (6.7), which, for warmer temperatures, causes more NO to go to NO_2. This effect would be most pronounced for p.m. measurements in the spring when the longer days have allowed considerable NO to form. Therefore, the minimum in NO_2 column abundances on daynumber 90 is not explainable by temperature effects and remains a puzzle.

6.4: a.m. / p.m. Ratios of NO_2 Abundance

The ratio of morning to evening NO_2 column abundance reveals the fraction of NO_2 that has been transformed to N_2O_5 overnight. The measured morning to evening ratios of NO_2 column abundances are shown in Figure 6.5 (top) for 1992-93. There is considerable scatter in these points near the winter solstice reflecting the combined uncertainties of taking the ratio of two small numbers each with large relative uncertainties. Some of the data have been contaminated with tropospheric pollution and have been rejected.

These measured a.m. / p.m. ratios, shown in the top

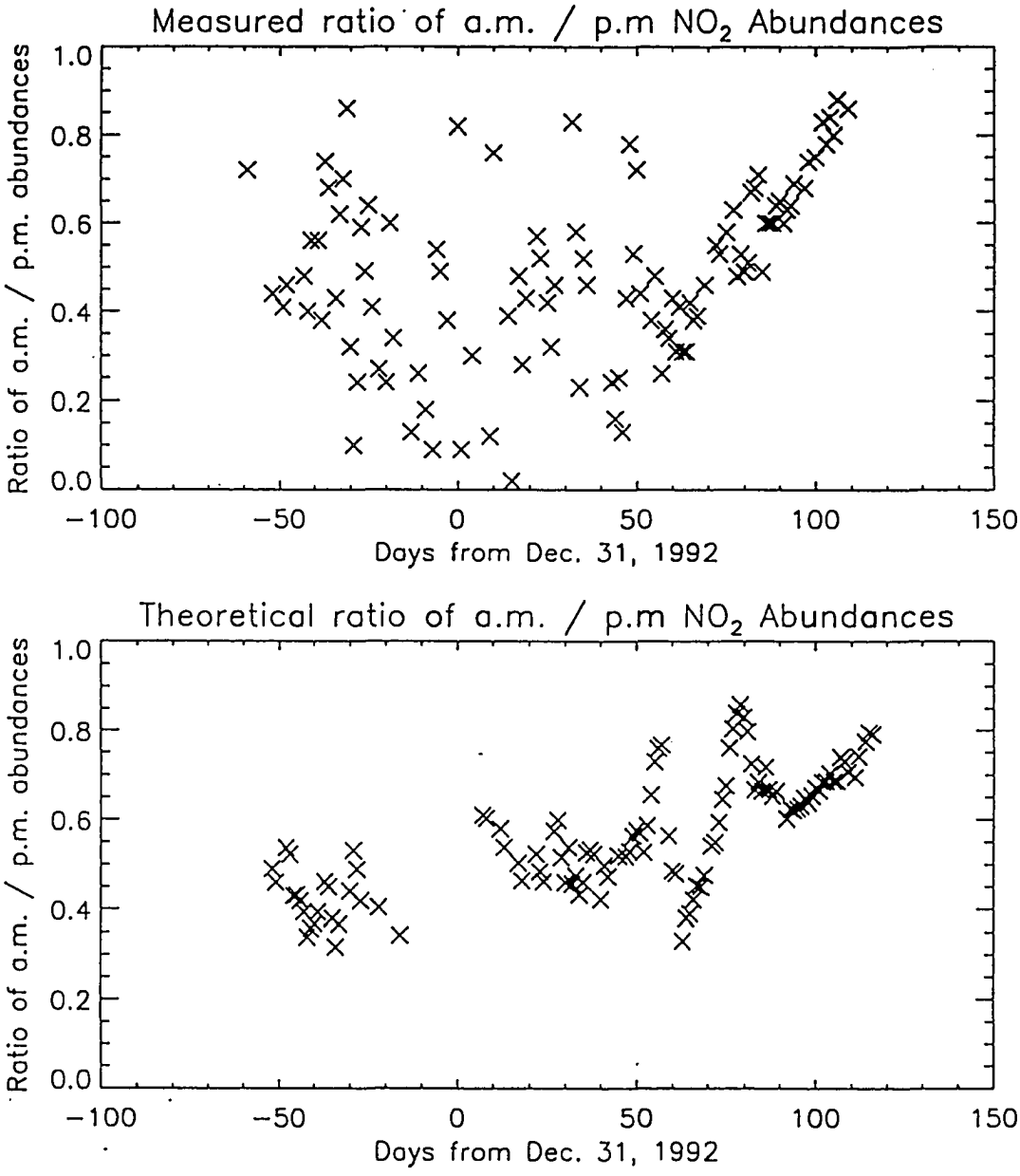

Figure 6.5: Ratio of a.m. / p.m. NO_2 column abundances. Measured (top) and theoretical (bottom) using temperature and ozone abundance at 27.5 km.

part of Figure 6.5, are compared to the theoretical estimate of morning to evening ratios calculated at 27.5 km using Eq. 6.14 (Figure 6.5, bottom). Before discussing these two plots, it is useful to describe how the information to compute the ratios using (6.14) was gathered.

The total ozone abundances measured by the Total Ozone Mapping Spectrometer (TOMS) satellite obtained from NASA are shown in Figure 6.6. To verify these ozone values, the TOMS total column abundances were compared with those measured by the Dobson spectrophotometer mounted on the roof of the Geophysical Institute. A comparison of 10 days of TOMS and Dobson ozone total column abundances from daynumbers 78 to 106, 1993, revealed an average difference of 1.6%, verifying the consistency of these two sets of data. Stratospheric temperatures were obtained from radiosondes launched at the Fairbanks Airport by the National Weather Service. Temperatures were collected at certain pressure levels: 100, 70, 50, 30 20, and 10 mbar corresponding roughly to 15.7, 18.2, 20.3, 23.8, 26.1, 30.1, 33.2, and 35.4 km respectively. The balloons typically broke at 30 or 20 mbar. To get a consistent measurement and to avoid missing data, the daily 100 mbar temperatures (an altitude of about 15.7 km) were scaled to 27.5 km using the Subarctic Winter Standard Atmosphere shown in Figure 6.7.

The average ozone profile was calculated by scaling the

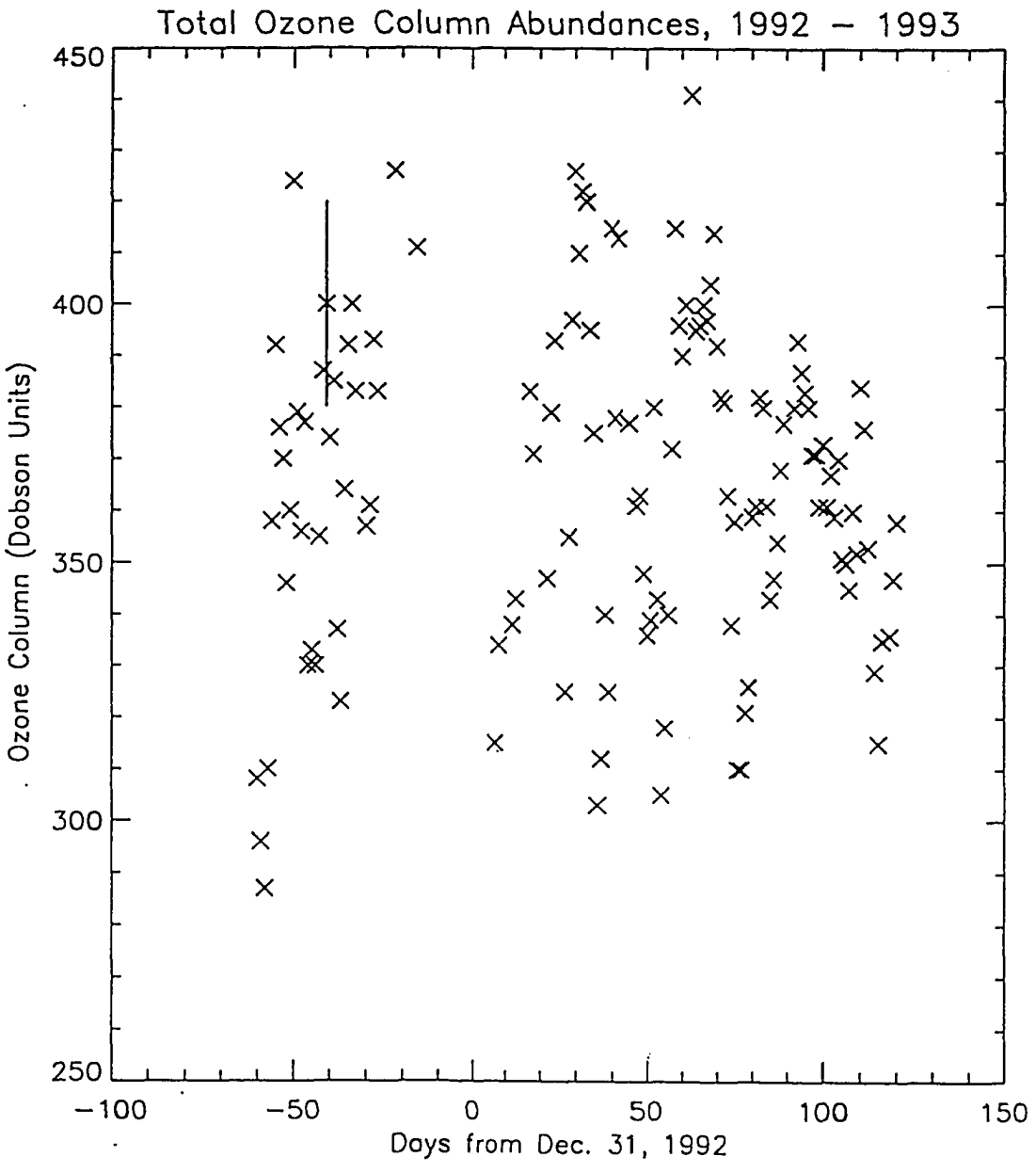

Figure 6.6: Ozone Column Abundances for 1992 – 93 as measured by the Total Ozone Mapping Spectrometer. The error bar for daynumber −41 is typical of the other data.

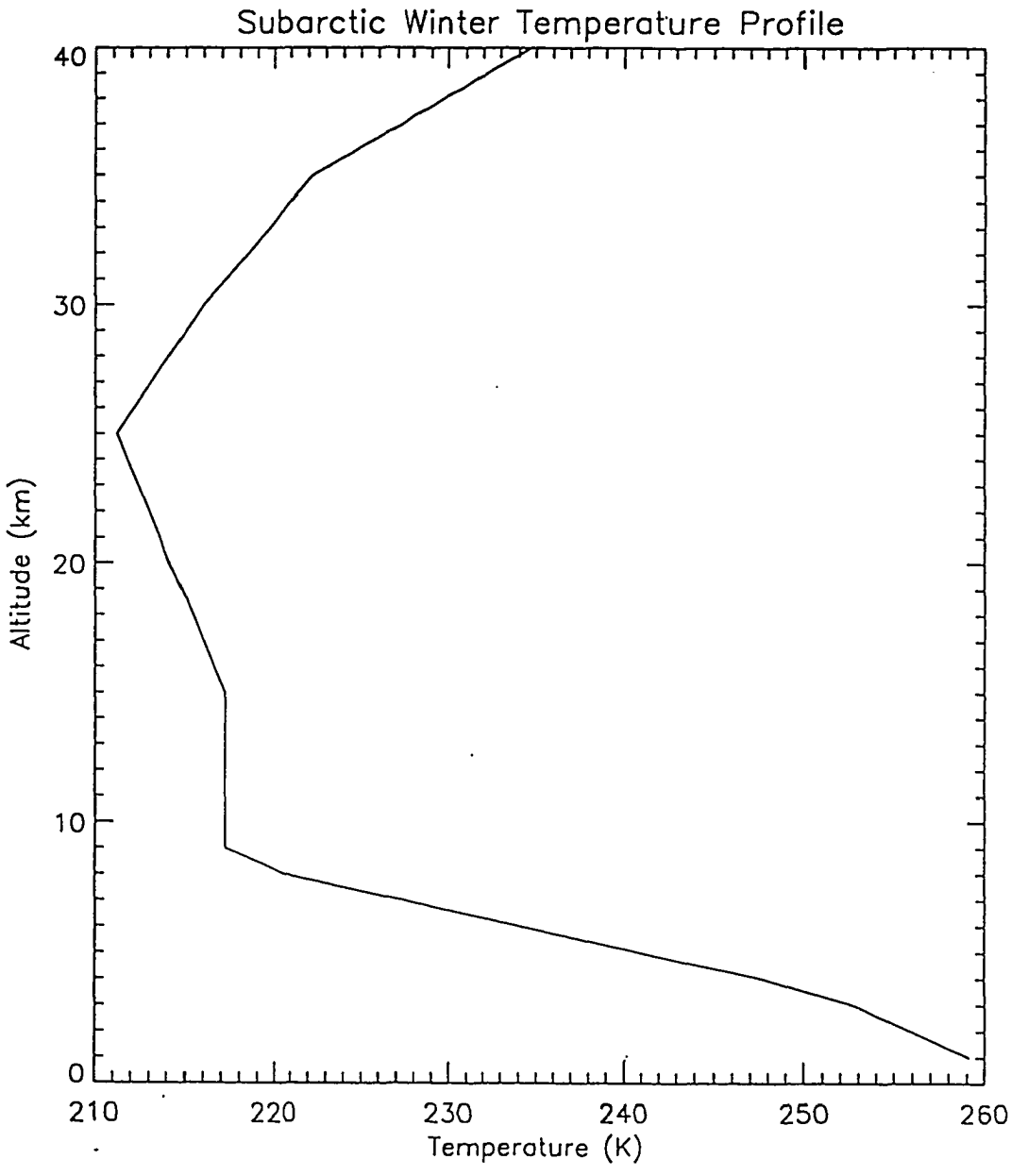

Figure 6.7: Subarctic winter temperature profile used to calculate the a.m. / p.m. theoretical ratios.

total ozone by the average profile determined from a series of 10 Umkehr measurements. The data were taken at Poker Flat, located about 50 km NE of Fairbanks, between September, 1990 and September, 1991 and were supplied by the National Oceanic Atmospheric Administration in Boulder. The 9 Umkehr levels have pressure coordinates which were converted to altitude using the ideal gas law and the Subarctic Winter Temperature profile. Figure 6.8 shows a typical ozone profile. To study the variability of the profile shape of the 10 measurements, the variation in fraction of total column in each layer was studied. Figure 6.9 (top) shows the percentage of the total ozone column of a layer versus total column for the lowest 4 Umkehr levels and (bottom) the same for the highest 5 levels. Although there is considerable variability in the lower levels, levels 5 and 6, centered at 23.2 and 28.1 km and close to the maximum NO_x concentration, are fairly constant. The standard deviation of layer 5 is 9.6% and layer 6 is 15.0%.

For one day the theoretical ratio of a.m. / p.m. NO_2 column abundances was calculated for a seven layer atmosphere from 10 to 45 km using the formula

$$\frac{NO_{2_{am}}}{NO_{2_{pm}}} = \frac{\sum_{j=1}^{7} \left(\frac{NO_{2_{am}}}{NO_{2_{pm}}}\right)_j [NO_2]_j}{\sum_{j=1}^{7} [NO_2]_j} \qquad (6.24)$$

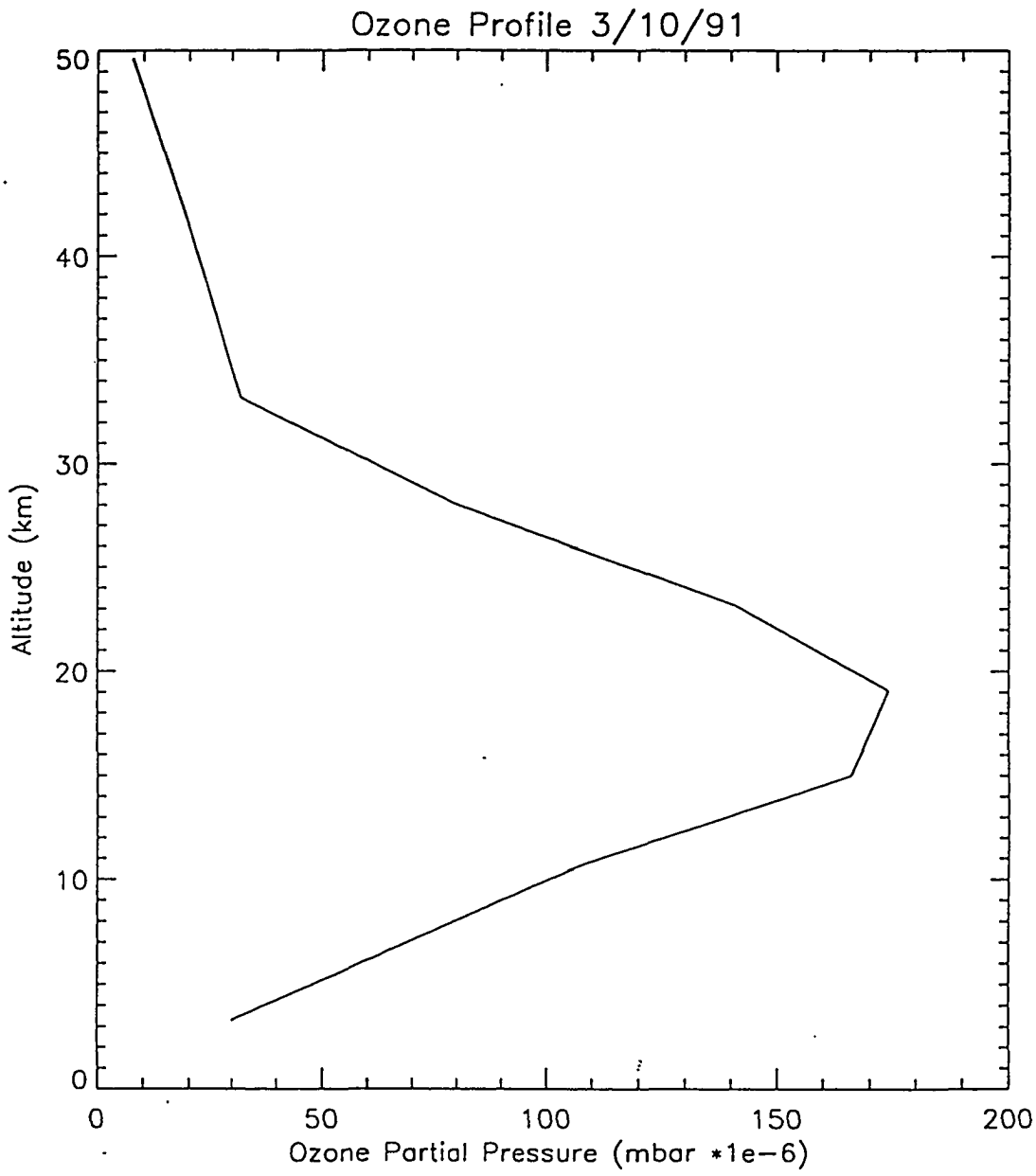

Figure 6.8: Ozone profile over Poker Flat on 3/10/91 retrieved from Dobson spectrophotometer data using Umkehr technique.

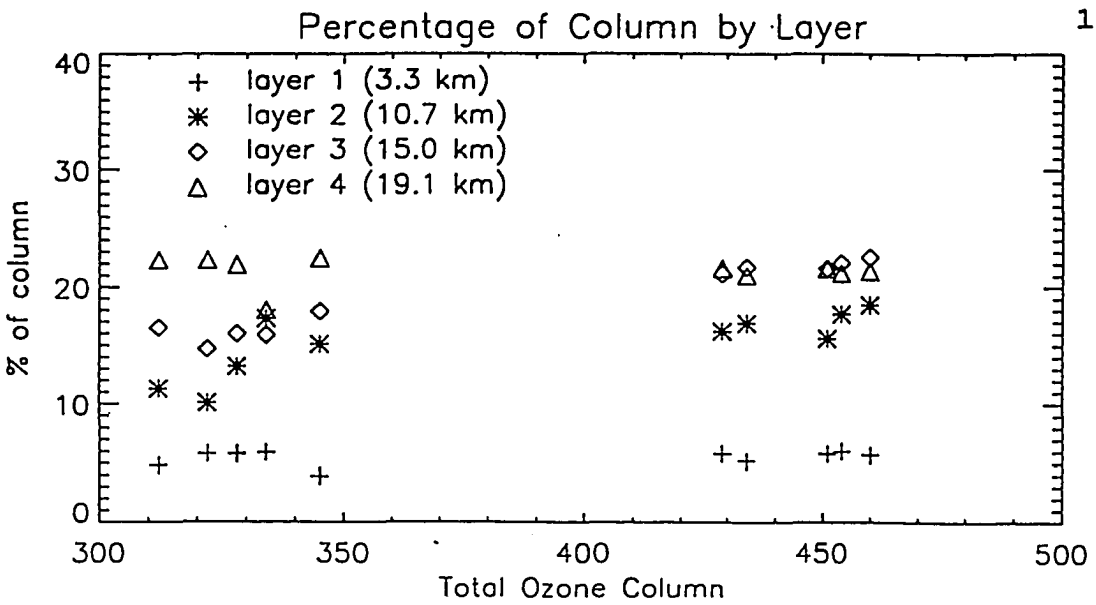

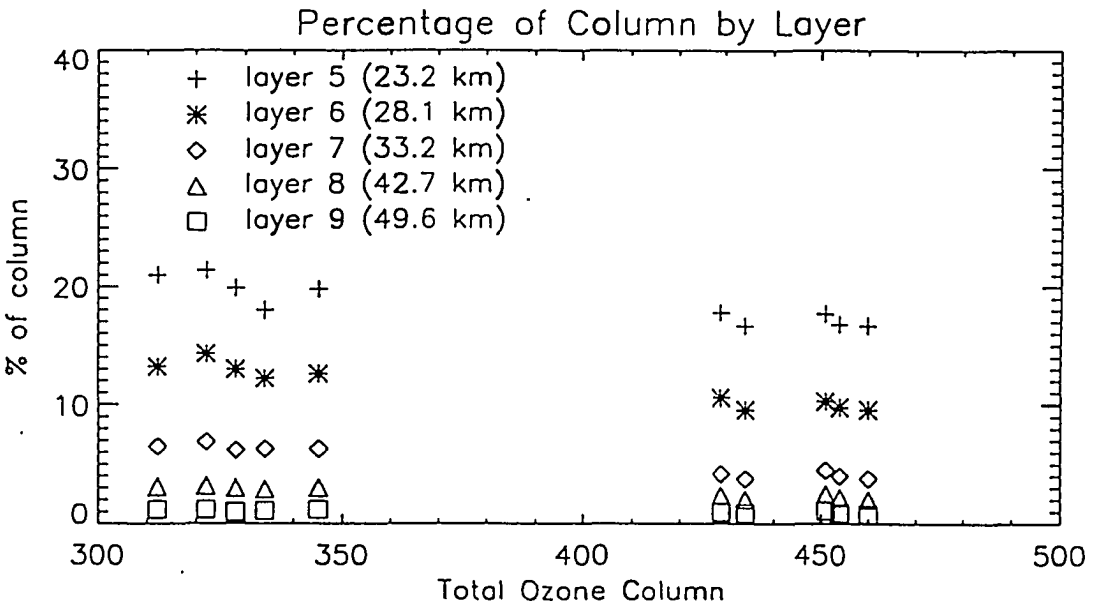

Figure 6.9: Variability of percentage of ozone in each Umkehr level versus total ozone column. Levels 1 – 4 (top) and levels levels 5 – 9 (bottom).

where j is the layer number, from 10 to 15 km (j=1) to 40 to 45 km (j=7). This was compared with the simpler calculation using Eq. (6.16) at an altitude of 27.5 km. The fraction of ozone in each of the nine Umkehr levels was multiplied by the daily TOMS total column abundance to yield the partial ozone profile. The length of night was calculated for each level by determining the duration for which the solar zenith angle was greater than the angle corresponding to the onset of darkness at that level. The NO_2 profile was constructed by taking the vertical profile retrieved from a p.m. NO_2 time series taken on March 14, 1993, and then scaling the 90° vertical column abundance. The difference between the two methods is 0.3%, justifying the simpler approach. However this close agreement using the one level and the nine levels is fortuitous. Even modest fluctuations in the actual temperature from those used from the Standard Atmosphere profile used will alter the ratio in Eq. 6.24. It will be seen that there are much greater uncertainties in the ratio due to extrapolating the temperatures than in using only one level for the ratio calculation.

What follows is a discussion of the measured and theoretical a.m. / p.m. ratios. The missing days for the theoretical ratios between daynumbers -15 and 10 result because no TOMS ozone data are available. The theoretical ratios shown in Figure 6.5 (bottom) are to be compared to

the measured ratios shown in Figure 6.5 (top). The theoretical and measured ratios do not agree well from daynumbers -50 to 0. The agreement improves as the time series nears its end. It is seen that in late 1992 and early 1993 there is considerably more scatter in the measured ratios than in 1993 after daynumber 40. The differences between the measured and the theoretical ratios could be due to errors in the temperature, NO_2, or ozone profiles used to calculate the theoretical ratios, or inaccuracies in the NO_2 measurements themselves.

The amount of NO_2 that decays at night is strongly affected by temperature. Figure 6.10 shows the computed temperature dependence of the (a.m. / p.m.) ratio at 27.5 km obtained by keeping ozone concentration and length of night the same. Inaccurate ozone and NO_2 profiles also will affect the ratios. For instance, too high a maximum in the NO_2 profile results in an (a.m. / p.m.) ratio that is too large because more NO_2 is at higher levels where the night is shorter. This prevents formation of NO_3. Too much ozone at higher levels results in the ratio being too small because a larger fraction of NO_2 will decay due to the additional ozone where the bulk of NO_2 is located. Of these three effects, the largest is due to uncertainty in the temperature. To investigate these issues further various parameters are changed in the theoretical ratio calculation

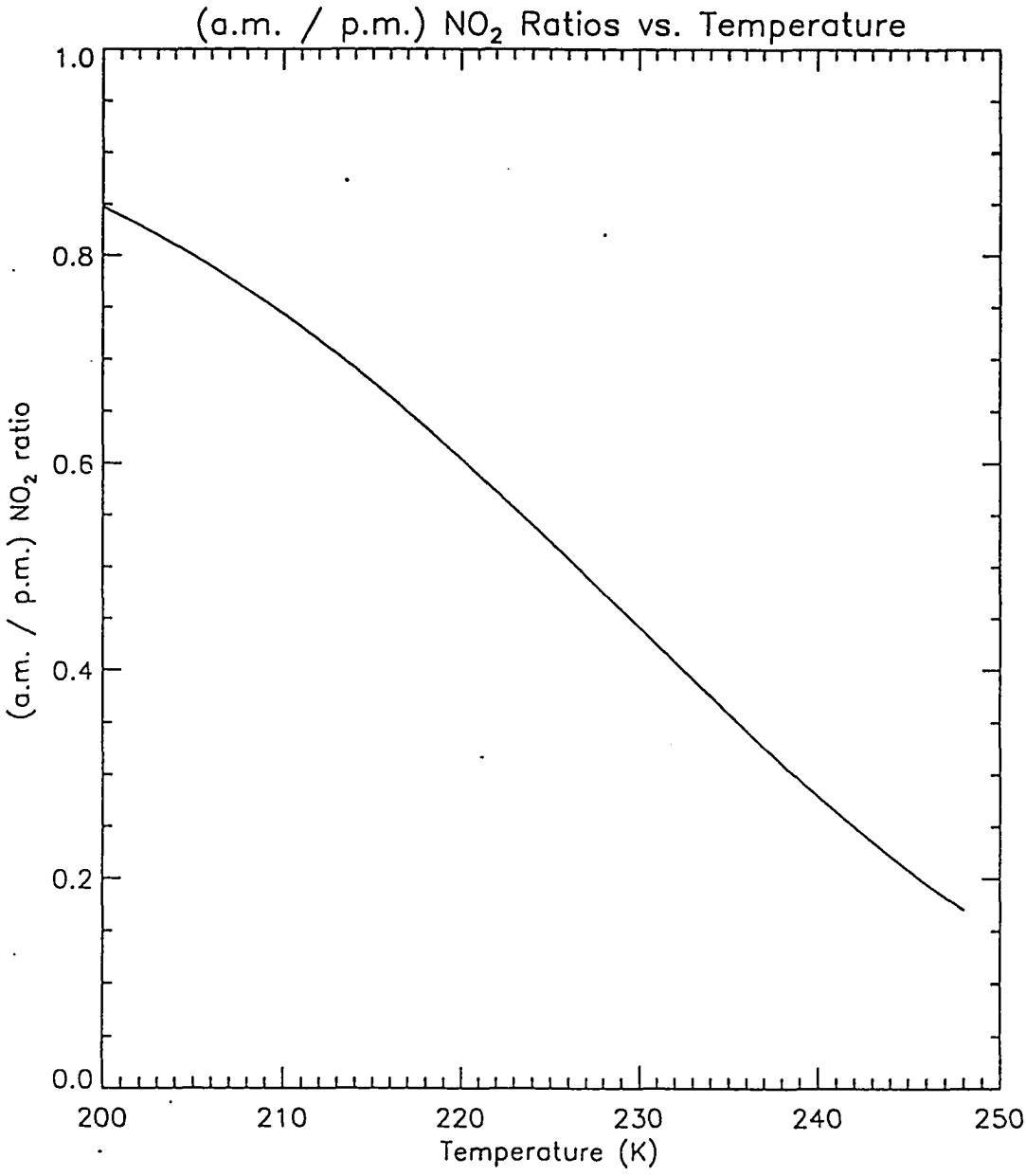

Figure 6.10: Temperature dependence of (a.m. / p.m.) NO_2 ratio keeping ozone concentration and length of night constant. Calculation was made for an altitude of 27.5 km.

at a height of 27.5 km: temperature ± 10°, ozone concentration ± 10%, and K_1 ± 10 to determine the effect on the a.m. / p.m. ratios. The results are summarized in Table 6.2.

Table 6.2 Sensitivity of Ratio to Changes of Parameters

Changes	a.m. / p.m. ratio
original conditions	0.6076
T + 10 K	0.444
T - 10 K	0.750
$[O_3]$*1.1	0.581
$[O_3]$*0.9	0.641
k_1*1.1	0.581
k_1*0.9	0.641

6.5 Possible Heterogeneous Conversion of N_2O_5 into HNO_3 on Sulfate Aerosols

Next is an investigation of the possible heterogeneous conversion of N_2O_5 into HNO_3 on sulfate aerosols in reaction (6.1). *Austin et al.* [1986] first postulated that the polar winter reservoir species of nitrogen was primarily nitric acid; this was an effort to explain the low measured amount of NO_2 and high amounts of HNO_3. Austin et al. stated,

> Closer examination of the temporal and spatial distribution of the satellite observations, however, provides clearer indication that the observed discrepancies between the model and the observations

> are probably due a photochemical source of nitric acid in the high latitude winter. . .It remains possible that . . . the following process occurs:
>
> $N_2O_5(g)$ + aerosol -> $2HNO_3(g)$.

To investigate this question a series of measurements of HNO_3 total column abundance, lidar backscatter measurements to infer aerosol surface area at various altitudes, and NO_2 column abundance to infer N_2O_5 distribution were used. These allowed calculation of the reaction coefficient k_1 for N_2O_5 into HNO_3 (reaction 6.1):

$$k_1 = \frac{\gamma A v}{4} \tag{6.25}$$

where A is the aerosol surface area ($\mu m^2/cm^3$), γ is the sticking coefficient which is the probability that a collision between N_2O_5 and a sulfate aerosol results in a reaction, and v is the mean velocity of N_2O_5 (m/s). A constant temperature of 217 K will be used to calculate v according to

$$v = \sqrt{\frac{8kT}{\pi m}} \tag{6.26}$$

where k is Boltzmann's constant, T is the temperature (K), and m is the mass of the N_2O_5 molecule.

The University of Denver [*Murcray et al.*, 1990] made measurements of HNO_3 and HCl total column abundances between August 1992 and February 1993 using a Bomen 0.2 wavenumber

resolution FTIR. The results of these measurements are shown in Figure 6.11. A substantial increase in HNO_3 column abundance is noted between August 13 - 20 (-140 to -133 from December 31) to the 3 measurements taken in October 30 - November 1 (-62 to -60). The average of the August readings is 1.6 x 10^{16} cm^{-2} and for the early November data is 2.0 x 10^{16} cm^{-2}. No data were taken during December and January. A series of 5 measurements taken between February 17 - 21 (48 to 52) reveal an average of 2.0 x 10^{16} cm^{-2}. There is no difference between the November and February HNO_3 column abundances. Yet, it is just during this period that N_2O_5 concentration should reach its maximum in the long polar winter nights through reaction (6.11). If there is sufficient sulfate aerosol, HNO_3 will form through reaction (6.1). It will be attempted to reconcile this lack of measured increase in HNO_3 with the possible production of HNO_3 on sulfate aerosols.

Reihs et al. [1990] studied the uptake of nitric acid on various mixtures of sulfuric acid and water at temperatures from 188 to 240 K and concluded that nitric acid ends up almost entirely in the gas phase because of its low solubility in the solution. A more recent study by *Zhang et al.* [1993] confirms this. Conversion of N_2O_5 into HNO_3 on sulfate aerosols results in the release of gaseous nitric acid.

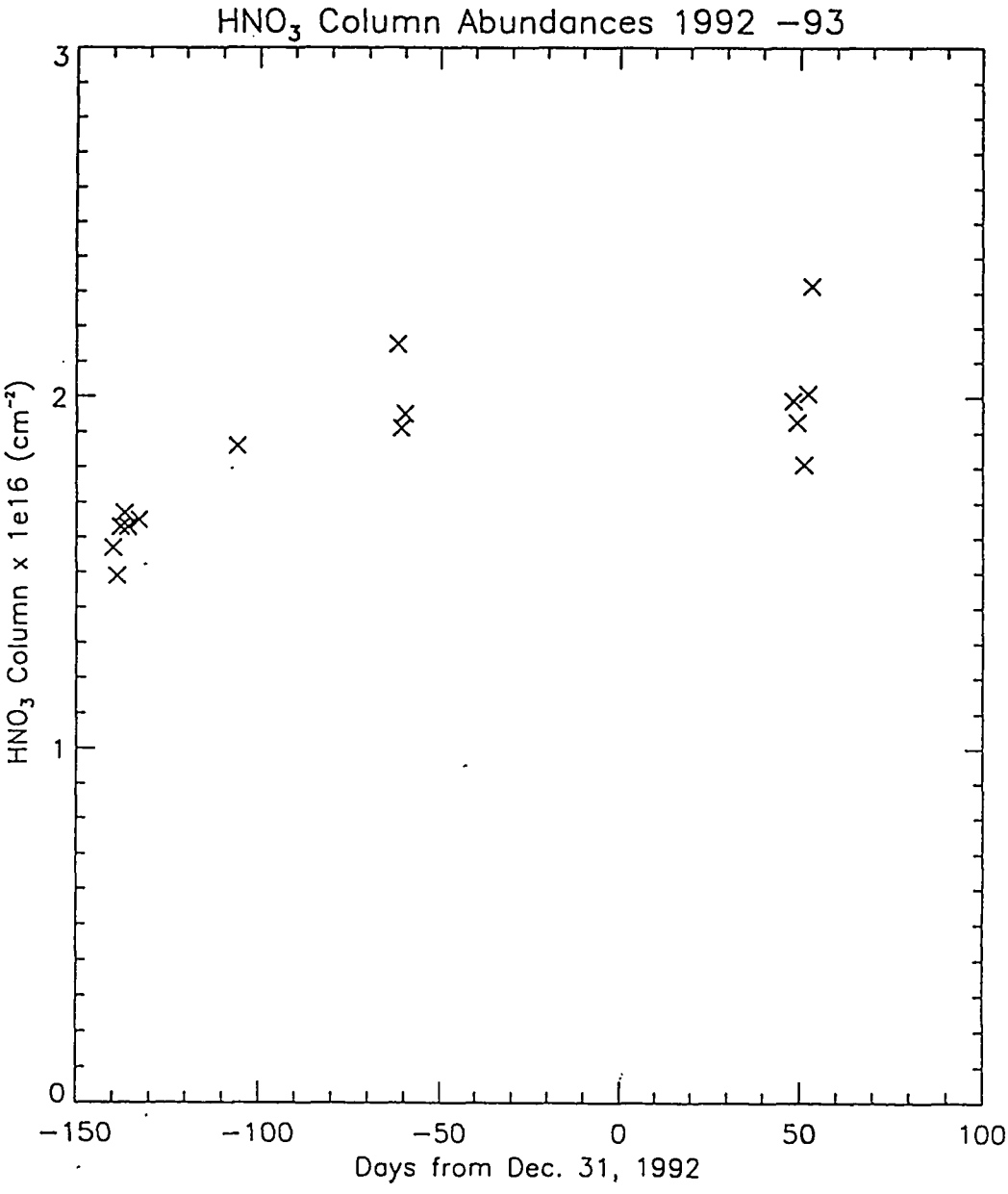

Figure 6.11: University of Denver FTIR total column measurements of HNO_3, 1992 – 93.

Estimating the aerosol surface area

To determine the stratospheric aerosol surface area, lidar backscatter measurements supplied by *Dr. T. Shibata* [personal communication, 1993] of Nagoya University, Japan were analyzed. Shibata used a 532 nm pulsed Nd:YAG laser [*Fujiwara et al.,* 1989] to measure the backscatter ratio profile during February and March 1993 above Poker Flat. If the depolarization ratio is near zero, it can be assumed that the particles are spherical. At typical stratospheric temperatures and pressures, only sulfuric acid mixed with water has a low enough vapor pressure to remain a liquid and be spherical. The measured depolarization was indeed close to zero, indicating an aerosol layer composed of a mixture of sulfuric acid and water. The scattering ratio, R, was measured, which is the ratio of total backscattering (the sum of Rayleigh, β_{Rl}, plus aerosol backscatter, β_{ar}, to the expected Rayleigh backscatter

$$R = \frac{\beta_{Rl} + \beta_{ar}}{\beta_{Rl}} \quad . \tag{6.24}$$

The quantity of interest is the aerosol backscatter coefficient β_{ar}

$$\beta_{ar} = (R-1)\cdot\beta_{Rl} \quad . \tag{6.25}$$

Figure 6.12 is a plot of altitude vs. scattering ratio R for a lidar measurement taken the night of March 15, 1993. These R values were averaged in altitude ranges of 5 km centered at 17.5, 22.5, and 27.5 km, for four days of lidar measurements (February 13, March 13, 15, and 16, 1993). The lidar measurements were normalized at 33 km assuming only Rayleigh scattering, using a standard atmosphere to determine the molecular density. Values for β_{R1} at other altitudes were calculated by multiplying the molecular density of air (m^{-3}) at that particular altitude by the backscatter coefficient for one molecule which is 6.3×10^{-32} m^2/steradian for the system. At 15 km, this results in $\beta_{R1} = 1.8 \times 10^7$ (m steradian)$^{-1}$. β_{R1} can be scaled to other altitudes by the pressure, since Rayleigh scattering is proportional to the molecular density. To estimate the errors in β_{ar}, one can look at the statistical error, $n^{0.5}$, where n is the total number of counts recorded in a layer. Alternately one takes the standard deviation about the mean within a layer. For instance, in Figure 6.12, the $n^{0.5}$ error for β^{ar} for the layer 25 - 30 km is 9%, yet the standard deviation (s. d.) is nearly 100%. Because the large scatter in these points can not be true stratospheric aerosol structure, it was decided to adopt the more conservative of the two errors. For the layer 20-25 km, the s.d. error is about 50%, and for 15-20 km about 25%.

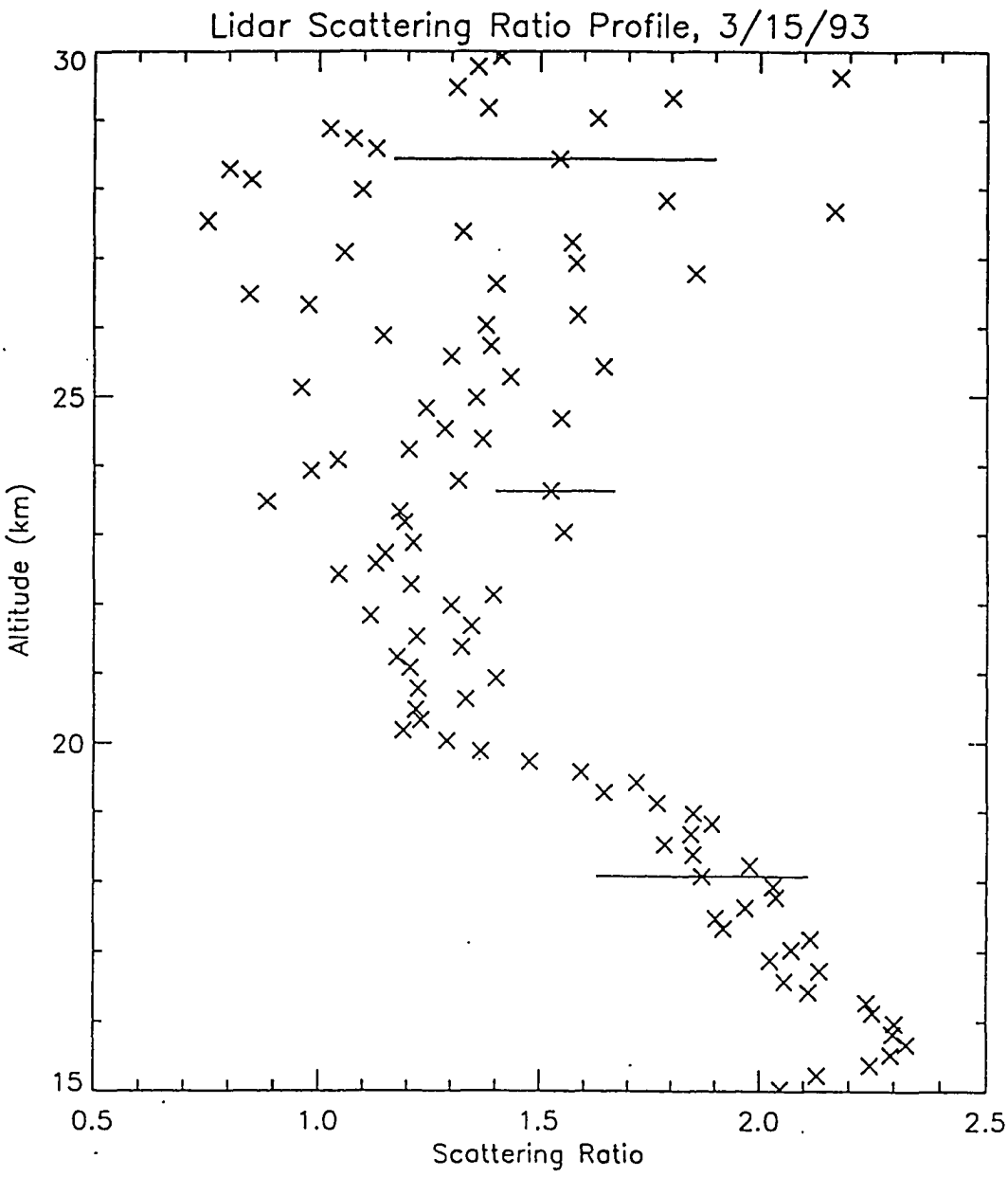

Figure 6.12: Scattering ratio profile measured over Poker Flat on 3/15/93. Data was supplied by Nagoya University. A scattering ratio of greater than one indicates a backscatter from something other than molecules. Error bars indicating the standard deviation are included for data points at three altitudes.

Once the aerosol backscatter coefficient was obtained, it was necessary to convert this into a surface area. *Jäger and Hofmann* [1991] did a detailed comparison between ten years lidar measurements made in the Federal Republic of Germany and *in situ* balloon sampling measurements made at the University of Wyoming. This study allowed the conversion of aerosol backscatter ratios to total aerosol surface area. The conversion factor is dependent on the altitude of the aerosol and year of the measurement. The years 1983-84 were chosen for conversion factors because the 2 to 3 year period after the 1982 El Chichon eruption is similar to the time between the 1991 Pinatubo eruption and Shibata's measurements.

The probability that N_2O_5 will react with water once it collides with the aerosol is given by the sticking coefficient, γ. For reaction (6.1), it has been measured in the laboratory by *Hanson and Ravishankara* [1991] at temperatures from 224 to 227 K with a percentage weight of sulfuric acid from 40% to 75%, respectively, in aqueous solution. The rest of the acid fraction was water. Values of γ ranged from 0.14 to 0.10. A value of 0.10 was adopted for this work, which represents the sticking coefficient for 70 to 75 % sulfuric acid at 220 K. The percentage of sulfuric acid in a particular stratospheric aerosol depends upon the water vapor available in the atmosphere, that is,

upon the relative humidity at that pressure and temperature. A 75% H_2SO_4 25% H_2O particle is in equilibrium with water vapor at typical stratospheric conditions of a water vapor mixing ratio of 3.0 ppmv at 220 K [*Hamill et al.*, 1988].

Measurements made aboard the ER-2 [*Wilson et al.*, 1993] at an altitude of 20 km gave an average stratospheric water vapor mixing ratio of 5 ppmv over the Arctic meaning more water available and hence less percentage weight sulfuric acid than the "typical" aerosol above. *K. Kelly* [private communication, 1993] measured a water vapor mixing ratio of about 4 ppmv over Fairbanks at an altitude of 20 km in October 1991. A 40% sulfuric acid / 60% water aerosol has a sticking coefficient of 0.14 [*Hanson and Ravishankara*, 1991]. The reaction probabilities for $ClONO_2$ on the same mixtures and temperatures were measured to be much smaller, between 1.9×10^{-4} to 6.4×10^{-2}. For this reason, reaction (6.2) will be ignored. One may calculate the reaction coefficient k_1 for the 5 km layers centered at 17.5, 22.5, and 27.5 km. It should be noted that the values of k_1 for the 22.5 and in particular the 27.5 km layers have large uncertainties owing to the small signal-to-noise of the lidar returns at these levels.

Production of HNO_3

Once k_1 is known, the production rate of HNO_3 from

reaction (6.1) may be estimated given a profile of N_2O_5 concentration. It is difficult to measure the abundance of the N_2O_5 molecule directly because its infrared rotational and vibrational absorption bands are broad, weak, and obscured by other stronger absorbers [*Roscoe,* 1991]. However, using the solar occultation method, a profile has been measured from a balloon-borne Fourier Transform Infrared Spectrometer (FTIR) down to 25.5 km [*Camy-Peyret et al.,* 1993]. It was assumed that the N_2O_5 profile has the same shape as the NO_2 profile retrieved from a time series of NO_2 slant column abundances measured on March 15, 1993 so the N_2O_5 curve was scaled down to 17.5 km. This is reasonable because N_2O_5 is formed in reactions (6.10) and (6.11) from NO_2 and ozone. The approximate total column abundance of the Camy-Peyret measurement extrapolated down to 17.5 km was 1.0×10^{15} cm^{-2}. The shape of this profile will be used to construct a N_2O_5 profile from the column abundance of N_2O_5 that is about to be deduced.

The N_2O_5 total column abundance can be roughly estimated by noting the seasonal decay of NO_2, and equating this decrease in NO_2 to an increase in N_2O_5 through reaction (6.11), that is $\Delta NO_2 = -0.5\ \Delta N_2O_5$. Referring to Figure 6.2, the NO_2 column at daynumber -50 is about 2.5×10^{15} cm^{-2} and near solstice daynumber -10 is about 1.0×10^{15} cm^{-2}. This gives an N_2O_5 column abundance of 0.75×10^{15} cm^{-2} at

solstice. As the days lengthen, the N_2O_5 is expected to decrease. By February 20, the NO_2 column has increased to about 2.0×10^{15} cm^{-2}, meaning the N_2O_5 column is estimated to be about 0.4×10^{15} cm^{-2}.

Converting the estimated solstice N_2O_5 column abundance of 0.75×10^{15} cm^{-2} to a profile using the Camy-Peyret data yields a three layer profile from 15 to 30 km. Multiplying each layer's concentration of N_2O_5 by k_1 gives the production rate of HNO_3 at solstice as shown in Table 6.3. Also shown is the average of aerosol surface area over the 5 km altitude layers as inferred from the lidar backscatter measurements. Over the three 5 km layers of atmosphere being considered, this results in a total HNO_3 production rate at solstice of 5.9×10^{14} cm^{-2} day^{-1}, or about 3% day^{-1} of the total column. For February 20, when the inferred N_2O_5 column is about half the solstice value, the HNO_3 production rate is about 1.5% of the total column per day.

Table 6.3: Solstice Production Rate of HNO_3 assuming a N_2O_5 column of 0.75 x 10^{15} cm^{-2}

Z (km)	$[N_2O_5]$ (cm^{-3} x 10^8)	Aerosol A μm^2 / cm^3	$k[N_2O_5]$ (s^{-1} cm^{-3}) x 10^2	HNO_3 per layer (cm^{-2} d^{-1}) x 10^{13}
17.5	0.14	10.6 ± 2.6	7.2	6.3
22.5	2.6	1.93 ± 0.9	26	2
27.5	5.4	1.53 ± 1.5	41	36
total	--	--	--	59

Next, the sinks of HNO_3 for February 20 are investigated: it photolysis reaction (6.16) and its reaction with OH, (6.17). The percent of HNO_3 photolyzed per day on February 20 at 17, 22, and 27 km were computed using 1-hour time steps, and the appropriate J_{HNO3} for the solar zenith angle

$$[HNO_3] = [HNO_3]_o \exp(-\sum J_{HNO_3}(t)\Delta t) \quad . \qquad (6.26)$$

Although OH abundances will not be large in the lower winter polar stratosphere, an upper limit estimate of its concentration was estimated from the work of *Stimpfle et al.* [1990] who used the laser-induced fluorescence technique to measure its concentration between 23 and 36 km at 32° N. The solar zenith angle ranged from 51 to 61°. These are

upper limits because the solar radiation at the smaller solar zenith angle of the Stimpfle measurements produces more OH from reaction (6.18) than at the relatively large solar zenith angles of February 20 over Fairbanks. The concentration of OH, [OH], for 17.5 km was taken from a model of *Brasseur and Solomon* [1986] that used calculations for noon at equinox. The reaction coefficient of reaction (6.17) is pressure and temperature sensitive [*DeMore et al.*, 1990] and was calculated for the three levels, 17.5, 22.5, and 27.5 km. To estimate the loss rate of HNO_3 a steady state [OH] was assumed and the following equation integrated for 8 hours, the approximate length of day on February 20:

$$\Delta HNO_3 (cm^{-3}) = k_{17} \; [OH] \; [HNO_3] \, \Delta t \; . \qquad (6.27)$$

OH concentrations were assumed to fall to zero during periods of darkness.

The HNO_3 profile is required to determine what fraction of this gas lies in the various 5 km slabs. This profile was estimated using the work of *Goldman et al.* [1992] who measured the profile of HNO_3 from a balloon using an FTIR at 32° N at solar zenith angles ranging from 90 to 95°. The results of the sources and sinks are shown in Table 6.4.

Table 6.4: Sources and Sinks of HNO_3 by layer for February 20 assuming N_2O_5 column of 0.75 x 10^{15} cm $^{-2}$

z (km)	HNO_3 column x 10^{15} cm^2	HNO_3 production % per day	HNO_3 photolysis % per day	HNO_3 loss by OH % per day
15-20	3.68	1.7	0.2	0.3
20-25	6.22	3.5	0.6	0.5
25-30	4.48	8.0	2.4	3.2

Since these reactions on aerosol surfaces are expected to proceed continuously as soon as N_2O_5 has accumulated in the fall stratosphere, there is evidently too much HNO_3 being produced in this crude estimate. There was a net production of HNO_3 in each layer, yet no increase in the column abundance was observed by the FTIR measurements.

The assumptions made will be examined. Transport was not taken into account. Seasonal transport is expected to bring HNO_3 from the equator to the poles between the summer and the winter. It is for this reason that the ozone is at its maximum at the pole in the winter. If there were indeed transport bringing in more HNO_3, there should be an additional increase in HNO_3 besides that produced by the heterogeneous reactions. So invoking seasonal transport, which should normally increase the amount of HNO_3 during the winter, does not help to explain the data. The transport would have to be in the other direction. However transport

from local high latitudes deficient in HNO_3 (for instance from areas within the polar vortex where HNO_3 concentrations are low because of sedimentation of nitric acid trihydrate), could explain the lack of increase in HNO_3.

Other possible ways to resolve the observed lack of HNO_3 increase between November and February involve its apparent production on sulfate aerosols:

1) the sticking coefficient was too large. Adopting a sticking coefficient of less than 0.1 would bring the production of the excess HNO_3 into better agreement with the estimated loss rates.

2) The estimated aerosol surface area is too large. This could be because the backscatter ratio is too large, or β_{R1} is too large, or the conversion factor of Jäger and Hofmann is too large. One notes that the standard deviation in β_{ar} is ± 100 % for the layer from 25 to 30 km, and ±60% for the layer from 20 to 25 km. Using the lower limit yield surface aerosol surface areas (and HNO_3 production rates) that are in line with the sinks and result in no net production of this gas.

3) The temperature assumed for the N_2O_5 is too large. Even lowering the assumed temperature from 217 K to 190 K (which was never reached according to radiosonde measurements) fails to reduce the production rate of HNO_3 by more than 15%. This is also not sufficient to fit the data.

4) There was too much N_2O_5 put in the profile. Decreasing in half the N_2O_5 column of 0.4 x 10^{15} cm^{-2} nearly balances the production and loss rates of HNO_3. In fact, by February 20, the approximate N_2O_5 column is expected to be about this value. Even so, recall that the [OH] was an upper limit because the measurement was taken at far smaller solar zenith angles. To truly balance loss and production rates would require even less than the 0.4 x 10^{15} cm^{-2} estimated for this date.

Of all these factors, the least well known is the N_2O_5 profile. Its concentration has been estimated in a very crude way. It would be useful to have a method for determining the column abundance of this gas from the ground, but the interference from tropospheric water vapor prohibits this. However, its spectrum can be measured from a balloon-borne FTIR. A set of such measurements are necessary to answer whether reaction (6.1) is occurring. In addition, there are no HNO_3 measurements from December and January, the very months when the production of this gas should be at its maximum. These measurements would indicate whether its production is occurring when N_2O_5 abundance is at its maximum, the solar radiation is at its minimum, and the sinks from reactions (6.16) and (6.17) can be neglected.

Chapter 7

Summary and Conclusions

NO_2 is one of the most important stratospheric trace gases that influences ozone abundances. To determine its abundance, a semi-automated spectrograph system was developed for recording scattered light spectra. These spectra were analyzed using retrieval software supplied by researchers at National Institute for Water and Atmosphere (NIWA) to determine slant column abundances of NO_2. This system measured the evening slant column abundances of NO_2 to within an average of 9% of the NIWA spectrometer at the Network for Detection of Stratospheric Change Intercomparison held in Lauder New Zealand in 1992. The instrument has been in nearly continuous operation at Fairbanks since November, 1992.

A measure of the air mass is required to convert slant column abundances to vertical column abundances. Software to compute air mass was developed using a multiple scattering discrete ordinate radiative transfer code with corrections for spherical geometry. The twilight conversion between NO and NO_2 should be considered in air mass computations [*McKenzie et al.*, 1991]. Air mass computations using the discrete ordinate method were compared with those

of the Monte Carlo method [*Perliski*, 1992] and were found to agree to within 5% at 90° solar zenith angle for stratospheric absorbers. Agreement of air mass values for tropospheric absorbers is within 25% at 90°. Computations using the discrete ordinate method are about 40 times faster than those using the Monte Carlo method.

Air mass depends upon the vertical distribution of the absorber, making the absorber profile necessary to convert slant column abundances to vertical column abundances. The profile code supplied by *McKenzie et al.* [1991] was used to retrieve the NO_2 profile from several measured time series.

Daily measurements of the NO_2 slant column over Fairbanks were made during the winter 1992-93. The NO_2 vertical column abundances inferred from these measurements showed the expected seasonal decrease as the hours of daylight diminished, and an increase as the sunlit hours increased. The ratio of measured morning to evening slant column abundances of NO_2 was roughly consistent with predictions based on a simple gas phase estimation of the overnight decay of NO_2 into N_2O_5. Near the winter solstice, the ratios are not close to the predictions of this simple model, indicating tropospheric pollution. Periodic maxima in column abundances were shown to be due to the transport of NO_2 different latitudes.

To study the effects of the remnant of the Mt. Pinatubo

aerosol layer on the odd nitrogen budget, the extent of the possible reaction of N_2O_5 and water on sulfate aerosols to yield nitric acid vapor was investigated. Lidar data taken by Nagoya University at 15 to 30 km altitudes over Fairbanks were used to estimate the aerosol surface area. The N_2O_5 concentration was estimated from the seasonal decay of NO_2 and a simple model constructed to estimate the production rate of HNO_3. The estimated production rates of HNO_3 predict a measurable increase in HNO_3. No increase was observed from the measurements of HNO_3 column abundance made using an FTIR deployed at Fairbanks by the University of Denver. This points to errors in the amount of N_2O_5, or surface area of the aerosol, or sticking coefficient in Eq. (6.1). Using the aerosol surface area from measurements by *Shibata et al.* [1994] made over Japan results in an HNO_3 production that is about half as large as the one calculated. Transport of HNO_3 is another possible reason that no increase in this gas was observed. Since HNO_3 has a long lifetime in the winter stratosphere, dynamical effects will be important. It was shown that horizontal transport is important for NO_2 column abundances. It is possible that the HNO_3 that was produced was then advected away, and replaced by HNO_3 depleted air.

To improve the accuracy of the NO_2 retrievals, modifications of the spectrograph system should be

performed. These include cooling the detector to -35° C to reduce the dark charge. This can be accomplished by chilling the glycol that flows pasts the hot side of the Peltier Device to 0° C (see Appendix A). Since changes of temperature affect the dark current of the detector and change the optical path of the spectrograph, the entire spectrograph should be maintained at a constant temperature. Dark current should be determined before each measurement and subtracted. The spectrograph should be moved to a site where the effects of tropospheric pollution are minimized.

A better estimation of the errors in NO_2 retrievals is required. The residual errors are not random indicating problems with the temperature dependence of the NO_2 cross sections, Ring Effect, and grating polarization effects. One way to attack this problem of bias errors would be to make a stable NO_2 absorption cell and place it in front of the entrance slit of the spectrograph each noon and record the spectrum. Analysis of the residuals under a variety of sky conditions (various clouds, aerosols, solar zenith angles) would enable a determination of what portion of the residuals are due to atmospheric, instrumental, and software effects.

The air mass factor computations should be extended to include the effects of aerosol layers at different levels of the stratosphere. A simple photochemical model can be used

to investigate the effects of twilight NO/NO_2 chemistry on air mass. Using these different air masses will then generate different NO_2 profiles; sensitivity studies should be performed to study the differences in retrieved profiles.

To study the possible influence of heterogeneous reactions, a study of the combined influences of photochemistry and dynamics is required. Weekly measurements of HNO_3 and HCl using the FTIR, in conjunction with daily measurements of NO_2, can provide the necessary input to photochemical models. The diurnal and seasonal evolution of the NO_2, HNO_3, and HCl column, as well as the diurnal cycles of NO_2, should be modeled and compared with observations. Differences between measured values and model predictions could be investigated by including transport terms and possible heterogeneous reactions in the model.

Appendix A

Computer Interfacing

System Software and Control Electronics

The photodiode array detector will be described, including how photons of a particular wavelength are detected, and how the measurement is transmitted to the computer. Next, experiment control and data storage with a computer are investigated. Finally, the steps taken to cool and dry the detector will be discussed.

A reversed biased photodiode acts as a charged capacitor. Photons of sufficient energy create electron-hole pairs in the semiconductor, effectively discharging the photodiode "capacitor". This results in a reduced voltage across the photodiode which is easily measured [*EG&G Instrument Corp.*, 1990]. Each photodiode has an initial voltage of 5.0 V which drops as it is struck by successive photons; its sensitivity is approximately 4,500 photons per count at 550 nm. Photodiodes have a linear response over an intensity range of seven orders of magnitude. Using the discrete ordinate radiative transfer code discussed in Chapter 4, clear sky zenith intensities ($w/m^2/str$) were calculated and found to vary less than 3 orders of magnitude for solar zenith angles of between 10° and 95°. Since a signal is easily measured at both of these zenith angles, it

can be concluded that the photodiodes are linear over the ranges of intensities measured.

To measure the separate voltages of the entire array, each photodiode was successively connected by shift registers and FET switches in the internal circuitry of the photodiode array to one or the other of the detector head's dual amplifiers. This gave rise to so called "even-odd" noise which was due to slightly different gains of the two operational amplifiers. Each pixel's voltage offset below 5.0 V was proportional to the integrated photon flux that had struck that pixel during the collection time. From the amplifiers each individual pixel's voltage was transmitted sequentially to the detector interface (Model EG&G/PARC OMA 1000) where it was digitized by a 15 bit analog to digital converter and stored in the detector interface memory before being sent to the computer. Control and data information was passed between the host computer (Compaq 386-20e) and the detector interface through a 16 wire parallel AT-GPIB line. A card in one of the computer's expansion slots (Model National Instruments AT-GPIB) allowed IEEE-488 control statements to be passed between the computer and the detector interface.

The experiment was controlled by a program written by Jianli Sun in Fortran (Microsoft version 5.1) which allowed variable exposure times, intervals between exposures,

movement of the filter wheel and grating turret, and wavelength calibration using solar absorption lines. Several subroutines were written in assembler code. Appendix B contains the complete code. Included is the parameter file which allowed exposure time, grating and filter positions, and rough calibration constants to be read into the main program without recompiling. The experiment's timing signal was taken from the computer's internal clock. A more precise wavelength scale of the photodiode array data was set in the program by linear interpolation using the well known Fraunhofer solar absorption lines at 410.1748 and 434.0475 nm.

The grating and the filter wheel were controlled by two RS-232 connections requiring machine code subroutines addition to the main Fortran program. A card was installed (part number Arnett Multi-4 PCB) into one of the computer's AT expansion slots to allow 4 simultaneous RS-232 connections to the computer's one serial port. The data from each exposure was written to the computer's hard disk in an ASCII file taking up about 30 kilobytes; every 2 weeks this raw was transferred to a tape backup with a capacity of 60 Megabytes (Compaq part number CPAQF527U) and set aside for further analysis. These files were turned into text files which compressed them to 3.0 kilobytes or converted into binary files which required 1.0

kilobytes. At last the files were read into the analysis program to recover total slant column amounts of NO_2 as described in Chapter 3.

Cooling and Drying Arrangements

The diode array was cooled by a Peltier device to 0°C to reduce Johnson or thermal noise [*Dereniak and Crowe*, 1984]. Such noise is reduced in half for every 7°C of cooling. Setting the temperature of the photodiode array was accomplished by sending a setpoint from the computer to the OMA controller which then used a simple thermostatic circuit to control the cooling device attached to the photodiode array. Care was taken so that the temperature at detector temperature had stabilized before measurements were attempted, so the Peltier cooling device was left running continuously. At 0°C, the temperature at which all measurements were taken, the dark noise was approximately 1,500 counts per second.

One measurement of dark noise was made each day by using the filter wheel in which was placed a metal disk to block all the light to the detector. This dark noise was subtracted from each of that day's subsequent measurement. To aid the cooling of the detector, a circulating pump sent ambient temperature alcohol through the aluminum block which removed heat from the hot side of the Peltier device. A fan

forced air on the alcohol as it returned to the recirculating pump to aid in heat dissipation. Still lower temperatures could be achieved by chilling the alcohol or by adding more stages to the Peltier device.

It was found that moisture condensed upon the cooled detector in humid conditions. To prevent this condensation a slight pressure of dried nitrogen was flowed into the area around the detector.

Appendix B
Control Software

```
c******** Written by Jianli Sun ************************
c******Modified to shorten the background correction*****
c******and calibration routine to 1 min******************
c******JRS 2/23/92 ***************************************
c*******************************************************
c*******************************************************
c
c   This program is used for solar spectrum collection
c
c*******************************************************
      program mainl
      character*30
datafile,parmfile,stat,tread*10000,tread1*3000
      character*1 conti,change,spec,detec,blkf,code,filt
      integer
temp,mode,scan,igno,memo,iaa(1024),period,ibb(1024)
      integer m,port1,port2,baud,parity,stopbit,wordl,iy(512)
      integer hour,min,sec,hsec,hour2,min2,sec2,hsec2,iz,rep
      integer period2,z,q
      real etime,cof1,cof2,lowav1,lowav2
      integer max,lab1,grat
      character*21
string,string1*18,string2*18,string3*17,string4*17
      character*17 string5
      lab1=2000
      lab2=200
c*********************************************************
********
c
c    Variable declare:
c       port1---- spectrometer port number
c       port2---- filter wheel port number
c       baud----- baud rate of RS232 port
c       parity--- parity bit of RS232 port
c       stopbit-- stop bit of RS232 port
c       wordl---- word length of RS232 port
c       temp----- temperture of detector
c       mode----- acquisition mode of detector
c       scan----- scane number of detector
c       igno----- ignore number of detector
c       etime---- exposure time of detector
c       cof1----- coefficient 1 of spectrum calibration
c       cof2----- coefficient 2 of spectrum calibration
c       blkf----- block function variable
c
```

```
c*****************************************************
      call setvm(3)
      write(*,*) "SOLAR SPECTRUM ACQUISITION SYSTEM"
      write(*,*)
      write(*,*)
      write(*,*) "input time period "
      read(*,100) period
  100   format(I2)
      write(*,*) "input name of data file   xxxx___.dat"
      read(*,110)  datafile
  110    format(A)
      write(*,*) "input name of parameter file"
      read(*,110) parmfile
c  ****************************************************
c
c  Open GPIB0, parameter file, data file
c       Parameter file=parm.dat , data file=datafile
c       tempery file=temp.dat, parameter file=parmfile
c
c ****************************************************

      open (1,file='gpib0', status='old',access='sequential',
      1  form='formatted', mode='readwrite')
      open (5,file=parmfile)
      open (6,file='temp.dat',status='unknown')
      open (8,file='grap.dat')

c*****************************************************
c
c  initialize the DETECTOR through GPIB0
c
c ****************************************************

      write(1,*) 'ABORT'
      write(1,*) 'RESET'
      write(1,*) 'REMOTE 12'
      write(1,*) 'GPIBEOS CR'
c         write(1,*) 'LANGEOS CR LF'
c
*****************************************************
c
c       read parameters of RS232 port
c       parameters: baud,parity,stopbit,wordlength,port
number
c
c
*****************************************************

      read(5,130) baud
```

```
      read(5,130) parity
      read(5,130) stopbit
      read(5,130) wordl
      read(5,130) port1
      read(5,130) port2

c ***********************************
c
c  initialize RS-232 port
c
c ************************************

     call init(baud,parity,stopbit,wordl,port1,mstat,istat)
     call init(baud,parity,stopbit,wordl,port2,mstat,istat)

*************************************************************
*
c
c  read parameters from parameter file
c  parameters: temperature, data acquisition mode, scane
No.,
c              ignore No., memory No.
c
c*************************************************************
**

     read(5,150) cof1
     read(5,160) cof2
     read(5,150) cwave1
     read(5,140) range1
     read(5,140) cwave2
     read(5,140) range2
     read(5,130) temp
     read(5,130) mode
     read(5,130) scan
     read(5,130) igno
     read(5,130) memo
     read(5,140) etime
  130   format(t20,i3)
  140   format(t20,f6.3)
c  140   format(t20,i2)
  150   format(t20,f8.4)
  160   format(t20,f7.5)
c*******************************************************
c
c  if spectrometer'parameters need to be set
c
c*******************************************************
```

```
  200   call task(port1)

c ****************************
c
c  set status of filter
c
c ****************************

      call task(port2)

c*********************************************************
c
c  clear the memory of the device and check error
c
c*********************************************************

      write(1,*) 'OUTPUT 12 ; CRM'
      write(1,*) 'LANGEOS CR LF'
      call spoll (2,m,stat)
c         write(*,*) stat
      if(m.eq.1) call error

c  ****************************
c
c    read repeat number
c
c*******************************

       read (5,130) rep
c********************************
c
c    read the central wavelength
c    and grating number
c
c********************************

       read (5, 165) wlength
       read (5, 180) grat
 165      format(t20,f5.1)
 180      format(t20,i1)
c*******************************
c
c    read block founction
c
c*******************************

       read (5, 170)  blkf

  170     format(t20,a)
```

```
c*********************************************
c
c  if block function is not background function
c  read background data file :bg.dat
c
c*********************************************

       if(blkf.eq.'b' ) goto  298
       open(9, file='bg.dat')
       do 330 i=1,1024
       read(9,*) ibb(i)
  330     continue
       close (9)
c*******************************************************
c
c   set parameters and data acquisition mode
c
c*******************************************************
 298      n=0
 300      write(string1,251) mode
 251     format('OUTPUT 12 ; DA ',i3)
      write(1,*) string1
      write(string2,252) temp
 252     format('OUTPUT 12 ; DT ',i3)
      write(1,*) string2
      write(string3,253) scan
 253     format('OUTPUT 12 ; I ',i3)
      write(1,*) string3
      write(string4,254) memo
 254     format('OUTPUT 12 ; J ',i3)
      write(1,*) string4
      write(string5,255) igno
 255     format('OUTPUT 12 ; K ',i3)
      write(1,*) string5
      write(string,250) etime
 250     format('OUTPUT 12 ; ET ',f6.3)
      write(1,*) string
c 300     write(1,*) 'OUTPUT 12 ; DA 1'
c        write(1,*) 'OUTPUT 12 ; DT 25'
c        write(1,*) 'OUTPUT 12 ; I 5'
c        write(1,*) 'OUTPUT 12 ; J 1'
c        write(1,*) 'OUTPUT 12 ; K 0'
c         write(1,*) 'OUTPUT 12 ; ET 3'
c         write(1,*) 'OUTPUT 12 ; ET'
c         write(1,*) 'ENTER 12#10'
c         read(1,'(A)') reading
c         rewind 1
c  222    call spoll(2,m,stat)
c         if(m.ne.1) goto 222
```

```
c         write(1,*) 'OUTPUT 12 ; CL'
c         write(1,*) 'ENTER 12#10'
c         read(1,'(A)') stat
c         rewind 1
c         call posi(8)
c         write(*,*) stat
c         call inkey(code)
c         if(code.eq.'y') goto 999
c         goto 222

      do 299 kk=1,520
      write(*,*) etime
 299     continue


c  ****************************************
c
c
c      repeat the following program REP time
c
c*******************************************
c ******************************************
c    set counter to 0
c ******************************************
     z=0
     q=0
 400    do 770  ij=1,rep
c  ****************************
c
c
c     if (blkf.eq.b).or.(blkf.eq.c)set period = 5
c     otherwise leave period as it was!
c
c
c  ******************************
     if((z.eq.0).and.(blkf.eq.'b')) period2=period
     if(blkf.eq.'b') period=5
     if(blkf.eq.'c') period=5
     if(blkf.eq.'b') z=z+1
     if((blkf.eq.'n').and.(q.eq.0)) period=5
     if((blkf.eq.'n').and.(q.gt.0))period=period2
     if(blkf.eq.'n') q=q+1
c  ****************************
c
c    keyboard and timer control
c
c  ****************************

      l=0
```

```
 500      call inkey(code)
      if(code.eq.'y') goto 999

      call timer(hour,min,sec,hsec)
c         call setvm(3)
c         call posi(5)
c         write(*,510) "TIME (hh:mm:ss:hs) "
c 510     format('+',t6,a19)
c         call posi(7)
c         write(*,520) hour,min,sec,hsec
c  520    format('+',t6,i2.2,':',t9,
i2.2,':',t12,i2.2,':',t15,i2.2)
      if(n.eq.0) goto 650
      if((hour.eq.0).and.(hour2.eq.23))  goto 530
      if((hour*60+min).eq.(hour2*60+min2+period)) goto 550
      goto 540
 530     if((24*60+min).eq.(hour2*60+min2+period)) goto 550
 540     goto 560
 550     if((sec.ge.sec2)) goto 650
 560     if(l.gt.0) goto 640
      l=l+1
c*******************************
c
c        plot curv on screen
c
c*******************************
      call setvm(6)
      call posi (0)
      write(*, 561) "SOLAR SPECTRUM"
  561    format('+',30x,a14)
      write(*,562)  "TIME :",hour,min,sec,"DATAFILE
:",datafile
  562
format(5x,a6,2x,i2.2,':',i2.2,':',i2.2,33x,a10,2x,a11)
      do 563  ji=0,639
      call point(ji,20)
  563   continue
      do 564  ji=60,600
      call point(ji,23)
      call point(ji,189)
  564    continue
      do 565  ji=23,189
      call point (60,ji)
      call point (600,ji)
  565    continue
      do 566  ji=169,23,-20
      call point(59,ji)
      call point(61,ji)
      call point(62,ji)
```

```
 566    continue
      do 567  ji=110,600,50
      call point(ji,187)
      call point(ji,188)
      call point(ji,191)
 567    continue

      rewind 8
      do 570 i=0,511
      read(8,*) iy(i)
      read(8,*) iz
      if(i.eq.0) max=iy(i)
      if(i.eq.0) min=iy(i)
      if(iy(i).gt.max) max=iy(i)
      if(iy(i).lt.min) min=iy(i)
570     continue
      rewind 8
        lab1=(max-min)/4+min
      call posi(3)
      write(*,568) max
 568    format('+',t2,i6)
      call posi(8)
      write(*,568) min+3*(max-min)/4
      call posi(13)
      write(*,568) min+2*(max-min)/4
      call posi(18)
      write(*,568) lab1
      call posi(24)
      lab20=cof11
      lab21=cof11+cof22*lab2
      lab22=cof11+2*cof22*lab2
      lab23=cof11+3*cof22*lab2
      lab24=cof11+4*cof22*lab2
      lab25=cof11+5*cof22*lab2
     write(*,569) lab20,lab21,lab22,lab23,lab24,lab25
 569   format('+',t8,i3,t20,i3,t33,i3,t45,i3,t58,i3,t70,i3)
      do 620 i=0,511
      iy(i)=189-int((iy(i)-min)*160/(max-min))
c         write(7,*) iy(i)
      if(i.eq.0) goto 610
      if(iy(i).eq.iy(i-1)) goto 610
      if(iy(i).gt.iy(i-1)) goto 590
      do 580 ii=1,abs(iy(i)-iy(i-1))-1
      call point((i+60),(iy(i)+ii))
 580    continue
      goto 610
 590    do 600 ii=1,abs(iy(i)-iy(i-1))-1
      call point((i+60),(iy(i)-ii))
 600    continue
```

```
  610     call point((i+60),iy(i))
  620     continue
  640     goto 500
  650     call setvm(3)
      n=n+1
      hour2=hour
      min2=min
      sec2=sec
      hsec2=hsec
c          write(*,*) hour,":",min,":",sec

c******************************
c
c  begin to capture data
c
c******************************

  700     write(1,*) 'OUTPUT 12 ; RUN'
  710     call spoll(1,m,stat)
c          write(*,*) m
c          write (*,'(A)') stat
      if(m.eq.0) goto 710
      call setvm(3)
      call posi(5)
      write(*,730) "DETECTOR STATUS "
      write(*,740) stat

c***********************************
c
c send data from device to computer
c
c***********************************

      i=0
      write(1,*) 'OUTPUT 12 ; DC 1,1,1024'

 720    write(1,*) 'ENTER 12#3000'
      read(1,'(A)')tread1
      rewind 1
      j=i*3000+1
      k=(i+1)*3000
      tread(j:k)=tread1
      i=i+1
      call spoll(128,m,stat)
      call setvm(3)
      call posi(5)
      write(*,730) "DETECTOR STATUS "
 730     format('+',t6,a16)
      write(*,740) stat
```

```
 740      format(' ',t6,a5)
      if(stat.eq.'/.(') goto 720
      if(stat.eq.'000') goto 720
      if(stat.eq.'0''*') goto 720
      if(stat.eq.'032') goto 720
      write(6,750) tread
  750    format(A)
      rewind 6
      write(datafile(5:7), '(i3.3)') n
      open(7, file=datafile , status='unknown')
      read (6,*)iaa
      rewind 6
      cof22=grat*cof2
      cof11=wlength-grat*(440-cof1)
      if(blkf.eq.'b') goto 8100
      if(blkf.eq.'c') goto 8200
      if(blkf.eq.'n') goto 8300
      call error
c****************************
c
c  Capture background data
c
c****************************

 8100   write(7,*) "  Background data file "
     write(7,*)
     write(7,*) "     x=wavelength       Y=count"
     write(7,*)
     do 8110  jk=1,1024
     wavel=cof11+cof22*jk
     write(7,*) wavel,iaa(jk)
     write(8,*) iaa(jk)
     ibb(jk)=ibb(jk)+iaa(jk)
 8110   continue
     goto 770

c****************************************
c
c    Use Local Minimals for Calibration
c
c****************************************
 8200   write(7,*) "  Spectrum Data File for Calibration"
     write(7,*)
     write(7,*) "     X=wavelength        Y=count"
     write(7,*)
     if( rep.ne.1) goto  8300

     j1=1
     j2=1
```

```
      do 8280 jk=1 ,1024
     wavel=cof11+cof22*jk
     iaa(jk)=iaa(jk)-ibb(jk)
     write(7,*) wavel,iaa(jk)
     write(8,*) iaa(jk)
     if(wavel.lt.(cwave1-range1)) goto  8250
     if(wavel.gt.(cwave1+range1)) goto  8250
     if(j1.ne.1) goto 8230
     lomin1=iaa(jk)
     lowav1=wavel
     lon1=jk
     j1=j1+1
8230   if(iaa(jk).ge.lomin1) goto 8250
     lomin1=iaa(jk)
     lowav1=wavel
     lon1=jk
     j1=j1+1
 8250   if(wavel.lt.(cwave2-range2)) goto  8280
     if(wavel.gt.(cwave2+range2)) goto  8280
     if(j2.ne.1) goto 8260
     lomin2=iaa(jk)
     lowav2=wavel
     lon2=jk
     j2=j2+1
 8260   if(iaa(jk).ge.lomin2) goto 8280
     lomin2=iaa(jk)
     lowav2=wavel
     lon2=jk
     j2=j2+1
 8280    continue
     cof2=(cwave2-cwave1)/(lon2-lon1)
     cof1=cwave1-cof2*lon1
     write(7,*) "coefficient",cof1,cof2
     goto 770

c*************************************
c
c       Save the Spectrum Data
c
c*************************************

 8300   write(7,*) "   Spectrum Data File"
     write(7,*)
     write(7,*) "      X=wavelength       Y=count"
     write(7,*)
     do 8380 jk=1,1024
     wavel=cof11+cof22*jk
     iaa(jk)=iaa(jk)-ibb(jk)
     write(7,*) wavel,iaa(jk)
```

```
      write(8,*) iaa(jk)
 8380   continue
 770    continue

c*************************************
c
c  average the noise of background
c
c*************************************

      if(blkf.ne.'b') goto 779
      open(9, file='bg.dat')
      do 8150 i=1,1024
      ibb(i)=ibb(i)/rep
      write(9,*) ibb(i)
 8150    continue
      close (9)

c****************************
c
c  finish the work or not ?
c
c****************************

 779      read(5,780) conti
      if(conti.eq.'n')  goto 999
 780    format(t20,a)

c*********************************
c
c    read REP from parameter file
c
c*********************************

      read (5,130) rep


c*********************************
c
c     read block founction  blkf
c
c*********************************

       read(5, 170) blkf
c*********************************
c
c  change parameters or not ?
c
c*********************************
```

```
      read(5,780) change
      if( change.eq.'n')  goto 400

c***********************************
c
c  change spectrometer parameters ?
c
c***********************************

      read(5,780) spec
      if(spec.eq.'n') goto 800

c***********************************
c
c    read central wavelength and
c    grating number
c
c***********************************

       read(5,165) wlength
       read(5,180) grat

c*****************************************
c
c   call subrountine to set spectrometer
c   parameters
c*****************************************

      call task(port1)

c ***********************************
c
c   change filter parameters?
c
c ************************************

  800   read(5,780) filt
      if(filt.eq.'n') goto  810
      call task(port2)
c*************************************
c
c  change detector parameters ?
c
c*************************************

  810   read(5,780) detec
     if(detec.eq.'n')  goto 400
     read(5,130) temp
     read(5,130) mode
```

```
      read(5,130) scan
      read(5,130) igno
      read(5,130) memo
      read(5,140) etime
      goto 300
      close (1)
  999   call setvm(3)
c        rewind (5)
c        do 1000 i=1,6
c        read(5,130) iaa(i)
c 1000   continue
c        write(5,150) cof1
c        write(5,160) cof2
c        write(5,150) lowav1
c        write(5,150) lowav2

      close (5)
      stop
      end

c*****************************
c
c   subroutine of error
c
c*****************************

      subroutine error
      write(*,1000)
 1000   format('device or parameters error')
      stop
      end

c*********************************
c
c  Subrouting of serial Polling
c
c*********************************

      subroutine spoll(ibit,m,state)
      integer ibit,m
      character*30 state
      write(1,*) 'SPOLL 12'
      read(1,'(A)') state
      rewind 1
      m=(ichar(state(1:1))-48)*100+(ichar(state(2:2))-48)*10
      m=m+ichar(state(3:3))-48
      m=mod((m/ibit),2)
      return
      end
```

```
c
*************************************************************
******
c     this is subroutine using RS232 for communication
c
*************************************************************
******
      subroutine task(port)
      parameter (lbufsiz=256)
      character*80 chai,chab
      character*1 ic,lbuf(lbufsiz),lbufb(lbufsiz)
      integer next,port,istat
      equivalence (chai,lbuf), (chab,lbufb)

c     ************************
c     procedure control section
c     ************************
      next=0
 100  next=next+1
      if(next.gt.2) next=1
      go to (200,300) next

c
*************************************************************
*****
c     read control code from parameter file and send to
RS232 interface
c
*************************************************************
*****


 200  read (5,210)chai
 210  format(t20,a)
      if (chai.eq.'over') go to 900
      l=len(chai)

 220   call stat(port,mstat,istat)

      if (iand ( istat,96).eq.0) go to 220
      do 230 i=1,l
      lb=ichar(lbuf(i))
      call trans(lb,port,istat)

 230  continue
      go to 100

c     **************************
c      check target's response
```

```
c       **************************

  300   i=0
  310   call stat(port,mstat,istat)
        call setvm(3)
        call posi(5)
        write(*,330) "RS-232 PORT STATUS"
  330   format('+'t6,a18)
        ih=istat
        write(*,340) ih
  340   format('0',t6,i4)
        if(iand(istat,1).ne.1) go to 310
  350   call fetch(ic,port,istat)
        call setvm(3)
        call posi(5)
        write(*,330) "RS-232 PORT STATUS"

        call posi(7)
        ih=istat
        write(*,340) ih
        i=i+1
        lbufb(i)=ic
        if(iand(istat,1).eq.1) go to 350
        call setvm(3)
        call  posi (8)
        write(*,330) "TARGET  STATUS"
        write (*,360) chab
  360   format(' ',t6,a10)
        go to 100

  900   return
        end
c
c  subroutine of timer
c
        subroutine timer(hours,mins,secs,hsecs)
        integer a,b,hours,mins,secs,hsecs
        call time(a,b)
        hours=a/256
        mins=mod(a,256)
        secs=b/256
        hsecs=mod(b,256)
        return
        end
```

Parameter File

```
baud                :7
parity              :0
stopbit             :1
wordlength          :3
spectrometer port   :2
filters port        :3
coefficient1        :402.9198
coefficient2        :0.06887
central wave1       :410.1748
range1              :0.5
central wave2       :434.0475
range2              :0.5
tempture            :0
acquition mode      :1
scan counter        :900
ignore counter      :1
memory counter      :1
exposure time       :0.150
echo status         :no-echo
scan rate           :200.0 nm/min
grating             :1 grating
wave length         :440.0 goto
finish  setting     :over
echo status         :no-echo
filter              :1 filter
finish setting      :over
repeat number       :1
c wavelength        :440.0
c grating           :1
block function      :b
continue            :y
repeat number       :1
block function      :c
change parameters   :y
change spec parm    :n
change filter       :y
filter              :2 filter
finish setting      :over
change detector     :n
continue            :y
repeat number       :48
block function      :n
change parameter    :n
continue            :y
repeat number       :1
block function      :n
change parameter    :n
```

```
continue           :y
repeat number      :1
block function     :c
change parameter   :n
continue           :y
repeat number      :150
block function     :n
change parameter   :n
continue           :n
```

References

Adams, C. N., and G. W. Kattawar, *Radiative transfer in spherical shell atmospheres I. Rayleigh scattering, Icarus, 35,* 139, 1978.

Andrews, D. G., J. R. Holton, and C. B. Leovy, *Middle Atmosphere Dynamics*, 489 pp., Academic Press, Orlando, Fla., 1987.

Austin, J., R. R. Garcia, J. M. Russel III, S. Solomon, and A. Tuck, On the Atmospheric Photochemistry of Nitric Acid, *J. Geophys. Res., 91,* 5477-5485, 1986.

Bowling, S. A., T. Ohtake, and C. Benson, Winter Pressure Systems and Ice Fog in Fairbanks, Alaska, *J. Appl. Meteor.* 7, 961-968, 1968.

Brasseur, G., and S. Solomon, *Aeronomy of the Middle Atmosphere,* 2nd ed., 441 pp., D. Reidel, Norwood, Mass., 1986.

Brasseur, G., and C. Granier, Pinatubo aerosols, chlorofluorocarbons, and ozone depletion, *Science, 257,* 1239-1242, 1990.

Brewer, A. W., C. T. McElroy, and J. B. Kerr, Nitrogen Dioxide Concentration in the Atmosphere, *Nature 264,* 129-133, 1973.

Camy-Peyret, J.-M. Flaud, A. Perrin, C. P. Rinsland, A. Goldman, and F. J. Murcray, Stratospheric N_2O_5, CH_4, and N_2O Profiles from IR Solar Occultaion Spectra, *J. Atm. Chem., 16,* 31-40, 1993

Chahine, M. T.. Generalization of the Relaxation Method for the Inverse Solution of Nonlinear Transfer Equations, in *Inversion Methods in Atmospheric Remote Sounding,* A. Deepak (ed.), 622 pp., Academic Press, New York, 1977.

Chapman, S., A theory of upper atmmospheric ozone, *Q. J. R. Meteorl. Soc. 3,* 103-125, 1930.

Collins, D. G., W. G. Blattner, M. B. Wells, and H. G. Horak, Backwards monte carlo calculations of the polarization characteristics of the radiation emerging

from a spherical shell atmosphere, *Appl. Opt., 11,* 2684, 1972.

Crutzen, P. J., The Influence of Nitrogen Oxides in the Atmospheric Ozone Content, *Quart. J. Roy. Met. Soc., 96,* 320-325, 1970.

Dahlback, A., and K. Stamnes, A new spherical model for computing the radiation field available for photolysis and heating at twilight, *Planet. Space. Sci., 39,* 671-683, 1991.

Davidson, J. A., C. A. Cantrell, A. H. McDaniel, R. E. Shetter, S. Madronich, and J. G. Calvert, Visible-ultraviolet absorption cross sections for NO_2 as a function of temperature, *J. Geophys. Res., 93,* 7105-7112, 1988.

DeMore, W. B., M. J. Molina, S. P. Sander, D. M. Golden, R. F. Hampson, M. J. Kurylo, C. J. Howard, and A. R. Ravishankara, Chemical Kinetics and Photochemical Data for Use in Stratospheric Modeling, *JPL Publ., 90-91,* 1990.

Delbouille, L., *Atlas Photometrique Spectre Solaire,* Institute d'Astrophysique de l'Universitedi Liege, Belgium, 1973.

Dereniak, E. L., and D. G. Crowe, *Optical Radiation Detectors*, 300 pp., John Wiley and Sons, New York, 1984.

Deshler, T., D. J. Hofmann, J. V. Hereford, and C. B. Sutter, Ozone and temperature profiles over McMurdo Station, Antarctica, in the spring of 1989, *Geopys. Res. Lett., 17,* 151-154, 1990.

Dutton, J. A., *The Ceaseless Wind,* 617 pp., Dover Publications, New York, 1986.

E. G. & G Instruments Corporation, Silicon Photodiode Detector Instruction Manual, 31 pp., Princeton, N.J., 1990.

Farman, J. C., G. Gardiner, and J. D. Shanklin, Large Losses of Total Ozone in Antarctica Reveal Seasonal ClO_x/ NO_x Interaction, *Nature, 315*, 207-210, 1985.

Finlayson-Pitts, B. J., and J. N. Pitts, *Atmospheric*

Chemistry: Fundamentals and Experimental Design, 1098 pp., John Wiley and Sons, New York, 1986.

Fujiwara, M., T. Shibata, M. Maeda, and M. Hirona, Lidar Observations of the Middle Atmosphere, *Rev. of Laser Engrn., 17,* 4, 240-257, 1989.

Ginzberg, V. L., Line Width in the Spectrum of Scattered Light, *Soviet Physics Uspekhi, 15,*(1), 114-120, 1972.

Gil, M., and J. Cacho, NO_2 Total Column Evolution During the 1989 Spring at Antarctic Peninsula, *J. Atm. Chem., 15,* 187-200, 1992.

Goldman, A., F. J. Murcray, R. D. Blatherwick, J. J. Kosters, and D. G. Murcray, Stratospheric HNO_3 Measurements from 0.0002-cm^{-2} Resolution Solar Occultation Spectra and Improved Spectroscopic Line Parameters in the 5.8-μm Region, *J. Geophys. Res., 97,* 2561-2567, 1992.

Götz, F. W. P., A. R. Meethan, and G. M. B. Dobson, The Vertical Distribution of Ozone in the Atmosphere, *Proceedings Royal Soc.,* 416-446, 1934.

Grangier, J. F., and S. Ring, Anomalous Fraunhofer line profiles, *Nature, 193,* 762, 1962.

Hamill, P., and R. P. Turco, and O. B. Toon, On the Growth of Nitric and Sulfuric Acid Aerosol Particles Under Stratospheric Conditions, *J. Atm. Chem., 7,* 287-315, 1988.

Hamill, P. and O. B. Toon, Polar Stratospheric Clouds and the Ozone Hole, *Physics Today, 24,* 34-42, December, 1991.

Hanson, D. R., and A. R. Ravishankara, The Reaction Probabilities of $ClONO_2$ and N_2O_5 on 40% to 75% Sulfuric Acid Solutions, *J. Geophys. Res., 96,* 17307-17314, 1991.

Harrison, A. W., Midsummer Stratospheric NO_2 at Latitude 45° S, *Can. J. Phys., 57,* 1110-1117, 1979.

Hofmann, D. J. and S. Solomon, Ozone destruction through heterogeneous chemistry following the eruption of El Chichon, *J. Geophys. Res., 94,* 5029-5041, 1989.

Hutley, M. C., *Diffraction Gratings*, 310 pp., Academic Press, London, 1982.

Jäger, H. and D. Hofmann, Midlatitude lidar backscatter to mass, area, and extinction conversion model based on *in situ* aerosol measurements from 1980 to 1987, *Appl. Opt., 30,* 127-138, 1991.

Johnston, P. V. and R. L. McKenzie, NO_2 Observation at 45° S During the Decreasing Phase of Solar cycle 21, from 1980 to 1987, *J. Geophys. Res., 94,* 3473-3486, 1989.

Johnston, P. V., DSIR Data Analysis Procedure, internal distribution to the Network for Detection of Stratospheric Change Instrument Intercomparison, held in Boulder, 1991.

Johnston, P. V., R. L. McKenzie, G. Keys, and A. Matthews. Observations of Depleted Stratospheric NO_2 Following the Pinatubo Volcanic Eruption, *Geophys. Res. Lett., 19* 211-213, 1992.

Kattawar, G. W., and C. N. Adams, *Radiative transfer in spherical shell atmospheres II. asymmetric phase functions, Icarus, 35,* 436, 1978.

Kattawar, G. W., A. T. Young, and T. J. Humphreys, Inelastic Scattering in Planetary Atmospheres. 1. The Ring Effect Without Aerosols, *Astrophys. Journ., 243,* 1049-1057, 1981.

Kawa, S. R., D. H. Fahey, L. E. Heidt, W. H. Pollack, S. Solomon, D. E. Anderson, M. Lowenstein, M. H. Profitt, J. J. Martigan, and K. R. Chan, Photochemical Partitioning of the Reactive Nitrogen and Chlorine Reservoirs in the High Latitude Stratosphere, *J. Geophys. Res., 97,* 7905-7923, 1992.

Krehler, K., M. Feidler, T. Gomer, J. Stutz, and U. Platt, The Latitudinal Distribution (50°N-50°S) of NO_2 and O_3 in October/November 1990, *Geophys. Res. Lett.,* in press 1994.

Kylling, A., and K. Stamnes, Efficient yet Accurate Solution of the Linear Transport Equation in the Presence of Internal Sources: The Exponential-Linear-in-Depth Approximation, *Journ. Comp. Phys., 102*(2), 265-276, 1992.

Lenoble, J., and H. B. Chen, Monte Carlo study of the effects of stratospheric aerosols and clouds on zenith sky absorption measurements, Paper presented at the International Radiation Symposium, IAMAP, Tallin, Estonia, Aug. 1992.

Lubin, D., J.E. Frederick, C. R. Booth, T. Lucas, and D. Neushuler, Measurements of enhanced springtime ultraviolet radiation at Palmer Station, Antarctica, *Geophys. Res. Lett., 16,* 783-785, 1989.

McCormick, M. P., T. J. Swissler, W. P. Chu, amd W. H. Fuller, Post-Volcanic Aerosol Decay as Measured by Lidar, *J. Atmos. Sci., 35,* 1296-1303, 1978.

McCormick, M. P. and R. E. Veiga, SAGE II measurements of early Pinatubo aerosols, *Geophys. Res. Lett., 19,* 155-158, 1992.

McKenzie, R. L. and P. V. Johnston, Seasonal Variations in Stratospheric NO_2 at 45°S, *Geophys. Res. Lett., 9,* 1255-1258, 1982.

McKenzie, R. L. and P. V. Johnston, Stratospheric Ozone Observations Simultaneous with NO_2 at 45 °S, *Geophys. Res. Lett., 10,* 337-340, 1983.

McKenzie, R. L. and P. V. Johnston, Springtime Stratospheric NO_2 in Antarctica, *Geophys. Res. Lett., 11,* 73-75, 1984.

McKenzie, R. L., P. V. Johnston, C. T. McElroy, J. B. Kerr, and S. Solomon, Altitude distributions of stratospheric constituents from ground-based measurements at twilight, *J. Geophys. Res., 96,* 15,499-15,111, 1991.

Mills, M. J., A. O. Langford, T. J. O'Leary, K. Arpag, H. L. Miller, M. H. Profitt, R. W. Sanders, and S. Solomon, On the Relationship Between Stratospheric Aerosols and Nitrogen Dioxide, *Geophys. Res. Lett., 20,* 1187-1190, 1993.

Molina, L. T. and M. J. Molina, Absolute absorption cross sections of ozone in the 185-350 nm wavelength range, *J. Geophys. Res., 91,* 14,501-14,508, 1986.

Moore, C. E., M. G. Minaert, and J. Houtgast, *The Solar Spectrum from 2935 A to 8770 A,* 349 pp., National Bureau of Standards, 1966.

Mount, G. W., R. W. Sanders, A. L. Schmelteklopf, and S. Solomon, Visible Spectroscopy at McMurdo Station, Antarctica 1. Overview and Daily Variations of NO_2 and O_3: Austral Spring, 1986, *J. Geophys. Res., 92,* 8320-8328, 1987.

Mozurkewich, M., and J. G. Calvert, Reaction Probability of N_2O_5 on Aqueous Solutions, *J. Geophys. Res., 93,* 15,889-15,896, 1988.

Murcray, F. J., J. J. Kosters, R. D. Blatherwick, J. Olson, and D. G. Murcray, High resolution solar spectrometer system for measuring atmospheric constituents, *Applied Optics, 29,*(10), 1520-1525, 1990.

Nash, J. C., *Compact Numerical Methods for Computers: Linear Algebra and Functional Minimization*, 167 pp., Adam Hilger, Bristol, England, 1979.

Naudet, J. P., D. Huguenin, P. Rigaud, and D. Cariolle, Stratospheric Observations of NO_3 and its Experimental and Theoretical Distribution Between 20 and 40 km, *Planet. Space Sci., 29,*(6), 707-712, 1981.

Nicolet, M., Stratospheric Ozone: An Introduction to its Study, *Rev. Geophys. Space Sci., 13,* 5593-5636, 1975.

Nicolet, M., Solar Spectral Irradiances with their Diversity Between 120 and 900 nm, *Planet. Space Sci., 137,* 1249-1289, 1989.

Noxon, J. F., Nitrogen Dioxide in the Stratosphere and Troposphere Measured by Ground Based Absorption Spectroscopy, *Science, 189,* 547-549, 1975.

Noxon, J. F., E. C. Whipple, Jr. and R. S. Hyde, Stratospheric NO_2 1. Observational Method and Behavior at Mid-Latitude, *J. Geophys. Res., 84,* 5047-5065, 1979.

Noxon, J.F., W. R. Henderson, and R. B. Norton, Stratospheric NO_2 3; The Effects of Large Scale Horizontal Transport, *J. Geophys. Res., 88,* 5240-5248, 1983.

Perliski, L. M., The Role of Multiple Scattering in Twilight Zenith Sky Observations of Atmospheric Absorbers: Diurnal Photochemistry and Airmass Factors, Ph. D. thesis, Boulder, University of Colorado, 1992.

Perliski, L. M., and S. Solomon, On the Evaluation of Air Mass Factors for Atmospheric Near-Ultraviolet and Visible Absorption Spectroscopy, *J. Geophys. Res., 98,* 10,363-10,374, 1993.

Pinto, J. P., R. P. Turco, and O. B. Toon, Self-Limiting Physical and Chemical Effects in Volcanic Eruption Clouds, *J. Geophys. Res., 94,* 11,165-11,174, 1989.

Pitari, G., and G. Visconti, Odd Nitrogen Removal on Background Sulfate Aerosols: Implications for the Ozone Hole, *Geophys. Res. Lett., 18,* 1853-1856, 1991.

Pommereau, J. P., and F. Goutail, Stratospheric O_3 and NO_2 observations in the summer polar circle in summer and fall 1988, *Geophys. Res. Lett., 15,* 895-897, 1988.

Reihs, C. M., D. M Golden, and M. A. Tolbert, Nitric Acid Uptake by Sulfuric Acid Solutions Under Stratospheric Conditions: Determination of Henry's Law Solubility, *J. Geophys. Res., 95,* 16,545-16,550, 1990.

Roscoe, H. R., Review and Revison of Measurement of Stratospheric N_2O_5, *J. Geophys. Res., 96,* 10,879-10,884, 1991.

Roscoe, H. R. and H. K. Hind, The Equilibrium constant of NO_2 with N_2O_4 and the temperature Dependence of the Visible Spectrum of NO_2: A Critical Review and the Implications for Measurements of NO_2 in the Polar Stratosphere, *Journ. Atm. Chem., 16,* 257-276, 1993.

Schiller, C. A. Wahner, U. Platt, H.-P. Dorn, J. Callis, D. Ehhalt, Near UV Atmospheric Absorption Measurements of Column Abundances During Airborne Arctic Stratospheric Expedition, January-February, 1989: 2. OClO Observations. *Geophys. Res. Lett., 17,* 4, 510-504, 1990.

Shaw, G., Radiance and Color of the Sky at Twilight: Perturbations Caused by Stratospheric Haze, *Pageoph, 119,* 231-247, 1981.

Shibata, T. T. Itabe, K . Mizutani, and K. Asai, Pinatubo volcanic aerosols observed by lidar at Wakkani, Japan, *Geophys. Res. Lett., 21,* 197-200, 1994.

Shimazaki, T., *Minor Constituents in the Middle Atmosphere,* 443 pp., D. Reidel Publishing Company, Tokyo, Japan,

1985.

Solomon, S., and R. W. Sanders, On the Interpretation of Zenith Sky Measurements, *J. Geophys. Res., 92,* 8311-8319, 1987.

Solomon, S., G. H. Mount, R. W. Sanders, R. D. Jakoubek, and A. L. Schmeltekopf, Observations of the Nighttime Abundance of OClO in the Winter Stratosphere Above Thule, Greenland, *Science, 242,* 550-555, 1988.

Solomon, S., Progress towards a quantitative understanding of Antarctic ozone depletion, *Nature, 347,* 347-354, 1990.

Solomon, S., Chemical Families, in *Research Problems in Atmospheric Chemistry,* Cantrell, C. A. , ed., 402 pp. National Center for Atmospheric Research, Boulder, Colorado, 1991.

Solomon, S., and J. G. Keys, Seasonal Variations in Antarctic NO_x Chemistry, *J. Geophys. Res., 97,* 7971-7978, 1992.

Solomon, S., R. W. Sanders, R. O. Jakoubek, K. H. Arpag, S. L. Stephens, J. G. Keys, and R.R. Garcia, Visible and Near-Ultraviolet Spectroscopy at McMurdo Station, Antarctica, 10. Reductions of stratospheric NO_2 due to Pinatubo aerosols, *J. Geophys. Res., 99,* 1992.

Stamnes, K., S.-C. Tsay, W. Wiscombe, and K. Jayaweera, Numerically stable algorithm for discrete-ordinate-method radiative transfer in multiple scattering and emitting layered media, *Appl. Opt., 27,* 2502-2509, 1988.

Stamnes, K., J. Slusser, M. Bowen, C. Booth, and T. Lucas, Biologically Effective Ultraviolet Radiation, Total Ozone Column Abundance, and Cloud Optical Depth at McMurdo Station, Antarctica, September 15, 1988 through April 15, 1989, *Geophys. Res. Lett., 17,*181-2184, 1990.

Stimpfle, R. M., P. O. Wennberg, L. B. Lapson, and J. G. Anderson, Simultaneous, In Situ Measurements of OH and HO_2 in the Stratosphere, *Geophys. Res. Lett., 17,* 1905-1908, 1990.

Stolarski, R. S., A.J. Krueger, M. R. Schoeberl, R. D. McPeters, P. A. Newman, and J. C. Alpert, Nimbus 7

satellite measurement of the springtime Antarctic ozone decrease, *Nature, 322,* 808-811, 1985.

Tolbert, M. A., and M. J. Rossi, Antarctic ozone depletion chemistry: reactions of N_2O_5 with H_2O and HCl on ice surfaces, *Science, 238,* 1258-1260, 1988.

Tolbert, M. A., M. J. Rossi, and D. M. Golden, Heterogeneous interactions of $ClONO_2$, HCl, and HNO_3 with sulfuric acid at stratospheric temperatures, *Geophys. Res. Lett., 15,* 851-854, 1988.

Toumi, R., S. Bekki, and R. Cox, A Model Study of ATMOS Observations and the Heterogeneous Loss of N_2O_5 by the Sulfate Aerosol Layer, *Journ. Atm. Chem., 16,* 135-144, 1993.

Twomey, S., *Introduction to the Mathematics of Inversion in Remote Sensing and Indirect Measurements,* 243 pp., Elsevier, New York, 1977.

Volz, F. E., and R. M. Goody, The Intensity of the Twilight and Upper Atmospheric Dust, *Journ. Atm. Sci., 19,* 385-406, 1962.

Warneck, P., *Chemistry of the Natural Atmosphere,* 753 pp., Academic Press, San Diego, 1988.

Wayne, R. P., *Chemistry of Atmospheres,* 447 pp., Clarendon Press, Oxford, 1991.

Webster, C. R., R. D. May, R. Toumi, and J. A. Pyle, Active Nitrogen Partition in the Nighttime Formation of N_2O_5 in the Stratosphere: Simultaneous in Situ Measurements of NO, NO_2, HNO_3, O_3, and N_2O Using the BLISS Diode Spectrometer, *J. Geophys. Res., 95,* 13,851-13,866, 1990.

Webster, C. R.., R. D. May, D. W. Toohey, L. M. Avallone, J. G. Anderson, P. Newman, L. Lait, M. R. Scheberl, J. W. Elkin, K. R. Chan, Chlorine Chemistry on Polar Stratospheric Cloud Particles in the Arctic Winter, *Science, 261,* 1130-1134, 1993.

Wilson, J. C., H. H. Johnson, C. A. Brock, D. W. Toohey, L. M. Avallone, D. Baumgardner, J. E. Dye, L. R. Poole, D. C. Woods, R. J DeCoursey, M. Osborne, M. C. Pitts, K. K. Kelley, K. R. Chan, G. V. Ferry, M. Lowenstein, J. R. Podolske, and A. Weaver, In Situ Observations of

Aerosol and Chlorine Monoxide After the 1991 Eruption of Mount Pinatubo: Effect of reactions on Sulfate Aerosols, *Science, 261,* 1140-1143, 1993.

Wofsy, S. C., M. J. Molina, R. J. Salawitch, L. E. Fox, and M. B. McElroy, Interactions Between HCl, NO_x, and H_2O Ice in the Antarctic Stratosphere: Implications for Ozone, *J. Geophys. Res. 93.,* 2442-2450, 1988.

World Meteorological Organization, *Atmospheric Ozone, 1985,* v. II, Geneva, 1986.

Zhang, R., P. J. Woolridge, and M. J. Molina, Vapor Pressure Measurements for the $H_2SO_4/HNO_3/H_2O$ and $H_2SO_4/HCl/H_2O$ Systems: Incorporation of Stratospheric Acids into Background Sulfate Aerosols, *J. Phys. Chem., 97,* 8541-8548, 1993.